# A SYSTEMATIC STUDY OF THE DECAYS
## OF
## CHARMED D MESONS

Thesis by

Jay Hauser

In Partial Fulfillment of the Requirements

for the Degree of

Doctor of Philosophy

California Institute of Technology

Pasadena, California

1985

(Submitted May 20, 1985)

## Abstract

A large sample of D mesons, produced by the decay of the $\psi(3770)$ and observed by the Mark III detector at SPEAR, forms the basis for a study of the decays of charmed $D^+$ and $D^0$ mesons. Many Cabibbo-allowed and Cabibbo-suppressed decays are observed. When normalized by a new, absolute technique, the branching ratios appear significantly higher than those reported by previous experiments. No evidence is found for specific final states from $D^0$ decay which are indicative of non-spectator W-exchange diagrams: limits are quoted. Finally, the inclusive semileptonic branching fractions of charged and neutral D mesons are measured by observation of electrons in the recoil from fully reconstructed hadronic D decays of known charm. By neglecting the contribution of Cabibbo-suppressed decays to the total decay widths, the ratio of these branching fractions can be interpreted as the ratio of $D^+$ and $D^0$ lifetimes, thus confirming the inequality of lifetimes observed by direct decay length experiments. The observed pattern of hadronic decays appears to favor modification of the spectator model over non-spectator processes as the main source of the lifetime difference.

## Acknowledgements

The measurements presented in this thesis could not have been made without the work of many members of the Mark III collaboration. In particular, I would like to mention the efforts of Guy Blaylock, in deriving the (preliminary) $D^0 \to K^- \pi^+$ and $D^+ \to K^- \pi^+ \pi^+$ branching ratios; Dan Coffman, who implemented the $e/\pi$ separation algorithm; Alan Duncan, for fitting the $K \pi \pi$ Dalitz plots; and Rafe Schindler, for his contributions to the results on Cabibbo-suppressed decay modes.

I am especially grateful to my advisor, David Hitlin, for his support and encouragement, and to Rafe Schindler, for valuable advice throughout the analysis of the data.

iv

# Table of Contents

## List of Tables

## List of Figures

## 1. Introduction

The existence, quantum numbers, and weak coupling of the charmed quark were predicted in a 1970 paper by Glashow, Iliopoulos, and Maiani[1] which attempted to explain the striking suppression of flavor-changing neutral weak currents observed, for example, in the decay $K_L^0 \to \mu^+\mu^-$. The 'GIM mechanism' requires the charmed quark to couple to an eigenstate of weak isospin $s' = s \cdot \cos\theta_c - d \cdot \sin\theta_c$ which is orthogonal to that eigenstate which couples to the up quark, $d' = s \cdot \sin\theta_c + d \cdot \cos\theta_c$. Flavor-changing neutral currents are thereby eliminated from first-order weak transitions, but are sufficiently suppressed in second-order transitions only if the mass of the charmed quark is a few $\text{GeV}/c^2$. Thus, when the $\psi$ was first seen in 1974 as a narrow enhancement in both p-Be and $e^+e^-$ collisions[2], the mass of $3.097\,\text{GeV}/c^2$ was appropriate for its interpretation as a $c\bar{c}$ (charm-anticharm quark) bound state.

To explain the narrow width of the new state it was postulated that the $\psi$ lies below the threshold for decay to openly charmed particles, such that its decay must proceed via $c\bar{c}$ annihilation. Assuming that quantum chromodynamics (QCD) is the correct theory of strong interactions, the strong decays of the $\psi$ must involve the emission of at least three gluons: a one-gluon intermediate state is forbidden because the $\psi$ is a color singlet, and a two-gluon intermediate state has the wrong charge conjugation. The decays are then suppressed by at least three powers of $\alpha_s$, which has a smaller value according to 'asymptotic freedom'[3] at the large $q^2$ of $\psi$ decay. This is the present explanation of the 'OZI rule' first proposed[4] *ad hoc* in the middle 1960's to suppress the decay $\phi \to \pi^+\pi^-\pi^0$.

Extension of flavor symmetry from SU(3) to SU(4) in order to accommodate the fourth quark opens up the possibility of many new particle states. The existence of these new states was predicted in the original GIM paper[1]. Detailed predictions of their properties were then made available (as a preprint) in 1974, just before the discovery of the $\psi$, in a paper by Gaillard, Lee, and Rosner[5]. The SU(4) extension of flavor symmetry replaces the SU(3) octet of ground-

state pseudoscalar mesons by a multiplet of fifteen mesons, including the $\psi(c\bar{c})$ and six which are explicitly charmed: $D^+(c\bar{d})$, $D^0(c\bar{u})$, $F^+(c\bar{s})$, and their charge conjugates. The ground-state $1/2^+$ baryon multiplet is similarly extended from 8 to 20 particles.

According to the GIM mechanism, the value[6] $\sin\theta_c = 0.23$ naively favors the weak decays of D mesons to strange final states which proceed via the Cabibbo-allowed diagram of Figure 1.1(a), by about a factor of 20 over decays to non-strange final states which proceed via the Cabibbo-suppressed diagrams of Figure 1.1(b) and (c). Doubly-suppressed decays, proceeding by the diagram of Figure 1.1(d), should occur at a negligible rate. When the lowest-lying states with open charm, the $D^0$ and $D^+$ mesons, were discovered[7] in 1976, it was thus encouraging that they appeared as narrow peaks in the strange final states $K^-\pi^+$ at $1.864\,\mathrm{GeV}/c^2$ and $K^-\pi^+\pi^+$ at $1.869\,\mathrm{GeV}/c^2$, respectively. However, the extension from two generations of quarks and leptons to three requires replacement of the GIM mechanism by the six-quark Kobayashi-Maskawa (KM) mixing model[8], in which the single Cabibbo angle is replaced by three angles and a complex phase. The eigenstate of weak isospin which couples to the charmed quark then becomes:

$$s' \equiv b \cdot V_{cb} + s \cdot V_{cs} + d \cdot V_{cd} = b \cdot (c_1 c_2 s_3 + s_2 c_3 e^{i\delta}) + s \cdot (c_1 c_2 c_3 - s_2 c_3 e^{i\delta}) + d \cdot (-s_1 c_2)$$

where $s_1$, $s_2$, and $s_3$ are the sines and $c_1$, $c_2$, and $c_3$ are the cosines of the mixing angles, and $\delta$ is the complex CP-violating phase. Of these terms, only the coefficients of $s$ and $d$ are relevant for charm decays. Moreover, recent measurements which indicate that the lifetimes of beautiful particles are on the order of $10^{-12}$ seconds[9] suggest that $\theta_1 \approx \theta_c$, and that the angles $\theta_2$ and $\theta_3$ are quite small[6], so that the GIM coupling of the charmed quark to

$$s' = s \cdot V_{cs} - d \cdot V_{cd} \approx s \cdot 0.97 - d \cdot 0.23$$

is essentially unaffected by the third generation of quarks and leptons. Experimental support for this picture of charm decays is provided by the observation of charm production in neutrino interactions, from which the measurements[10]:

$$|V_{cd}| = 0.24 \pm 0.03 \quad , \quad |V_{cs}| > 0.59 \text{ at } 90\% \text{ confidence level,}$$

are derived. The measurement of $|V_{cs}|$, however, relies on particularly uncertain assumptions regarding the $s\bar{s}$ sea content of the nucleon wavefunction.

The theoretical literature covering the weak decays of charmed particles is immense. Fairly comprehensive reviews, however, are available, from a theoretical perspective in Reference 11 and Reference 12, and from a more experimental point of view in Reference 13. The following section concerns itself with a brief review of the major topics.

Weak decays of hadronic particles can be classified as purely leptonic, semileptonic, or purely hadronic. The inclusive decay rate for purely leptonic transitions, which scales linearly with mass, is expected to be small relative to semileptonic and hadronic decay rates, which scale roughly as the fifth power of the charm mass[5]. Matrix elements for semileptonic decays involve the product of hadronic and leptonic currents, and can be parametrized by hadronic form factors. The purely hadronic transitions are the most difficult, although perhaps the most intriguing decays to understand. Among the hadronic weak decays of strange particles, a large enhancement of $\Delta I = 1/2$ transitions over $\Delta I = 3/2$ transitions has long been recognized, although not well understood[14]. Explanations for this enhancement in terms of penguin diagrams[15] and operator coefficients[16] have met with qualitative success, although specific calculations suffer greatly from the present inability to calculate strong processes at low $q^2$ ($\approx 0.5\,\text{GeV}^2$). Based on the idea of asymptotic freedom, it was initially hoped that the higher mass of the charmed quark would allow for more reliable calculation of hadronic charm decay rates.
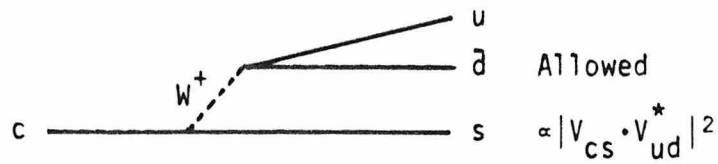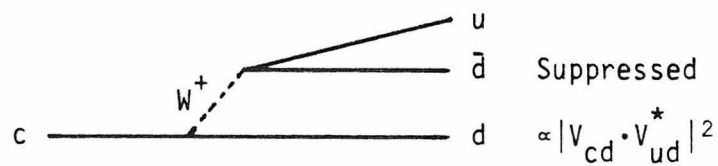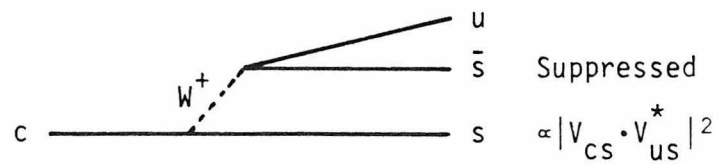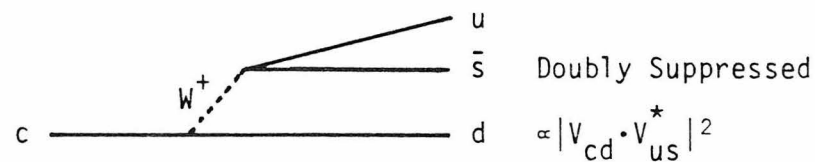
Figure 1.1. Charmed quark decay diagrams: (a) Cabibbo-allowed, (b) Cabibbo-suppressed by the matrix element $V_{cd}$, (c) suppressed by the 'ordinary' Cabibbo matrix element $V_{us}$ of kaon decay, and (d) doubly-suppressed by $V_{cd}$ and $V_{us}$.

In this spirit, the first and simplest model proposed for the decay of charmed particles is the light-quark spectator model[5,17,18], in which the decay of a meson or baryon containing a charmed quark proceeds as it would for a free charmed quark. Figure 1.2(a) shows the corresponding valence quark diagram for Cabibbo-allowed hadronic D decay. In the absence of strong interactions and light quark masses, this model predicts equal lifetimes for all charmed particles, as well as semileptonic branching ratios of 20% (by counting the three different colors of quarks and the single 'color' of electron or muon doublet which can be produced at the final W vertex). In order to incorporate the effect of the strong interaction, radiative and virtual gluon corrections involving a single hadronic weak current must be considered[19], but have approximately the same effect on both the semileptonic and hadronic decay rates. Diagrams which involve the exchange of gluons between *different* weak hadronic currents, on the other hand, exist for hadronic decays only. The necessary modification of the inclusive hadronic decay rate is calculated within QCD in the following manner. The low-energy effective Hamiltonian for Cabibbo-allowed hadronic charm decay in the absence of strong interactions is written as:

$$H = \frac{G_F}{\sqrt{2}}[(\bar{s}c)(\bar{u}d)],$$

where parentheses indicate color singlet, left-handed $(V - A)$ currents. This can be formally rewritten:

$$H = \frac{G_F}{\sqrt{2}}[C_+O_+ + C_-O_-],$$

where

$$O_\pm = \frac{1}{2}[(\bar{s}c)(\bar{u}d) \pm (\bar{s}d)(\bar{u}c)],$$

and $C_+ = C_- = 1$. Hard (short-distance) gluonic exchange modifies the effective Hamiltonian by leaving the operator structure unchanged but changing the

numerical values of $C_+$ and $C_-$. The hard gluon corrections, which have been calculated within QCD both in leading log approximation[16] and in next-to-leading log approximation[20], enhance the $C_-$ operator coefficient over $C_+$, as seen in Figure 1.3 as a function of the renormalization point $\mu$. The natural choice for the parameter $\mu$ is the charmed quark mass, taken to be about 1.5 GeV. The inclusive hadronic decay rate is then proportional to $(2C_+^2 + C_-^2)$, resulting in semileptonic branching ratios:

$$B_e = \frac{1}{2 + 2C_+^2 + C_-^2} \, .$$

For 'reasonable' choices $\mu = 1.5\,\text{GeV}$ and $\Lambda_{\overline{MS}} = 0.250\,\text{GeV}$, the leading log corrections to the weak Hamiltonian give $C_+ = 0.7$, $C_- = 1.8$, and semileptonic branching ratios of 16%. The next-to-leading log calculation and consideration of radiative gluon diagrams[20] both decrease this value, to about 11%. The most uncertain remaining correction is the decreased phase space due to finite quark masses. It has been argued[21] that using constituent rather than current light quark masses may help take into account the confinement of the final state quarks into real hadrons. The larger constituent quark masses suppress the hadronic decay rate more than the semileptonic rate, leading to a slightly higher semileptonic branching ratio, estimated[12] as $(13 - 15)\%$.

The first measurements of $D^+$ and $D^0$ semileptonic branching ratios showed a significant difference between them, with Mark II[22] reporting $(16.8 \pm 6.4)\%$ and $(5.5 \pm 3.7)\%$, and DELCO[23] reporting $(22.0^{+4.4}_{-2.2})\%$ and less than 4.0% (at 95% confidence level) for $D^+$ and $D^0$, respectively. Isospin symmetry implies that the partial widths to Cabibbo-allowed semileptonic final states are equal for $D^+$ and $D^0$. Thus, to the extent that Cabibbo-suppressed semileptonic widths may be neglected, the ratio of semileptonic branching ratios is equal to the ratio of $D^+$ and $D^0$ lifetimes[21,24]. An early experiment which measured the D lifetimes directly in emulsion reported[25] $\tau(D^+) = (10.3^{+10.5}_{-4.1}) \times 10^{-13}$ sec, and
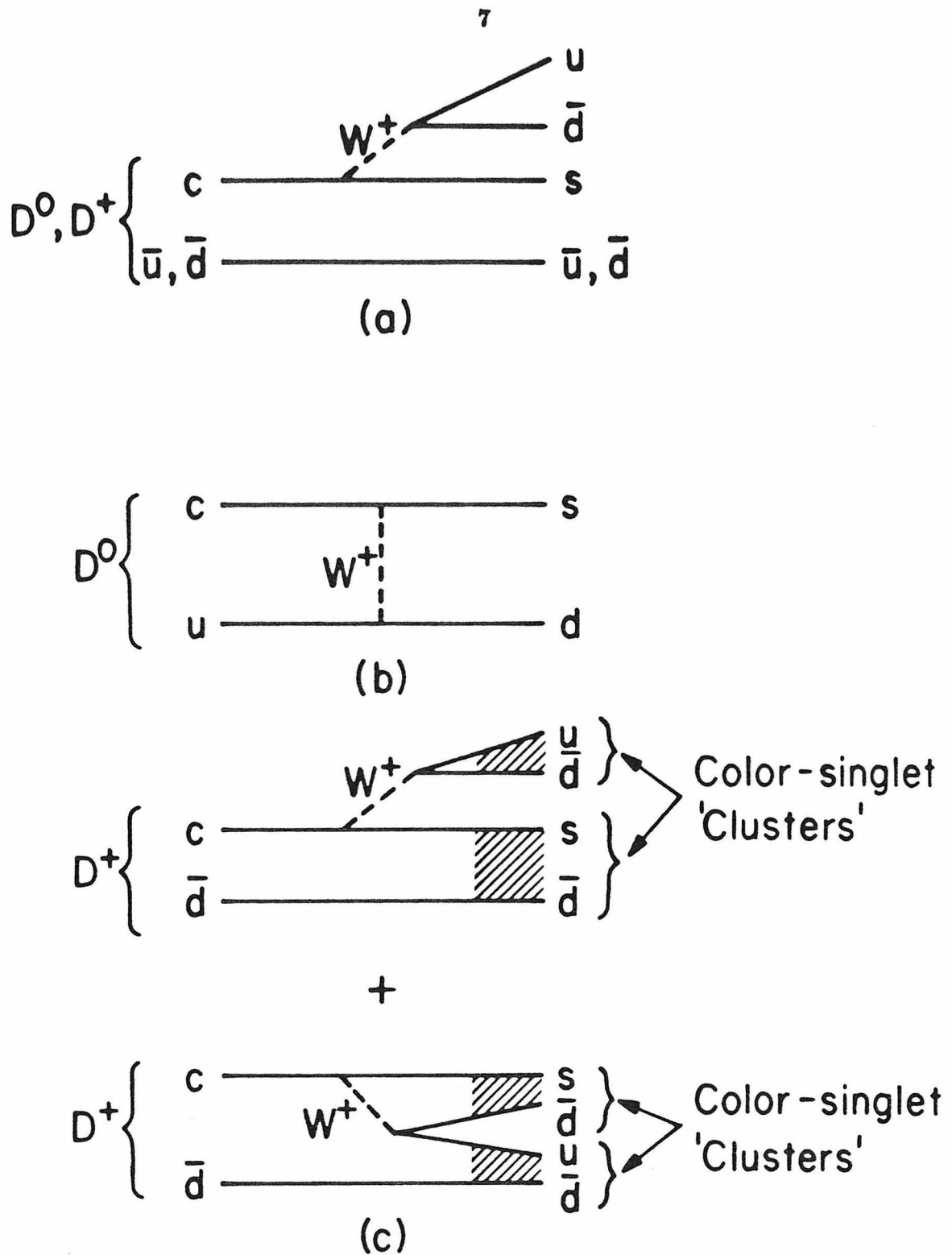
Figure 1.2. Valence quark diagrams for Cabibbo-allowed hadronic D decay via (a) the light-quark spectator model, (b) W-exchange, for $D^0$ only, and (c) showing possible interference between spectator diagrams leading to the same final state in $D^+$ decay.
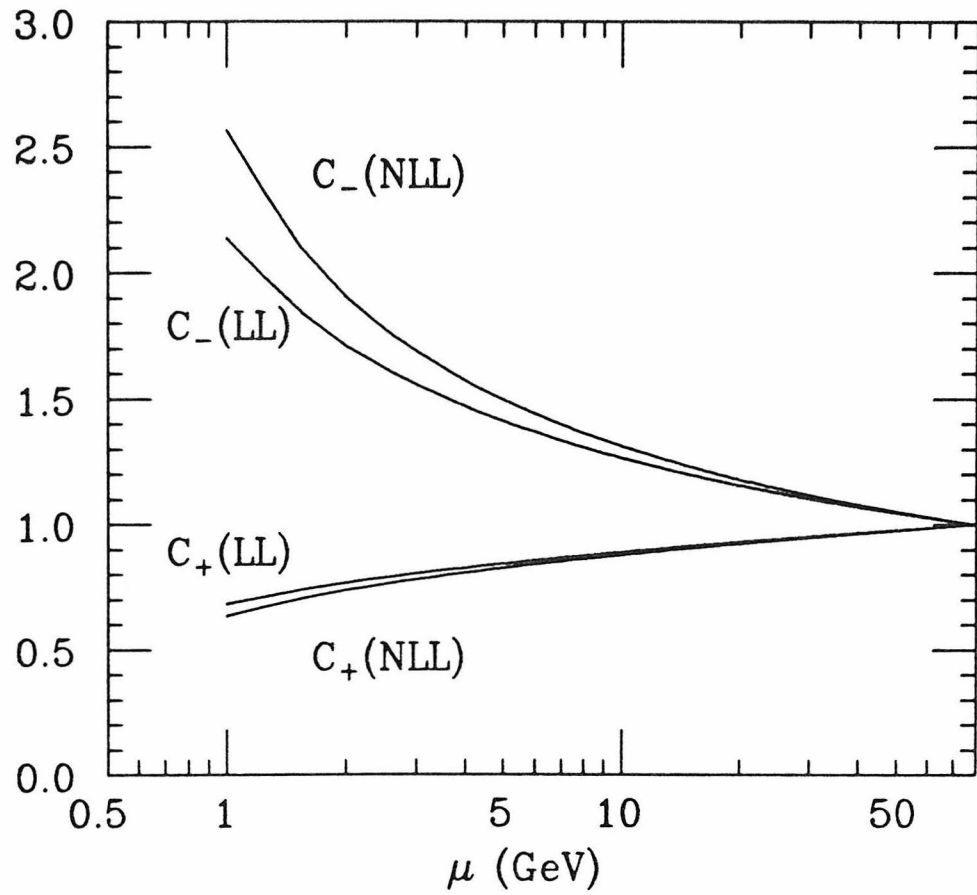
Figure 1.3. Variation of $C_+$ and $C_-$ operators with $\mu$ in leading log (LL) and next-to-leading log (NLL) approximations.

$\tau(D^0) = (1.00^{+0.52}_{-0.31}) \times 10^{-13}$ sec. By taking the ratio of semileptonic branching fractions to represent the ratio of lifetimes, and multiplying the likelihood functions for this ratio, the combination of these three early experiments[22] gives a ratio of $D^+$ to $D^0$ lifetimes:

$$\frac{\tau^+}{\tau^0} = 10.0^{+12.0}_{-4.6}.$$

The picture in early 1981 was thus one of complete disagreement with the spectator model prediction of equal charmed particle lifetimes and semileptonic branching ratios. Since that time, the D lifetimes have been measured by a large number of direct decay length experiments. These measurements individually have large statistical errors, but can be combined to yield the present world average values[26]:

$$\tau(D^+) = (8.8^{+0.9}_{-0.8} \pm 0.5) \quad \times 10^{-13} \text{ sec}$$
$$\tau(D^0) = (4.2 \pm 0.3 \pm 0.3) \times 10^{-13} \text{ sec,}$$

from which is derived:

$$\frac{\tau^+}{\tau^0} = 2.1 \pm 0.3 \pm 0.3.$$

This ratio is still in conflict with the spectator model, but perhaps less alarmingly so.

Rates to two-body hadronic final states from D meson decay can be derived within the spectator model by factorizing the decay matrix elements between color singlet quark-antiquark pairs which are taken to represent the mesonic final states[17,18], by analogy to semileptonic decays, where factorization is entirely valid. In hadronic decays, however, such a factorization can be criticized[27] for completely ignoring long distance QCD effects such as color transfer by soft gluons and final state interactions. Nevertheless, the predictions which follow can show striking dependence on the $C_+$ and $C_-$ operator coefficients, as in the ratio of the $D^0$ decay rate to $\bar{K}^0 \pi^0$ relative to $K^- \pi^+$ shown in Figure 1.4. The

small rate for $D^0 \rightarrow \bar{K}^0\pi^0$ relative to $K^-\pi^+$ ($\sim 1/40$) which is predicted by 'normal' values of $C_+$ and $C_-$ has been dubbed 'color suppression,' because it arises from a possible mis-match of colors between the pairs of quarks which must form the final state hadrons. In $D^0 \rightarrow K^-\pi^+$, however, the quarks are naturally paired into color singlets. In a parton model, it is easy to see that this suppresses the $\bar{K}^0\pi^0$ decay by a factor of 3 (for the three colors) in amplitude, or 9 in rate, from the $K^-\pi^+$ decay. This ratio has been measured[22] as $0.75 \pm 0.35$ based on observation of $(8.5 \pm 3.7)$ events in the $\bar{K}^0\pi^0$ channel, a result which differs greatly from the predicted suppression.

Several models have been proposed to deal with these discrepancies between the spectator model and the data on D meson decay. Perhaps the most popular model claims a significant enhancement of the total $D^0$ decay width from the non-spectator W-exchange diagram shown in Figure 1.2(b). Other non-spectator processes such as penguin diagrams (for both $D^+$ and $D^0$) and annihilation diagrams (for $D^+$ only) occur at a Cabibbo-suppressed level in D decays, and are not expected to significantly alter the total widths[28]. The attractive feature of the W-exchange model, besides the prediction of different lifetimes, is that it decreases the $D^0$ semileptonic branching ratio from that predicted in the light quark spectator model, as is experimentally observed, but does not modify the semileptonic branching ratio of the $D^+$. In order to reproduce the difference in lifetimes by this mechanism, the hadronic decays of the $D^0$ must be enhanced by about a factor of three. The decay amplitudes from the W-exchange diagrams were originally neglected because they are helicity-suppressed relative to spectator decays by the factor:

$$\frac{f_D^2 m_s^2}{m_c^4} \approx 10^{-3},$$

where $f_D$ is the D meson decay constant (estimated $\sim 0.2\,\text{GeV}$), as well as color suppressed. When gluons are considered, either by explicit calculation of
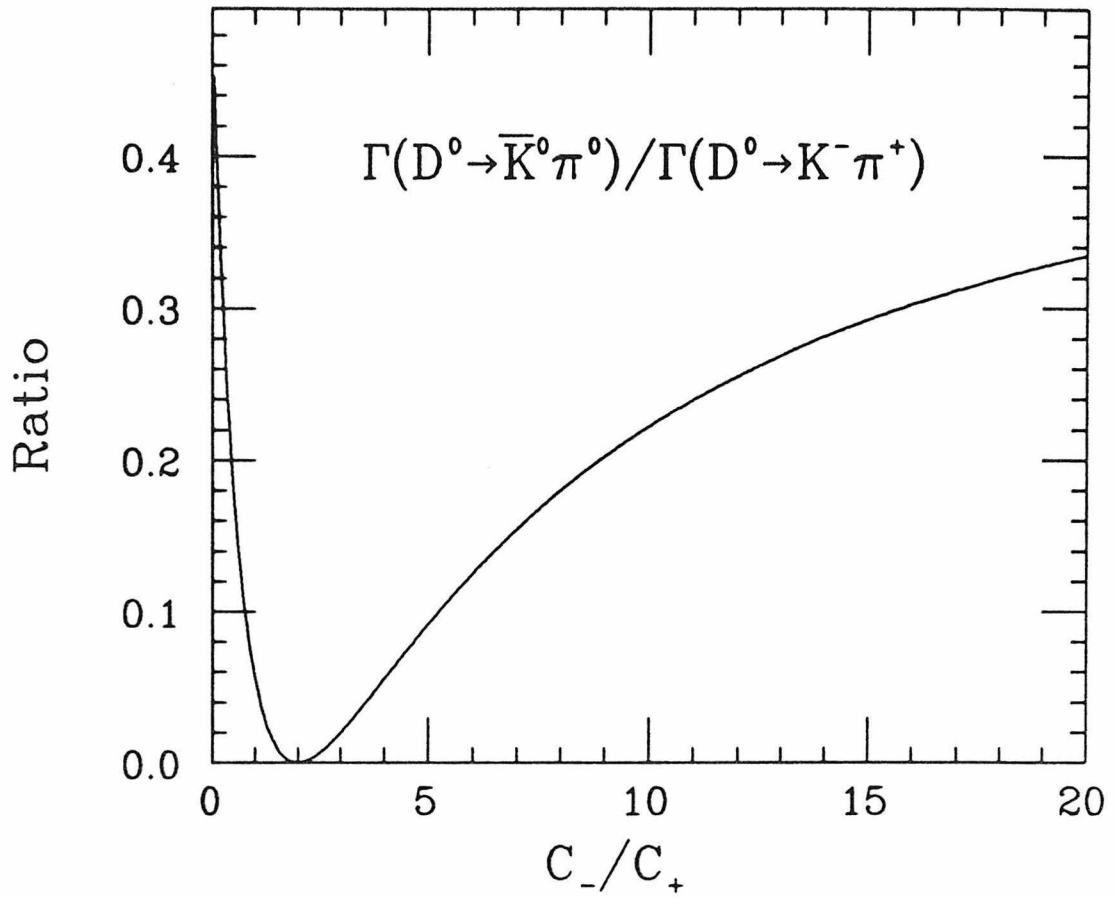
Figure 1.4. Variation of $\Gamma(D^0 \to \bar{K}^0\pi^0)/\Gamma(D^0 \to K^-\pi^+)$ with the ratio $(C_-/C_+)$ of operator coefficients in the spectator model (assuming factorization).

diagrams which include gluon emission from an initial-state quark line[29], or by assuming that the $D^0$ wavefunction includes a large intrinsic gluon component, represented[30] as $|c\bar{u}G\rangle$, then the quarks in the $D^0$ wavefunction can be in a color octet spin-1 state, and both types of suppression disappear. The rate for this type of decay depends on the overlap between the charmed and light quark wavefunctions at the origin, given by $f_D$. A perturbative QCD calculation of the decay rate from the W-exchange diagram with a gluon emitted from an initial-state quark line (essentially a radiative correction) gives[29]:

$$\frac{\Gamma_A}{\Gamma_{SP}} = \frac{2\pi\alpha_s}{27} \cdot \frac{(C_+ + C_-)^2}{(2C_+^2 + C_-^2)} \cdot \left[\frac{f_D}{m_u}\right]^2 \approx .03 - .09 \,,$$

using values $\alpha_s = 0.4$, $C_+ = 0.7$, $C_- = 1.8$, $m_u = 0.34\,\text{GeV}/c^2$, and a range of $0.150 - 0.280\,\text{GeV}$ for $f_D$. If the intrinsic gluon content of the D wavefunction is large, so that the probability for the quarks to be in a color octet spin-1 state is nearly unity, somewhat higher values for this ratio can be obtained[30]:

$$\frac{\Gamma_A}{\Gamma_{SP}} = \frac{4\pi^2}{3} \cdot \frac{(C_+ + C_-)^2}{(2C_+^2 + C_-^2)} \cdot \left[\frac{f_D}{m_D}\right]^2 \approx 0.13 - 0.44 \,,$$

using the same choices of parameters as in the previous equation. Thus, it is difficult[31], but perhaps not impossible, to account for the lifetime difference in this manner. Because final states from W-exchange are purely $I = 1/2$, a large contribution to the $D^0$ width also offers a means of enhancing the $\Gamma(D^0 \to \bar{K}^0\pi^0)/\Gamma(D^0 \to K^-\pi^+)$ ratio, to the value 1/2 attained in the absence of $I = 3/2$ contributions. Another consequence of this model could be a significant enhancement of $D^+$ Cabibbo-suppressed decays via the annihilation diagram[13]. Such decays require the presence of at least two gluons in the $D^+$ wavefunction to remove helicity suppression and provide a color singlet $c\bar{d}$ combination to couple to the $W^+$.

Experimentally, the existence of W-exchange graphs can be proven by observation of final states from $D^0$ decay which contain no $u\bar{u}$ content, and

can occur through W-exchange by creation of $d\bar{d}$ or $s\bar{s}$ pairs from the vacuum. Such decays occur through spectator diagrams only by OZI-suppressed processes in which the $u$ quark formed at the final W vertex annihilates the $\bar{u}$ quark contained in the $D^0$ wavefunction. The only Cabibbo-allowed state which is experimentally promising is $\bar{K}^0\phi$, which occurs through the W-exchange diagram with creation of an $s\bar{s}$ quark pair from the vacuum. The branching ratio for this decay is estimated[32] as $10^{-5} - 10^{-6}$ by OZI-suppressed spectator processes, but may have a branching ratio of $\sim (0.2 - 1.0)\%$ if the W-exchange diagrams are important. Among Cabibbo-suppressed states, one can search for, e.g., $K^0\bar{K}^0$, $K^{*0}\bar{K}^0$, or $\bar{K}^{*0}K^0$, which occur through W-exchange by creation of a $d\bar{d}$ pair from the vacuum.

Another explanation for the observed semileptonic branching ratios, the color cluster interference model[33], does not invoke non-spectator processes, but makes two fundamental assumptions. The first is that the ratio $(C_-/C_+)$, which is increased by QCD corrections to the weak Hamiltonian in leading log approximation and even more in the next-to-leading log calculation, is further enhanced for both $D^+$ and $D^0$ by non-perturbative effects[34], thereby increasing the hadronic decay rate close to that observed for the $D^0$. In order to decrease the $D^+$ hadronic decay rate, it is also postulated that the spectator decays proceed first by production of two color singlet quark-antiquark states, which then hadronize independently. In $D^0$ decay, the two possible amplitudes for production of the quark-antiquark pairs lead to different final states, while in $D^+$ decay, these amplitudes may lead to identical final states, as is shown in Figure 1.2(c). If these amplitudes interfere destructively, the rate for $D^+$ hadronic decay can be suppressed. In this picture, the decay of the $D^0$ is 'normal,' while the $D^+$ should decay relatively often into Cabibbo-suppressed final states[35]. Expressed in terms of flavor symmetry, a large $(C_-/C_+)$ ratio enhances the SU(4) 20-plet piece of the weak Hamiltonian containing both the charm-conserving SU(3) octet responsible for the $\Delta I = 1/2$ strange decays, as

well as a single charm-changing SU(3) sextet[36]. Because the charm-changing Hamiltonian transforms as a single SU(3) amplitude under 'sextet dominance,' the implications of a large $(C_-/C_+)$ ratio for charm decays can be expressed, without reference to any dynamical assumptions, in terms of simple SU(3) relations between various (especially two-body) decays[37,38]. Among these predictions are a suppression of all $D^+$ two-body decays to pairs of mesons from equivalent SU(3) octets, such as $D^+ \rightarrow \bar{K}^0 \pi^+$ and $D^+ \rightarrow \bar{K}^{*0} \rho^+$. The hypothesis of color cluster interference in $D^+$ decays extends this suppression to the inclusive $D^+$ decay rate.

The observation of charmed particles has proven to be quite difficult. Fixed target experiments using hadron beams or even photon beams suffer from large non-charm backgrounds unless they can observe the short length ($c\tau \approx 200\ \mu$m) between the production and decay vertices. In $e^+ e^-$ collisions at present accelerators the decay length is generally shorter than either the size of the interaction region or the spatial resolution of the detectors. Furthermore, the hadronic production rate decreases with increasing center-of-mass energy in $e^+ e^-$ machines (below the $Z^0$ pole), and that portion of the total cross-section which is due to charm production suffers from large combinatorial backgrounds.

In view of this situation, the $\psi(3770)$ resonance (hereafter referred to as the $\psi''$), which was discovered in $e^+ e^-$ collisions[39] just above charm threshold in 1977, offers several advantages for the detailed study of the weak decays of charmed particles. The $\psi''$, shown in Figure 1.5 as an enhancement in the total hadronic cross-section, is interpreted as the $1^3 D_1$ state of charmonium[40], which couples to $e^+ e^-$ by having mixed with the $2^3 S_1$ state (the $\psi'$). Lying above $D^0 \bar{D}^0$ and $D^+ D^-$ thresholds, but below $D\bar{D}^*$ or $D\bar{D}\pi$ thresholds, the $\psi''$ decays without OZI suppression to $D\bar{D}$ pairs, thereby acquiring a more typical hadronic decay width ($\Gamma \approx 0.025\ \text{GeV}/\text{c}^2$) which is larger than 100 times the width of the $\psi$ or the nearby $\psi'$.

Each D meson produced by the decay of the $\psi''$ in $e^+ e^-$ collisions has energy
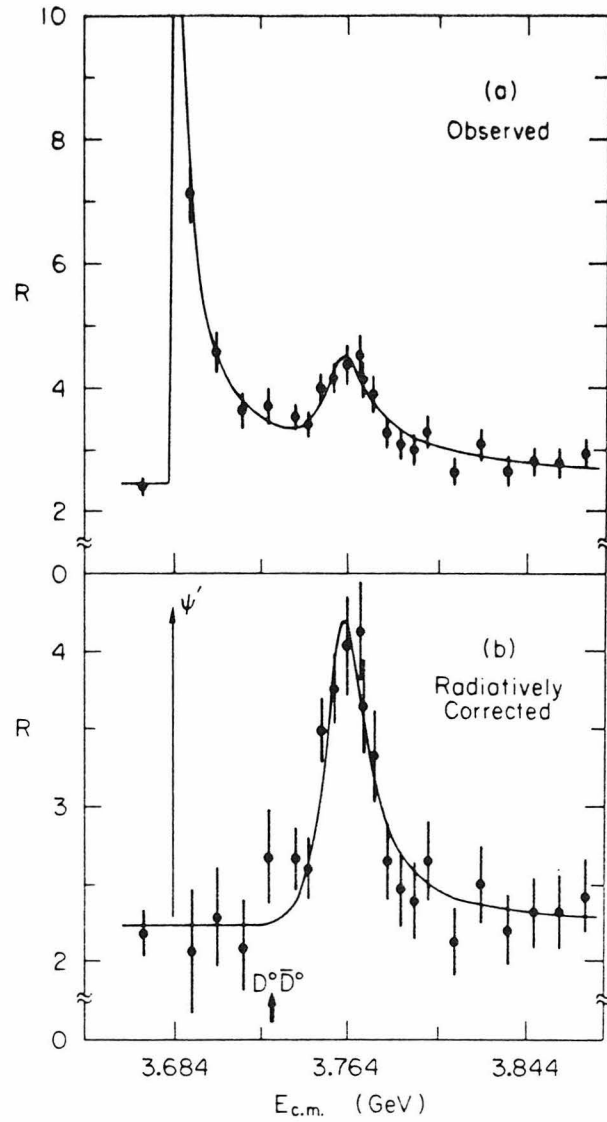
Figure 1.5. Mark II measurement of $R$ in the region of the $\psi''$.

equal to the beam energy. This can be used as a kinematic constraint to reduce backgrounds. Also, the production of $D^+D^-$ and $D^0\bar{D}^0$ pairs are equal by isospin symmetry, although the different masses, $m(D^+) = 1.869\,\mathrm{GeV}/c^2$ and $m(D^0) = 1.864\,\mathrm{GeV}/c^2$, slightly favor $D^0\bar{D}^0$ production by a ratio[41] of 56%/44% over $D^+D^-$ production. Thus, the number of $D^+D^-$ and $D^0\bar{D}^0$ pairs can be determined from a knowledge of the $\psi''$ cross-section and integrated luminosity, and used to normalize the calculation of branching ratios from observations of D decay into specific final states. Most of the known branching ratios of D mesons have been measured in this way by the Lead Glass Wall[42] (LGW) and Mark II[22] experiments at SPEAR.

This thesis presents measurements of D decay branching ratios, using data collected in the Mark III detector at SPEAR, which are sufficient in number and precision to allow, for the first time, a comprehensive picture of the hadronic decays of D mesons. The motivation is clear: to better understand the source of the difference between $D^+$ and $D^0$ lifetimes. The thesis is organized as follows. The Mark III detector hardware and some of the essential software tools are described in chapter 2. Measurements of exclusive Cabibbo-allowed and Cabibbo-suppressed hadronic D decays are presented in chapters 3 and 4, respectively. No evidence is seen for the $\bar{K}^0\phi$, $K^0\bar{K}^0$, and $(K^{*0}\bar{K}^0 + \bar{K}^{*0}K^0)$ final states from $D^0$ decay which would, if seen, prove the existence of W-exchange diagrams; upper limits are quoted. The $D^0$ and $D^+$ cross-sections in our data sample, necessary for normalization of branching ratios, are derived in a direct manner by a new 'double-tag' technique which is free of many ambiguities and problems which were faced by earlier experiments at SPEAR, which determined their cross-sections from the observed $\psi''$ line shape. The cross-sections thus determined lead to significantly higher branching ratios for well-known D decay modes than were previously measured. Chapter 5 presents measurements of individual $D^+$ and $D^0$ semileptonic decay branching fractions, derived by an analysis of the electron content in the recoil spectrum from fully reconstructed

hadronic D decays of known charm and charge. The ratio of $D^+$ and $D^0$ semileptonic branching fractions is determined with an accuracy comparable to the present world average of the ratio of lifetimes, and is found to be in agreement within the quoted errors. In the final chapter, these measurements are compared to the predictions of several models of charm decay.

## 2.  The Mark III Experiment

### 2.1  INTRODUCTION

Measurements presented in this thesis use data from in three separate runs taken at the $\psi''$: $1472\,\mathrm{nb}^{-1}$ collected in the fall of 1982, $3793\,\mathrm{nb}^{-1}$ collected in the spring of 1983, and $4060\,\mathrm{nb}^{-1}$ collected during the spring of 1984, for a total integrated luminosity of $9325\,\mathrm{nb}^{-1}$. During this time, the Mark III detector was located in the West pit at SPEAR. The following sections describe the $\psi''$ data sample, the Mark III detector, and critical Mark III software.

### 2.2  THE $\psi''$ DATA SAMPLE

Runs which are included in the $\psi''$ data sample have center-of-mass energy between 3.758 and 3.778 GeV. At the beginning of the 1982 data run, several hundred inverse nanobarns were collected at various energies during an attempt to better define the peak of the $\psi''$ resonance. The rest of the 1982 data was collected at 3.770 GeV, while the 1983 data was all taken at 3.768 GeV. During the 1984 run, SPEAR was set at a nominal energy of 3.768 GeV, but an actual energy of 3.764 GeV. This difference arose from a mechanical problem with the flip coil which is used to calibrate the SPEAR energy scale, and was only discovered much later when it was found that both $D^0$ and $D^+$ mesons were produced during that running period with lower momentum than expected from the recorded beam energy and the known D masses. As fortune would have it, this was the only $\psi''$ running period in which the calibration of the SPEAR energy scale was not checked by measuring the energy of the $\psi$ or $\psi'$ resonance peaks.

The performance of SPEAR is illustrated in Figure 2.1, which shows average luminosity over blocks of twenty data runs. The best average luminosity, $2. \times 10^{30}\,\mathrm{cm}^{-2}\mathrm{sec}^{-1}$, was reached during the 1983 run. The 1984 run had lower luminosity for unknown reasons.
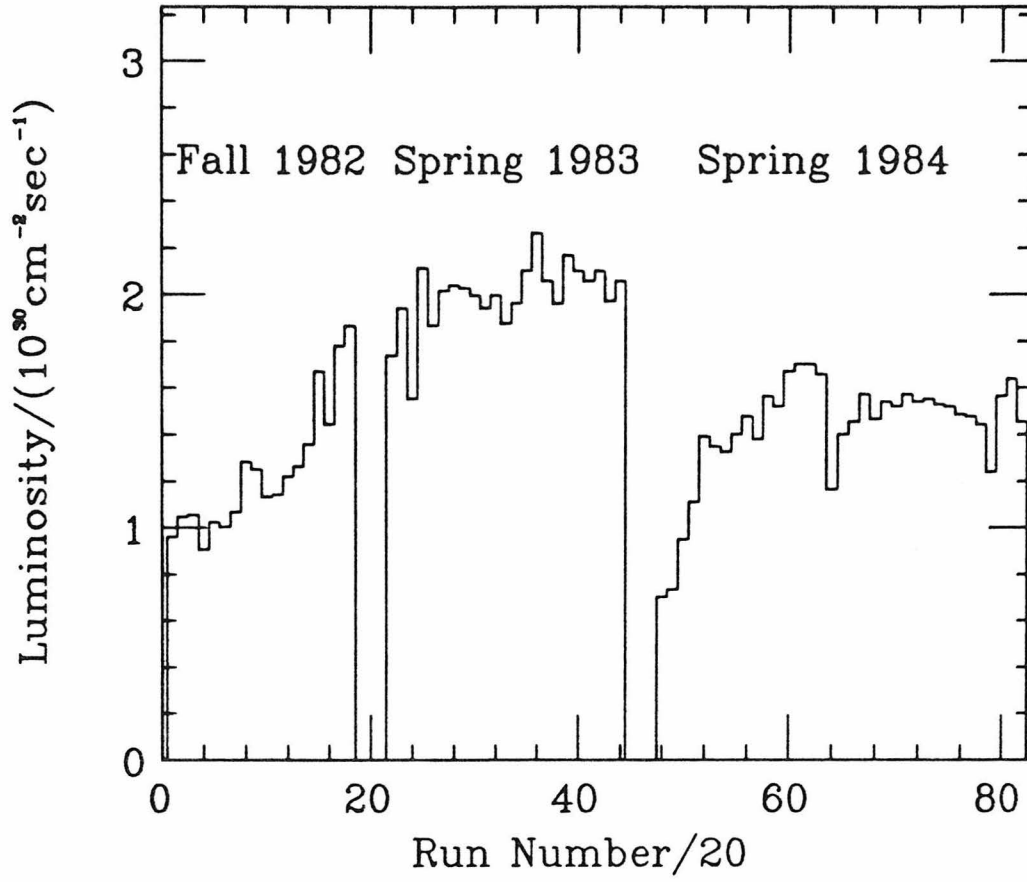
Figure 2.1. SPEAR luminosity during $\psi''$ running, averaged over 20-run blocks.

Luminosity is monitored online by a set of shower counters which detect small-angle Bhabha ($e^+e^- \rightarrow e^+e^-$) events. In this analysis, we use the more reliable technique of measuring integrated luminosity by comparing the number of large-angle Bhabha and di-muon ($e^+e^- \rightarrow \mu^+\mu^-$) events to the calculated third-order QED cross-sections[43]. The total integrated luminosities thus determined from Bhabha and di-muon events agree within 2%. We shall assign a 5% systematic error to the measurement of integrated luminosity over the entire $\psi''$ running period.

## 2.3 AN OVERVIEW OF THE MARK III DETECTOR

The Mark III follows several other detectors at SPEAR: Mark I, Mark I with the Lead Glass Wall, Mark II, DELCO, and the Crystal Ball. None of these experiments, however, combined the advantages of a magnetic detector with good efficiency for low-energy photons over a large solid angle. In $e^+e^-$ collisions at 3-4 GeV center-of-mass energy, typical charged particle and $\pi^0$ energies are only a few tenths of a GeV in hadronic events. In order to optimize the efficiency for detection of exclusive decays of charmed particles, the proposal for the Mark III therefore emphasized:

1.  Large solid angle for detection of photons and charged particles.

2.  Good efficiency for low-energy photons, which is achieved by placing the shower counter inside of the magnet coil.

3.  A minimal amount of material in front of and in the drift chambers, in order to minimize multiple Coulomb scattering, nuclear interactions, and photon conversions. For momenta below $1\,\mathrm{GeV/c}$, multiple Coulomb scattering dominates the error in momentum measurement in this detector.

4.  Good separation of charged pions, kaons, and protons having momentum below $1\,\mathrm{GeV/c}$ by TOF measurement, and additional particle separation by dE/dX measurement at low momenta where energy loss is approximately proportional to $1/\beta^2$.

5. Low cost. The magnet flux return steel is taken from the defunct Mark I, and the shower counters employ a relatively inexpensive lead-proportional tube design.

Following acceptance of the Mark III proposal in the spring of 1978 and the ensuing construction work, the detector was completed and installed in the West pit at SPEAR in the summer of 1981. Further work during the summer of 1982 included the addition of preamplifiers located at the face of the dE/dX layer of the main drift chamber, and read-out of four planes* of wires rather than two from the trigger drift chamber, bringing the performance of the detector up to its design goals. The detector and its major sub-systems are shown in cross-section in Figure 2.2.

The following sections briefly describe each of the major components of the Mark III detector and their performance during the $\psi''$ data runs. A much more detailed description of the entire detector can be found in Reference 44. Detailed descriptions are also available which are specific to the main drift chamber[45], TOF counters[46], barrel shower counter[47], endcap shower counters[48], and the trigger[49].

## 2.4 THE DRIFT CHAMBERS

The drift chambers for the Mark III detector consist of two sections: a 'trigger' drift chamber close to the beam pipe which consists of four planes of wires, and an outer 'main' drift chamber which contains a total of 28 wire planes.

The trigger drift chamber (layer 1), shown in cross-section in Figure 2.3(a), serves two distinct functions: to furnish points near the interaction region for tracking, and to reduce the trigger rate due to cosmic rays and beam gas while introducing a minimal amount of material into the detector.

Layer 1 supplies each track with axial (X-Y) information from four wire planes of radius between 0.098 and 0.134 m, as well as Z information by charge

---

\* Plane is used here to refer to a single cylindrical (!) array of sense wires.

Shower Counter

Drift Chamber

TOF Counter

Interaction
Region
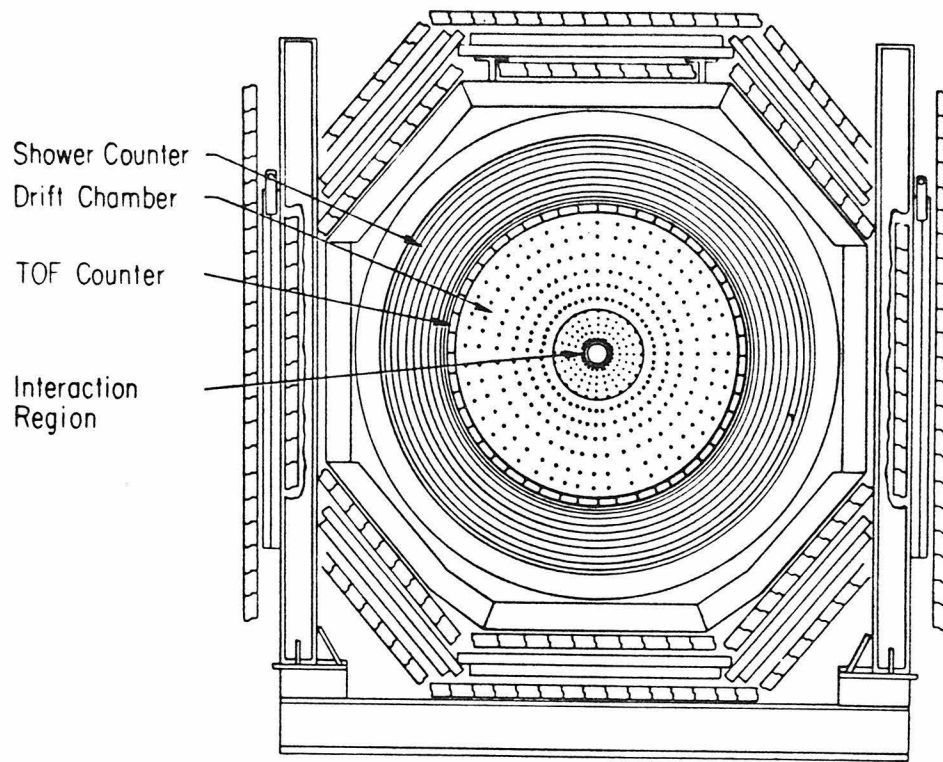
Figure 2.2. Axial view of the Mark III detector.
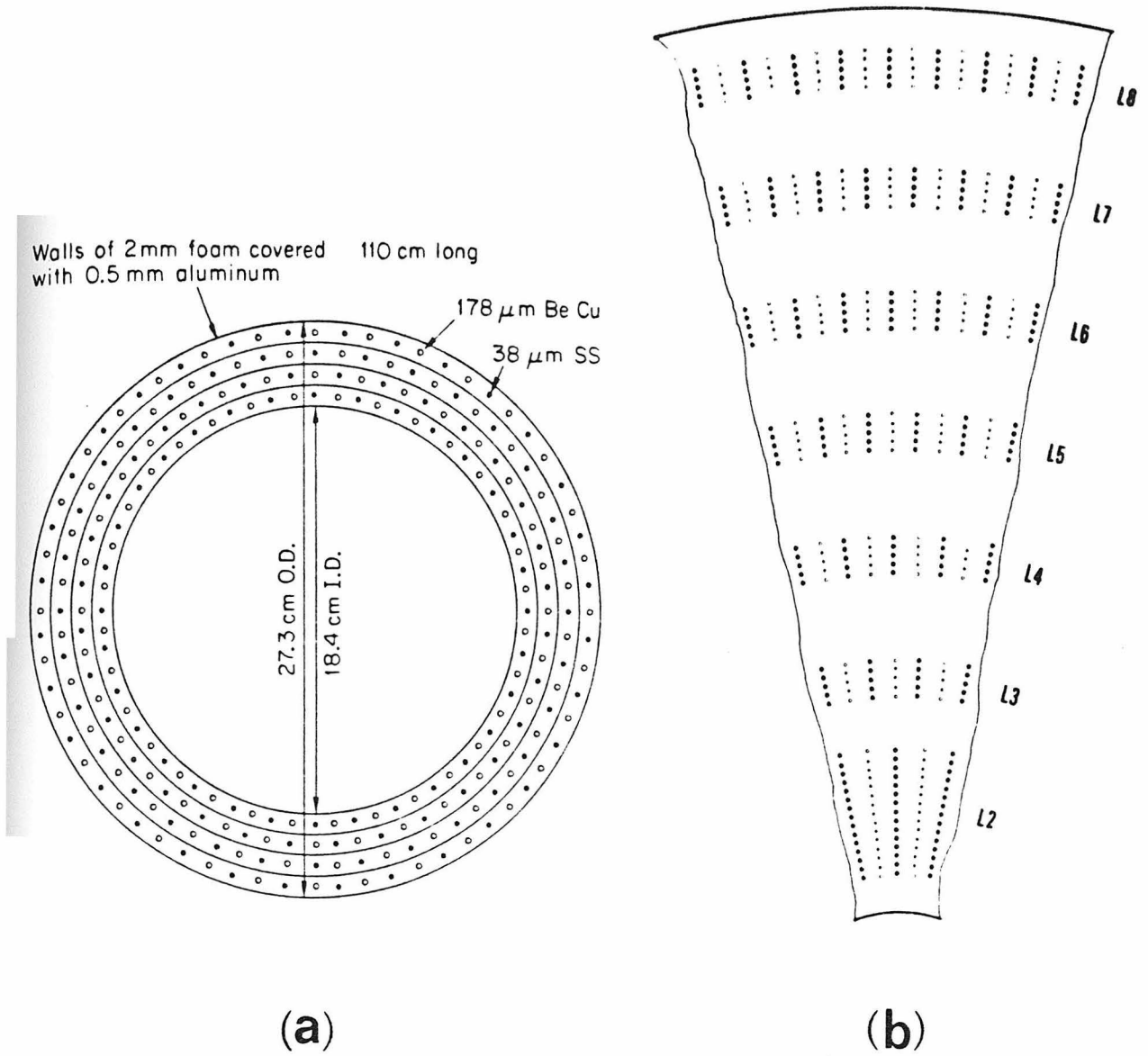
Figure 2.3. Mark III drift cell designs in (a) layer 1, and (b) layers 2-8.

division, using pulse height measurements from both ends of each sense wire. The long rise time of the preamplifiers for layer 1, necessary to reduce the amplitude of high-frequency pickup on the wires, as well as a non-uniform electric field configuration within each drift cell, lead to a poor spatial resolution of $\sigma \approx 350\,\mu\text{m}$. Nonetheless, the large solid angle covered by this layer (98% of $4\pi$), and the proximity of these measurements to the interaction region makes them quite useful in the identification of secondary vertices, improves the momentum resolution for high-momentum tracks, and helps the tracking of particles which exit the main drift chamber at low angles.

The use of layer 1 in the trigger is made possible by the $\frac{1}{2}$-cell offset between adjacent wire planes (see Figure 2.3(a) ). To the extent that the drift velocity is constant, the sum of drift times $(t_1 + t_2)$ from adjacent wire planes should be a constant offset from beam crossing for tracks traveling radially outward from the interaction region. Out-of-time cosmic rays, or curling tracks of very low momentum such as from beam-gas events, will have a displaced time sum. The distributions of $(t_1 + t_2)$ within the 100 ns time sum gate width for events which are classified as hadrons and for events which are classified as cosmic rays are shown in Figure 2.4. Given the 780 ns beam crossing interval, this gate reduces the trigger rate from cosmic rays by a factor of eight, to about 1 Hz.

The main drift chamber consists of seven layers of drift cells (defined as layers 2-8) having an inner radius of 0.185 m and an outer radius of 1.086 m. The innermost of these layers (layer 2) is 1.83 m long. Layer 2 contains twelve sense wire planes on which both drift time and charge deposition (for dE/dX) are measured. The remaining six layers, 2.39 m long, contain three sense wire planes on which only drift time is measured. Charges from induced pulses on the two guard wires in each cell in layers 3, 5, and 7 are added and then read out at both ends, giving a measurement of Z by charge division. Layers 4 and 6 are stereo, inclined at angles of 7.7° and −9.0°, respectively. Thus, a particle originating from the beam intersection region passes through as many as 34 planes of drift
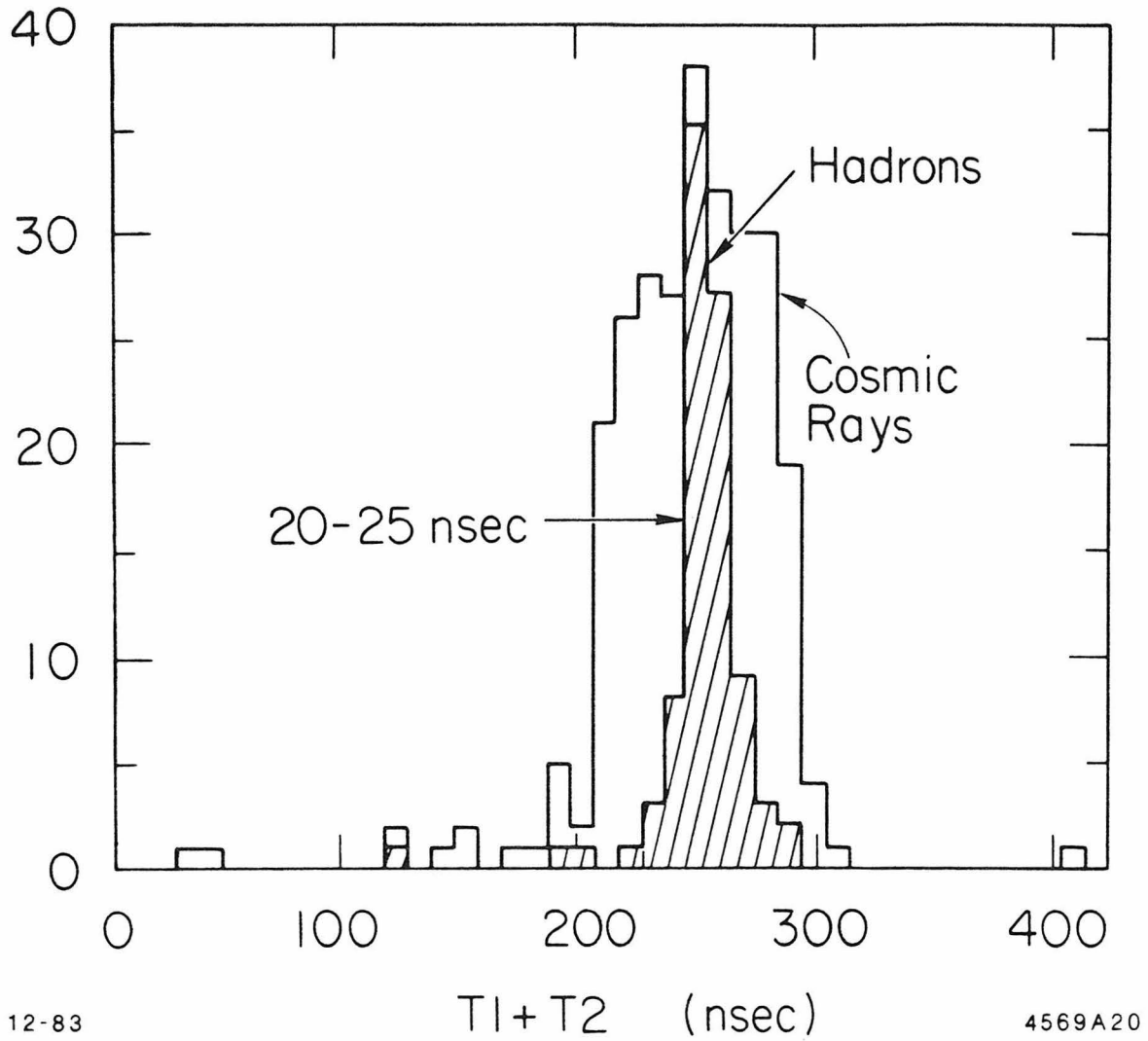
Figure 2.4. Distribution of layer 1 time sum $(t_1 + t_2)$ for hadrons and cosmic rays.

chamber wires.

The solid angle for tracking with all eight layers is 73%, while dip angle reconstruction with both stereo layers is possible over 84% of $4\pi$ solid angle. The $\cos\theta$ distribution of tracks from a clean sample of hadronic events is shown in Figure 2.5. This distribution, which should be flat for isotropic production and perfect tracking efficiency, shows that good tracking efficiency (with poorer momentum resolution) is achieved for tracks which reach layer 3, covering 94% of $4\pi$ solid angle. Drift length measurements in the trigger and main drift chambers combine to yield a momentum resolution for charged particles given by:

$$\sigma_p/p = \sqrt{(0.015)^2 + (0.015 \cdot p)^2}\,,$$

where $p$ is in GeV/c. The first term under the square root in this expression is the contribution from multiple Coulomb scattering, while the second term represents the error in the measurement of track sagitta. This implies $\sigma_p = 0.060\,\mathrm{GeV/c}$ for the muons of $1.878\,\mathrm{GeV/c}$ momentum from di-muon events at the average $\psi''$ center-of-mass energy of $3.766\,\mathrm{GeV}$. The observed momentum distribution, shown in Figure 2.6(a), is fitted to a Gaussian having mean $1.875\,\mathrm{GeV/c}$ and a slightly larger width than predicted, $\sigma_p = 0.064\,\mathrm{GeV/c}$, due to small non-Gaussian tails. When the position and size of the beam interaction region is used as a constraint in the helix fit for each track, the resolution improves to $\sigma_p = 0.051\,\mathrm{GeV/c}$, as shown in Figure 2.6(b).

The basic drift cell structures of layers 2-8 are shown in Figure 2.3(b). Typical spatial resolution in these layers is $\sigma \approx 250\,\mu\mathrm{m}$. Within each cell the sense wires are slightly staggered in order to decide whether a track passed to the left or to the right of the sense wires on the basis of the times within the cell alone. In layers 3-8 the stagger is $\pm 400\,\mu\mathrm{m}$, which is further increased near the center of the wires by electrostatic forces. With such a large stagger, the left-right decision can be made simply by forming the quantity $\frac{(t_1+t_3)}{2} - t_2$ from the individual time measurements. The distribution of this time sum is shown
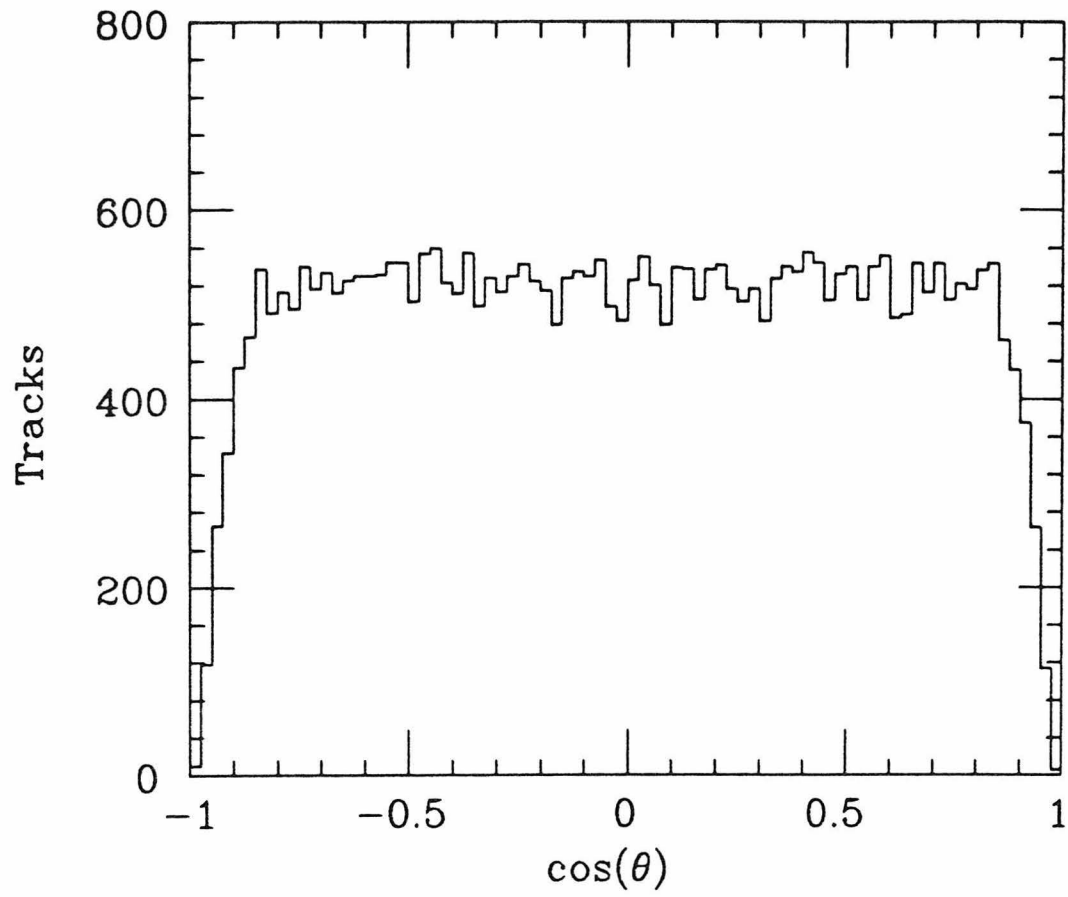
Figure 2.5. Distribution of $\cos\theta$ for charged tracks in hadronic events.
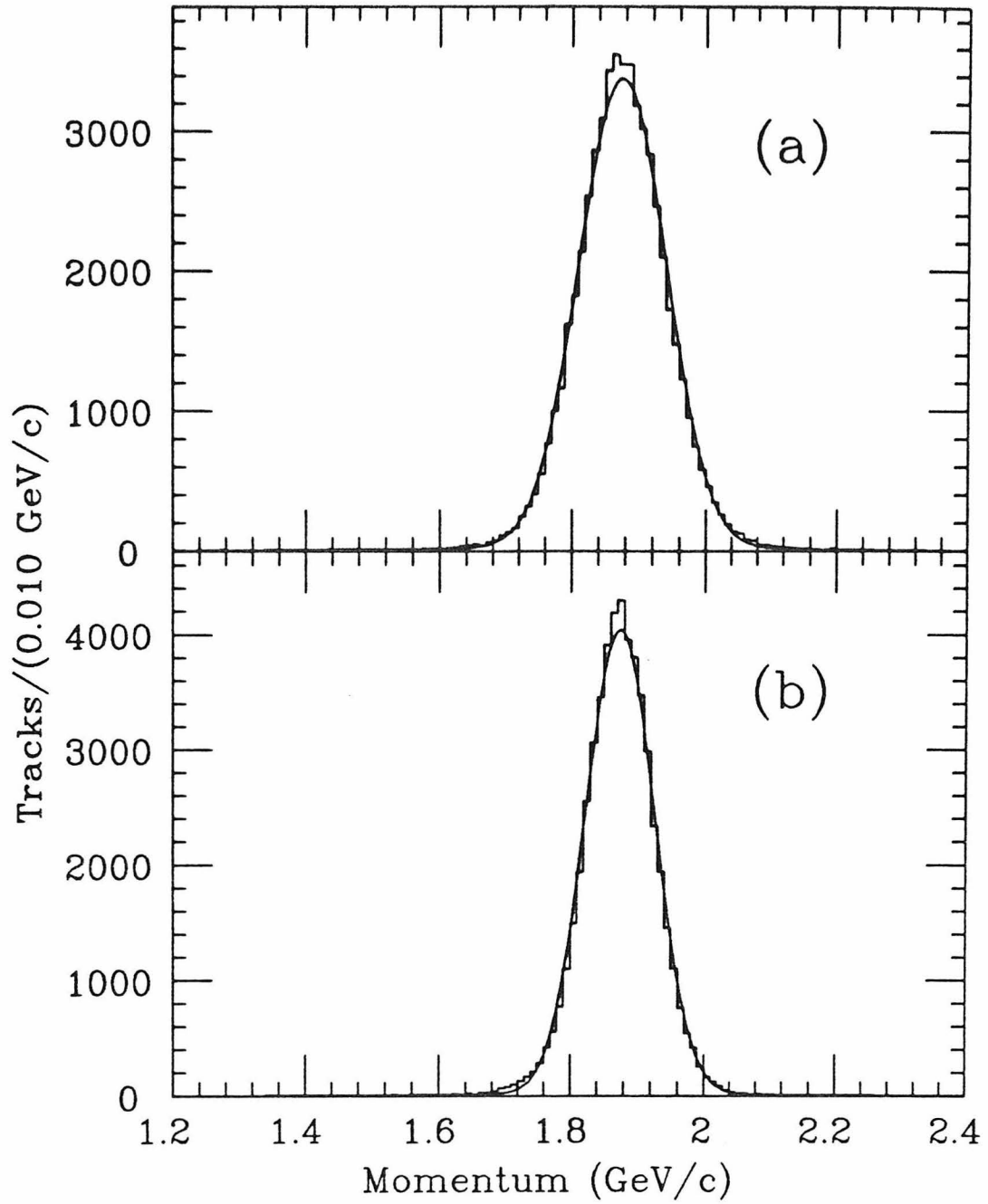
Figure 2.6. Momentum distributions for muons from di-muon events in the $\psi''$ data sample, using (a) one-track fits, and (b) 'vertex-constrained' fits.

in Figure 2.7. Although the wire stagger in layer 2 is only $\pm 150\,\mu$m, the twelve wire planes allow the left-right decision to be made by comparison of $\chi^2$ from fits on the left and right sides. For this purpose, a fit to a quadratic curve in X-Y is faster, and is adequate for tracks which do not curl up in the drift chamber.

Measurement of dE/dX in layer 2 is made possible by charge read-out on the twelve sense wires in each drift cell, representing twelve gas samples of 0.01 m thickness. Low gas gain is essential, not only to avoid gain saturation, but also to keep the wires from drawing excessive current: the wires are so close together and inaccessible in this layer that replacement of bad or missing wires has proven to be a nearly impossible task! Low-noise preamplifier cards which provide a gain of twenty are placed on the face of layer 2 to amplify the tiny ($\sim 200\,\mu$V) signals. The dE/dX measurements are not used for data taken during the fall 1982 run, because the 500 ns gate length for charge collection used during that run (thereafter lengthened to 1000 ns) was too short and introduced large drift time-dependent effects. Figure 2.8 shows the averaged dE/dX pulse height after angular corrections and truncation of large pulse heights. The width of the energy loss distribution at a particular momentum is approximately $\sigma = 17\%$ of the peak value. Separation of charged kaons from pions by dE/dX is apparent in the $1/\beta^2$ region of energy loss, reaching $3.3\sigma$ at 0.4 GeV/c momentum, but decreasing to $1.7\sigma$ at 0.6 GeV/c.

Time measurements from stereo layers 4 and 6 determine Z at each stereo wire plane with a resolution of $\sigma_z \approx 2$ mm. The 0.27 m lever arm between the stereo layers thus provides adequate track dip angle resolution of $\sigma_\theta \approx 10$ mr, while the three time measurements within a single stereo layer provide inadequate dip angle resolution of only $\sigma_\theta \approx 150$ mr. However, it is often difficult to assign correct stereo information from both stereo layers to a track. If a track passes through a stereo layer within several cells of another track in X-Y projection, the assignment of stereo cells may be ambiguous. If two tracks pass through the same stereo cell, stereo information is necessarily lost. Finally, if the left-right
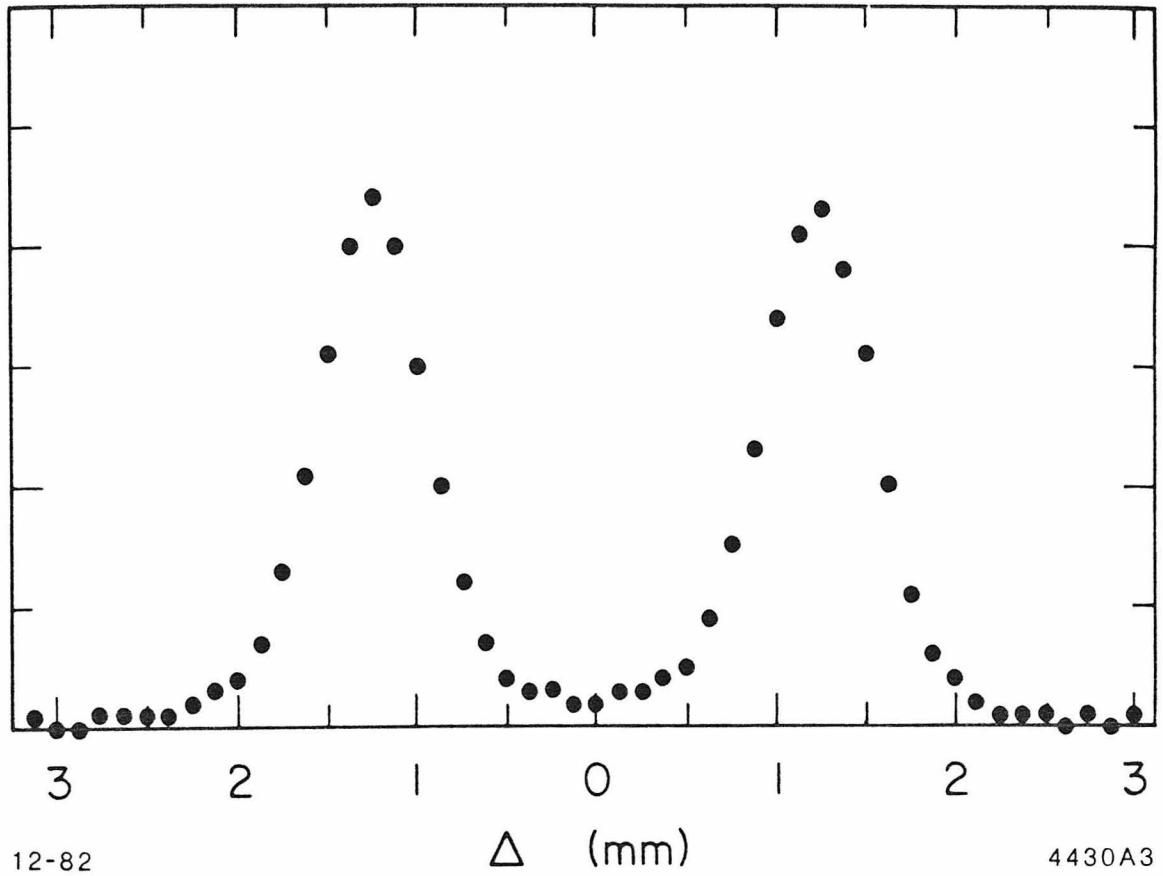
Figure 2.7. Left-right determination using $\frac{(t_1+t_3)}{2} - t_2$ in drift chamber layers 3-8.
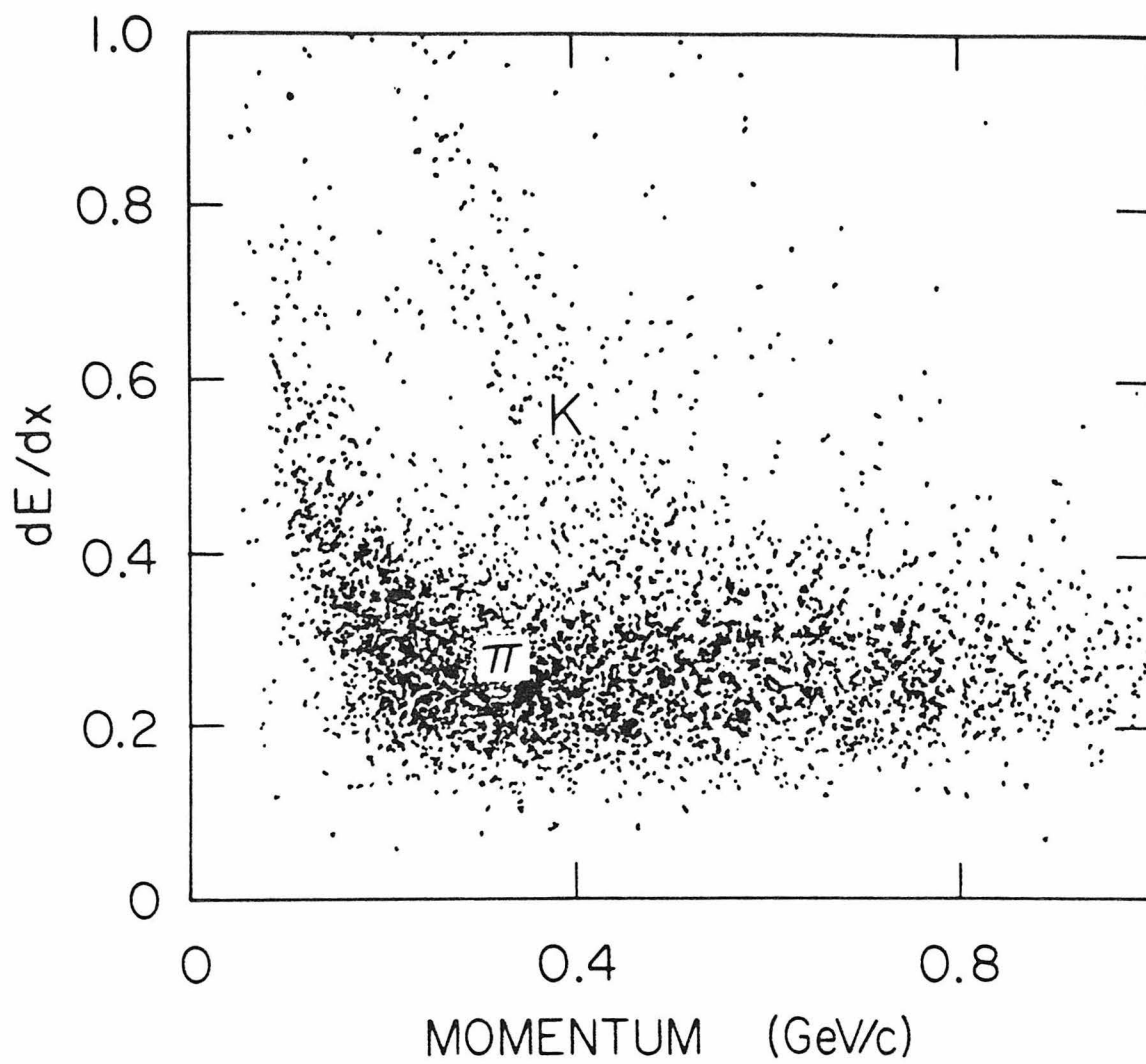
Figure 2.8. Layer 2 dE/dX pulse height versus momentum.

assignment within a stereo cell is incorrect, as happens in $1 - 2\%$ of the cases, the dip angle determination will be ruined.

The charge division information from layers 1, 3, 5, and 7 complements the dip angle information from the stereo layers. In layer 1, however, the measurements for steeply dipping tracks are often lost because the large pulses overflow the range of the amplitude-to-digital (ADC) conversion. Non-linear charge corrections are required in all charge division layers, and large cross-talk from tracks passing through adjacent cells and layers is observed. Charge division resolution in layers 5 and 7 is $\sigma_z \approx 0.05\,\mathrm{m}$ under optimal conditions. Resolution in layer 3 is degraded to $\sigma_z \approx 0.08\,\mathrm{m}$, apparently because of pick-up on the drift chamber wires. Charge division has thus proven to be of marginal utility.

Because of the problems with Z reconstruction, the first Mark III drift chamber tracking program often arbitrarily assigns Z=0 to the point of closest approach of a track to the beam position in axial (X-Y) projection. In addition to an average and systematic error equal to the size of the interaction region ($\sigma_z \approx 0.025\,\mathrm{m}$) in real $e^+e^-$ collision events, this assignment often gives absurd results for well-detached secondary vertices and for cosmic ray or beam-gas events. Dissatisfaction with the first-generation tracking program led to the development of a new and radically different second-generation tracking program, which is described in detail in Appendix A of this thesis[50].

## 2.5   THE TIME-OF-FLIGHT SYSTEM

Strapped onto the outside aluminum shell of the main drift chamber is a cylindrical array of time-of-flight (TOF) scintillation counters at $1.2\,\mathrm{m}$ radius, covering 80% of the $4\pi$ solid angle. These counters are $0.05\,\mathrm{m}$ thick, $0.16\,\mathrm{m}$ wide, and $3.2\,\mathrm{m}$ long, made of Nuclear Enterprises Pilot F scintillator. Attached to the ends of the counters are light guides which bring the light outside of the magnet flux return steel to 2 inch Amperex XP2020 phototubes. The thickness of the scintillator, shape of the light guides, and choice of the photomultipliers were all

optimized on the basis of Monte Carlo studies which determined the number and arrival time dispersion of the first photons, which are most critical for the time measurement.

The times when the pulse from the photomultiplier crosses two different discriminator thresholds and the charge collected are recorded from each end of struck counters. These time measurements are relative to the beam crossing time supplied by a beam 'pick-off' electrode. The entire system is calibrated online by a $N_2$ laser which pulses the counters through fiber optic cables. Offline corrections are determined by using either Bhabha or di-muon events, which have tracks arriving at known times relative to beam crossing. Corrections to the raw times are determined separately for each counter, and consist of a time pedestal subtraction, and adjustments which are polynomial in measured pulse height and Z of the track in the TOF counter. In practice, only the time from the lower discriminator threshold has proven useful. Although the time residual distribution has long non-Gaussian tails, the resolution for hadrons near its peak is about 200 ps. A scatter plot of $\beta$ determined from TOF versus momentum measured by the drift chamber is shown in Figure 2.9, indicating good $\pi$-K separation out to 1 GeV/c momentum.

## 2.6 THE SHOWER COUNTER

The Mark III shower counter consists of three modules: a barrel section covering 80% of $4\pi$ sr., and two endcap sections which extend coverage to 95% of $4\pi$ sr. These modules share a common design having 24 layers of proportional tubes interleaved with lead-aluminum sandwiches of $\frac{1}{2}$ radiation length thickness. The front six layers are read out individually, while the back eighteen layers are read out in groups of three layers. The coordinate along the wire direction is determined by charge division on the resistive stainless steel sense wires. In the 80% argon, 20% methane gas mixture used, this design yields an energy
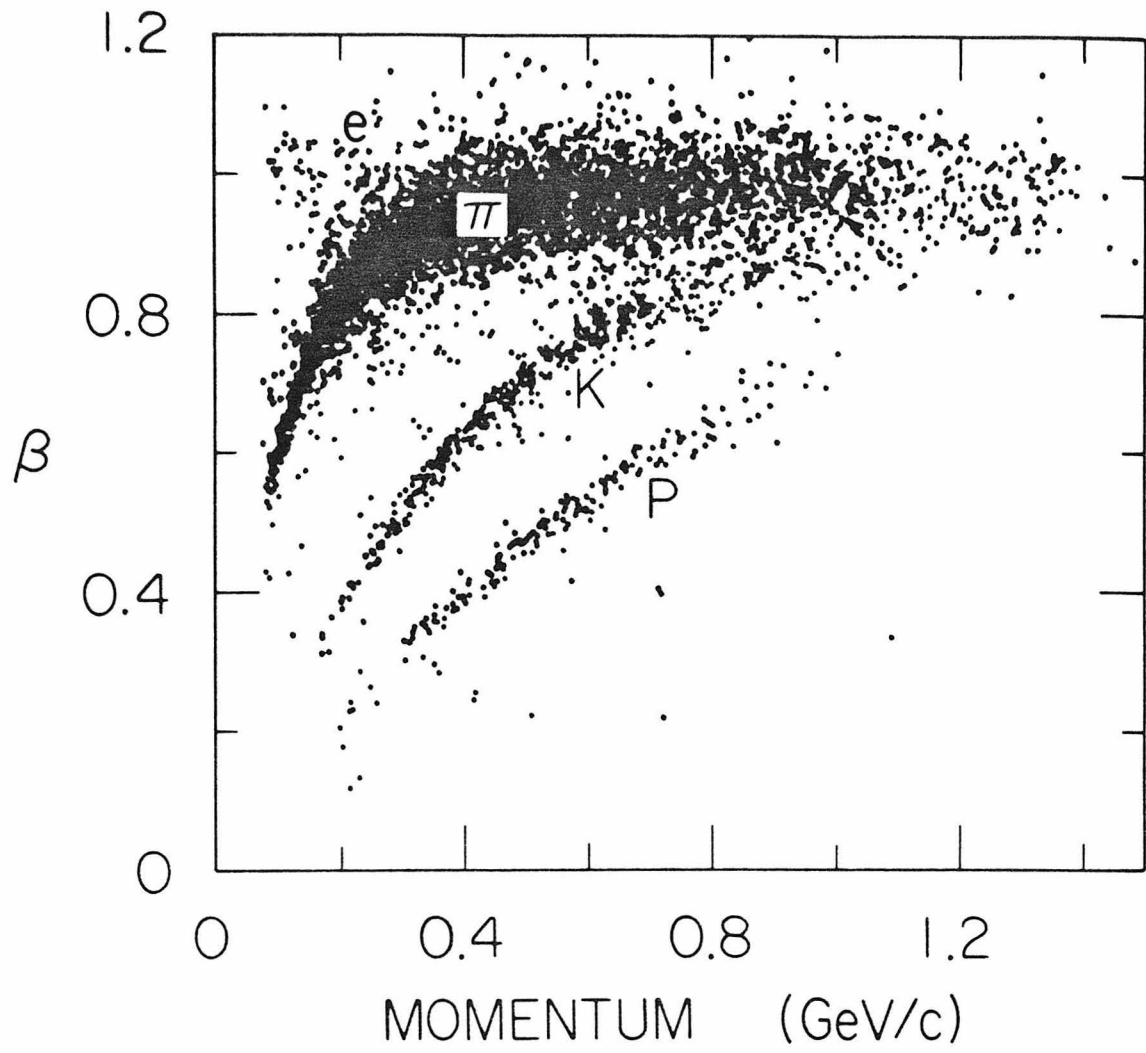
Figure 2.9. $\beta$ from TOF versus momentum.

resolution for photons which is well described by:

$$\frac{\sigma_E}{E} = \frac{18\%}{\sqrt{E}},$$

where E is in GeV.

The barrel section is divided in $\phi$ by thin aluminum I-beams into 320 proportional tubes per layer, resulting in a resolution of $\sigma_\phi = 7$ mr. The $46\,\mu$m sense wires have $2000\,\Omega$ resistance and yield a charge division resolution of 0.8% of their 3.5 m length. At the 1.3 m inner radius of the barrel section, this corresponds to a $\sigma_\theta = 20$ mr determination of polar angle. Each layer is supported by five longitudinally spaced circular aluminum ribs. These ribs absorb some fraction of nearby showers, and thereby decrease the amount of energy measured in their vicinity.

The proportional tubes in the endcap sections are made of $27.1 \times 11.7$ mm thin-walled rectangular aluminum tubes. Performance of the endcaps is quite similar to that of the barrel, although the shorter sense wires of $37\,\mu$m diameter allow, in principle, a better determination of position along the wire direction.

The photon detection efficiency has been measured using the monochromatic $\pi^0$ from $\psi \to \rho^0\pi^0$ events. The $\pi^0$ decay produces a flat photon energy spectrum which extends from 0.003 to 1.55 GeV. The efficiency thus determined is shown as a function of energy in Figure 2.10, reaching nearly 100% for 0.100 GeV photons.

## 2.7   THE MAGNET

The Mark III magnet coil is wound with four layers of $5 \times 5$ cm aluminum conductor. The designed 0.4 T field is generated by a current of 4400 amps. This current dissipates 1 MW as heat in the coil which is carried away by water pumped through 2.5 cm circular holes in the center of each conductor. In addition, two small compensator magnets are located near the beam axis at $\pm 2$ m from the interaction region in Z. These magnets cancel the line integral of magnetic field along the beam direction, which otherwise would couple the large
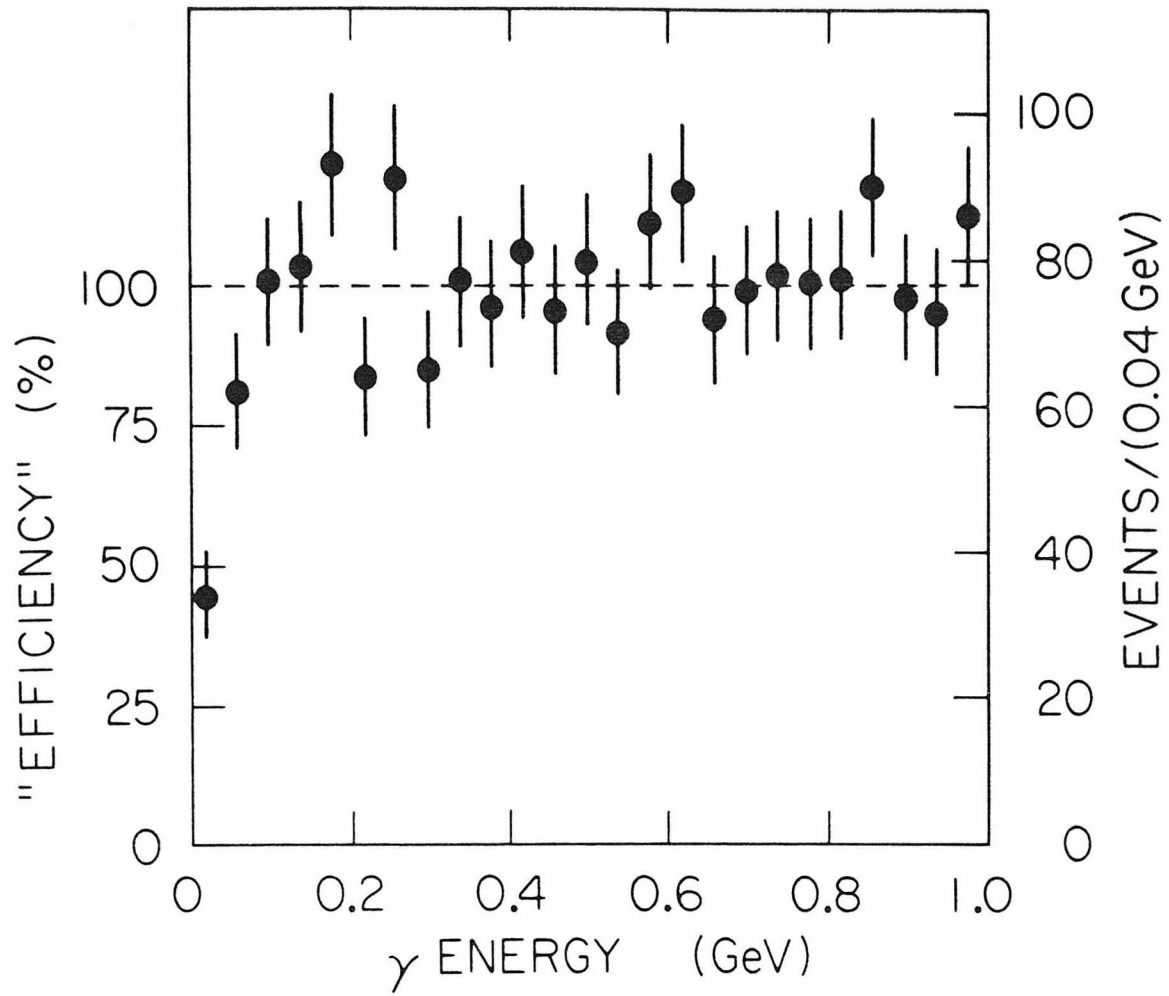
Figure 2.10. Photon efficiency as a function of energy.

horizontal and vertical betatron oscillations. The magnetic field was mapped by Hall probes on a long arm with the coil mounted inside the flux return steel, before the detector was installed. The detector itself contains no magnetic materials. A total of 17 parameters describes the magnetic field to an accuracy of 0.2% over the drift chamber tracking volume. Six of these parameters determine the relative orientation and displacement between the coordinate system used to describe the magnetic field and the coordinate system of the drift chamber. Two parameters describe the dipole fields due to the small compensator magnets. The final nine parameters, which are used to describe the field of the main coil in cylindrical coordinates, are the coefficients of orthogonal polynomials in R and Z, each of which satisfies $\vec{\nabla} \cdot \vec{B} = 0$ identically. Within the volume of the drift chamber, the Z component of the field is uniform to within 6%. During actual data taking, the readings of a single NMR probe located within the coil are used to determine the overall scale of the magnetic field.

## 2.8 THE MUON SYSTEM

Outside of the magnet flux return steel are two layers of proportional tubes, separated by an additional 0.12 m of steel, which cover 65% of the $4\pi$ solid angle. These tubes provide separation of muons from pions, as pions have a high probability of hadronic interaction within the steel. The efficiency for detection of muons by the muon system within its solid angle, as measured in radiative di-muon events from the $\psi''$ data sample, is shown in Figure 2.11(a). Muons with momentum below 0.6 GeV/c stop in the magnet steel. The muon counters are thus insensitive to a large fraction of the muon spectrum from semileptonic D decays, which peaks near 0.5 GeV/c. In addition, there is a substantial probability that a pion will 'punch-through' and be identified as a muon, as can be seen from Figure 2.11(b). The main use of the muon counters has been in detection of the di-muon events used to determine luminosity. For these muons of 1.884 GeV/c momentum, the system is fully efficient.
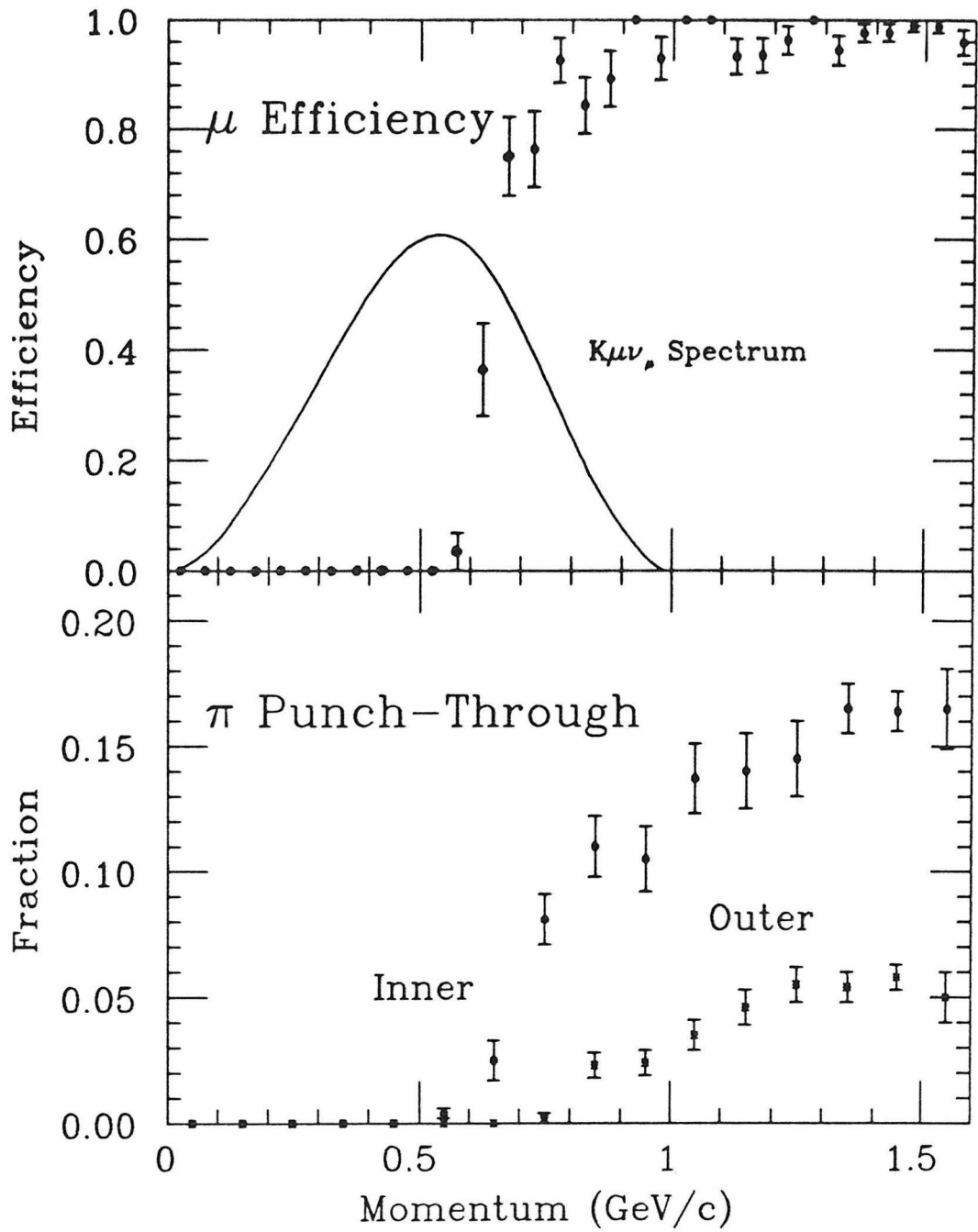
Figure 2.11. Muon system performance: (a) efficiency for detection of muons, and (b) probability that a pion will 'punch-through' and be identified as a muon.

## 2.9 THE TRIGGER

Three levels may be employed in making the decision to trigger the Mark III. The level 1 trigger looks for a valid time sum in at least one cell in layer 1, and may, in addition, require a TOF hit. This decision takes place within 590 ns after beam crossing, so that the electronics may be reset before the next beam crossing at 780 ns if the level 1 trigger is not satisfied. The level 2 trigger looks for tracks in the drift chamber by combining signals from each cell in layer 5 in coincidence with signals from the appropriate cells in layers 1 and 3. The lower momentum limit imposed by the allowed coincidences is 0.050 GeV/c for the $\psi''$ data set, although this limit can be adjusted between 0.050 GeV/c and 0.250 GeV/c. The level 2 trigger decision takes place within one additional beam crossing. Finally, a third trigger level looks at charge division information from layers 1, 3, and 5 to determine whether tracks originate from the beam intersection region. This third level decision was never actually used during $\psi''$ running, due to the poor quality of the charge division information.

At the $\psi''$, the level 1 trigger is satisfied at a $(4 - 10)$ KHz rate, contributing a dead time of less than 1% from operation of the level 2 trigger. The event rate is typically 4 Hz, most of which is either cosmic rays or beam-gas scattering. Read-out of the electronics takes $\sim 25$ ms, and is thus the source of 10% dead time. During $\psi''$ running, events were logged to tape according to a '$1\frac{1}{2}$-track' trigger, which requires at least two drift chamber tracks, or one drift chamber track plus a TOF hit. Since a D meson decay is generally uncorrelated with the decay of the recoil D, and because all modes studied thus far involve at least one charged track, this loose trigger requirement introduces almost no loss of data.

## 2.10 THE EVENT FILTER AND RECONSTRUCTION PROGRAMS

Much of the data logged to tape are cosmic ray and beam-gas scattering events. Most of these events are removed from the analysis stream before full event reconstruction by simple cuts contained in the Mark III data filter program.

The following information causes an event to be rejected by this program:

1. Exactly two back-to-back TOF counter hits with a time difference of approximately 8 ns (rejects cosmic rays).

2. Two charged tracks with no shower energy deposition (rejects beam-gas events).

3. One charged track in the event with very little or very asymmetric shower energy deposition (rejects beam-gas events).

These cuts remove about 2/3 of the logged events. Thousands of events were scanned by hand to make sure that no interesting hadronic, di-muon, or Bhabha events are rejected in the process.

After an event passes the filter, event reconstruction takes the raw data, e.g., drift time measurements, shower counter pulse heights, etc., applies necessary corrections, and transforms it into a form suitable for physics analysis.

The first step in this process is to find charged tracks in the drift chambers and properly associate them with drift length and charge division measurements. The measurements from each track are then fitted to a series of linked helices (which would be a single helix in the absence of magnetic field variations) in order to determine the particle trajectory and extract the best possible estimate of the magnitude and direction of the particle's momentum at its point of closest approach to the primary vertex. If a trajectory is consistent with having come from the primary vertex, a better 'vertex-constrained' measurement can be made by including the position of the beam interaction region, with appropriate errors, in the helix fit (compare Figure 2.6(a) to Figure 2.6(b)).

Pulse height measurements from layer 2 of the drift chamber are then associated with each track, and corrections for the effect of temperature variations on the gas gain, and for drift time dependence are applied. Because of Landau fluctuations, a better estimate of expected energy loss is made by deleting the largest (typically 30%) of the individual pulse height measurements before taking an average. The expected energy loss is computed using the Landau-

Sternheimer formula[51]:

$$\frac{dE}{dX} = \left(\frac{N}{\beta^2}\right)\left[8.991 + \ln(\gamma^2) - \beta^2 - \delta\right]$$

for the most probable ionization, where $\delta$ is the Sternheimer density effect and $N$ is a normalization constant, and then scaled by path length through the drift cell. The number of standard deviations between the measured and expected energy losses is then computed for each $\pi/K/p$ hypothesis.

Time measurements in the TOF counters are associated with charged tracks by comparison of the $\phi$ of the counter and the Z position determined by the relative amounts of charge collected by the phototubes on each end of the counter, with the entrance point of the particle in the TOF as determined from the drift chamber trajectory. TOF weights $(W)$ are assigned for each particle hypothesis which correspond to the deviation of the measured time $(t_m)$ from the expected time of flight $(t_{pred})$:

$$W = e^{-\frac{1}{2}\left(\frac{t_m - t_{pred}}{\sigma_t}\right)^2}.$$

The raw data from the shower counters consists of charge-division measurements from each end of wires which have collected charge, thus determining the positions of energy deposition in all three dimensions. The shower reconstruction program attempts to group these measurements into more-or-less contiguous 'clusters'. Each cluster is assigned an energy under the assumption that the charge deposited results from an electromagnetic shower of a photon or electron. The shower counter energy scale is calibrated using the electrons from Bhabha events. When the mean position of a cluster is sufficiently close to the entrance point of a charged particle into the shower counters, it is associated with that track. Remaining clusters are then presumed to be photons. One problem encountered is that charged hadrons which interact in the shower counter tend to produce 'split-offs,' which are secondary interactions occurring far enough from the main shower so that they are considered separate showers,

and thus become a source of fake photons. These are rejected by ignoring all candidate photons found within 18° of a charged track at its point of entrance into the shower counters.

## 2.11 THE MONTE CARLO SIMULATION

A Monte Carlo simulation is the most appropriate method for determining efficiencies in a complicated detector. There are two main parts of such a simulation: event generation, and detector response.

Generation of $D\bar{D}$ pair events in the Mark III Monte Carlo begins with the decay of the $\psi''$ to D mesons with a $\sin^2\theta$ angular distribution. The D mesons may then decay independently either to a specific channel, or to a D 'model'. This model incorporates many of the known D decay channels, but is mainly intended to reproduce observed inclusive distributions, so that the calculation of efficiency in a particular decay channel by use of the Monte Carlo will be properly affected by the decays of the recoil system. The most relevant inclusive distributions are charged multiplicity, pion and kaon momentum spectra, and the semileptonic branching fractions. Two-body pseudoscalar-pseudoscalar (P-P) decays are generated isotropically in the D rest frame. Quasi-two-body pseudoscalar-vector (P-V) decays are generated with the correct $\cos^2\theta$ distribution of the subsequent two-body decay of the vector particle. Cabibbo-allowed semileptonic decays are generated using simple pole form factors[52], such as that of the $F^*$ in $D \to Ke\nu$. However, vector-vector (V-V) decays and other channels with four or more particles in the final state are generated simply according to phase space.

The detector simulation of the Mark III Monte Carlo attempts to reproduce the behavior of each detector subsystem as closely as possible. Monte Carlo data records are produced in exactly the same form as real data. This allows efficiencies, resolutions, and the effect of cuts and corrections to be calculated simply by passing Monte Carlo data through the usual reconstruction and analysis chain.

All particles produced at the initial event vertex decay with their known lifetimes, as do particles from secondary (or tertiary, etc.) vertices. Interactions with matter via multiple Coulomb scattering, ionization energy loss, nuclear interactions, and photon conversions are taken into account according to the amount of material present in the beam pipe and detector sections.

The drift chamber simulation propagates charged particles through the magnetic field, assumed to be uniform. Actual wire positions are used, including wire bowing due to electrostatic forces and gravity. The relation between measured drift time and distance between the wire and the particle trajectory which is used in drift chamber track reconstruction is inverted, and measurement errors appropriate to the wire layer are added. Delta rays which give early drift times are included in a small fraction of the measurements. The layer 2 $dE/dX$ simulation scales energy loss with track path length within the drift cell and with $\beta$ using the Landau-Sternheimer formula, and then varies the energy loss according to the observed pulse height distribution from Bhabha events. Inefficient, dead, and 'noisy' wires are included at a level appropriate to the $\psi''$ running conditions.

The TOF simulation starts with the correct time of entry of a particle into a TOF counter. The number of photons collected by the phototube is assumed to be proportional to the energy deposition of the particle in the TOF, but attenuated according to an exponential in the distance travelled by the photons in the scintillator. Time slewing is included as measured in the data. Charge deposition is represented by a gamma distribution, while the non-Gaussian nature of the observed time residual distribution is approximated by a single Gaussian plus flat tails.

The simulation of photon showers uses a simplified model of shower development. The first step assumes that the total number of shower electrons which pass through the gas sampling volume is given by the initial photon (or electron) energy divided by a constant, in this case, 10 MeV, and distributed

according to a Gaussian with truncated tails. The number of shower electrons in each shower counter layer is calculated by using a standard energy-dependent formula for the distribution of energy loss with depth, and is varied according to a Gaussian. Each shower electron loses energy in the gas according to a very wide Gaussian instead of the true Landau formula, and is distributed transversely in a manner which depends on energy loss and depth within the calorimeter. This shower model is certainly not correct, but has been adjusted so that gross distributions of photon and electron showers from actual Bhabha and $\psi \rightarrow \rho\pi$ events are reproduced by the Monte Carlo, and suffers significantly only for photons with energy below about 0.100 GeV.

## 3. Reconstruction of Cabibbo-Allowed Hadronic Decay Modes

### 3.1 INTRODUCTION

This chapter describes the analysis of exclusive Cabibbo-allowed hadronic D meson decays. The measurement of total integrated luminosity $(9325\,\mathrm{nb}^{-1})$ allows us to quote results in terms of the average $D^+$ or $D^0$ production cross-sections in our data sample times the branching ratios $(\sigma \cdot B)$. Branching ratios themselves are derived by using the cross-sections:

$$\sigma_{D^+} = 4.4 \pm 0.8 \pm 0.5\,\mathrm{nb}$$
$$\sigma_{D^0} = 4.8 \pm 0.9 \pm 0.6\,\mathrm{nb},$$

where the errors are quoted (here and elsewhere) as statistical and systematic, respectively. These cross-sections have been determined by a preliminary analysis which is described briefly in section 3.7. The full and final analysis, which is not yet complete, is expected to obtain cross-sections approximately twice as accurate as those used herein.

### 3.2 PARTICLE IDENTIFICATION AND D RECONSTRUCTION

Before discussing specific decays, it is useful to note some common features of the analyses. In general, reconstruction of exclusive D decay modes requires the identification of charged pions and kaons, neutral kaons, and photons from $\pi^0$ or $\eta$ decay; and determination of their energies and directions.

Except for the decay mode $D^0 \to K^-\pi^+$, identification of charged kaons by TOF is required to suppress the level of background. A particle is classified as a pion, kaon, or proton according to the highest TOF weight of the three if that weight is larger than $4 \times 10^{-6}$ $(5\,\sigma)$. Because pions are the most abundant charged particle, a particle which does not receive a TOF assignment, either because it did not strike a TOF counter or because none of the weights are sufficiently large, is arbitrarily called a pion. After a hypothesis is assigned to

the particle, a correction for energy lost in passing through the beam pipe and detector is applied to recover a better estimate of its initial momentum at the event vertex. The energy lost by minimum-ionizing particles varies with polar angle as $1/(\tan\theta)$, and is typically about $0.002\,\mathrm{GeV}$. Slow kaons and protons in the $1/\beta^2$ energy loss region may lose significantly more.

Neutral kaons are identified in the decay $K^0_s \to \pi^+\pi^-$ by the $\pi^+\pi^-$ invariant mass and by separation of the decay vertex from the event primary vertex. An impact parameter of at least $2\,\mathrm{mm}$ is required for at least one of the pions. Another cut is imposed on the angle $\xi$ between the sum of the pion momenta $\vec{P}_{xy}$ and the vector $\vec{R}_{xy}$ which extends from the primary vertex to the decay vertex in X-Y projection. This cut depends on the length of the vector $\vec{R}_{xy}$ in the following way:

$$|\vec{R}_{xy}| \in \begin{cases} [2,5]\,\mathrm{mm} & \text{cut } \xi < 0.70 \\ [5,10]\,\mathrm{mm} & \text{cut } \xi < 0.50 \\ [10,20]\,\mathrm{mm} & \text{cut } \xi < 0.35 \\ [20,40]\,\mathrm{mm} & \text{cut } \xi < 0.20 \\ [40,\infty]\,\mathrm{mm} & \text{cut } \xi < 0.10 \ . \end{cases}$$

In addition, the two tracks are required to come within $8\,\mathrm{cm}$ in Z of each other at their crossing point in X-Y projection. The vector momentum of each track is then recalculated at the mutual crossing point rather than at the point of closest approach to the primary vertex. The cuts on the resulting $\pi^+\pi^-$ invariant mass distribution shown in Figure 3.1 give a signal-to-background ratio of $2.6 : 1$. These vertex cuts remove a fraction of $K^0_s$ decays which is about 10% for fast $K^0_s$'s $(p \approx 0.800\,\mathrm{GeV/c})$, but varies roughly inversely with kaon momentum.

Charged particles which are consistent with coming from the primary vertex and which do not come from a good $K^0_s$ decay candidate are constrained to the position of the primary vertex, to improve their momentum resolution. All-charged final states from D decay are then reconstructed by forming four-vectors
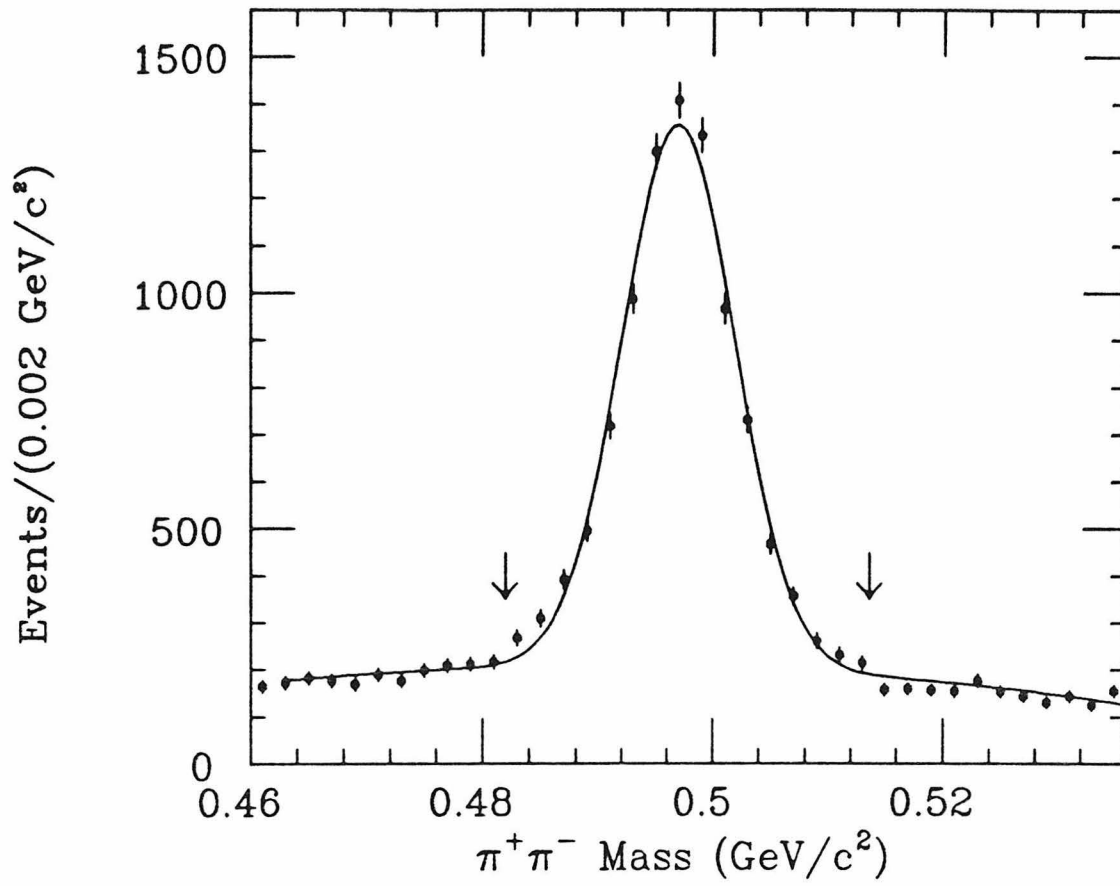
Figure 3.1. Invariant mass of $\pi^+\pi^-$ combinations after vertex displacement cuts. Arrows indicate the mass cuts used to select $K_s^0$ candidates.

of appropriate combinations of kaons and charged pions in each event. For combinations of particles from D decay, the invariant mass:

$$M = \sqrt{(\sum E_i)^2 - |\sum \vec{P}_i|^2}$$

should equal to the D mass. Because the D is produced with energy equal to the known beam energy, the sum $\sum E_i$ can be replaced by $E_{beam}$ in the above formula to obtain what is known as 'beam-constrained' mass:

$$M = \sqrt{(E_{beam})^2 - |\sum \vec{P}_i|^2}$$

which, for fixed beam energy, depends only on the vector sum of momenta. Near the D mass and momentum, these two variables are almost completely uncorrelated: the error in invariant mass is dominated by the $\sum E_i$ term, while the error in beam-constrained mass depends only on the $|\sum \vec{P}_i|$ term. Plotting beam-constrained mass has two nice features: D signals should always appear at the known D mass; and, unlike invariant mass, there is no structure in this variable from feed-down of specific continuum or $D\bar{D}$ final states. The latter point follows from the difficulty of producing particle combinations which have monochromatic momentum as low as $0.270\,\mathrm{GeV/c}$ at a center-of-mass energy of $3.768\,\mathrm{GeV}$, and has been verified 'experimentally' by examining feed-down into various channels from a large number of decay modes in the Monte Carlo.

Decay modes which contain a single $\pi^0$ or $\eta$ are reconstructed in the $\gamma\gamma$ decay mode of the $\pi^0$ or $\eta$. Selection of photons begins with shower counter clusters not associated with any charged tracks. To remove showers associated with interactions of nearby charged hadrons ('split-off's) in the shower counters and $K_L^0$ or neutron interactions, clusters which lie within $18°$ of the entrance of a charged particle into the shower counter are eliminated, as are those which begin in the shower counter after more than three radiation lengths, or which have energy deposited within a single shower counter layer. The $\gamma\gamma$ mass spectrum

after these cuts and with the additional requirement that $E_\gamma > 0.150\,\text{GeV}$, is shown in Figure 3.2. Obviously, the shower counter energy resolution is not sufficient to unambiguously select $\pi^0$ or $\eta$ candidates. To attain better background rejection, as well as to improve the D mass resolution, the energies and positions of the two photons are varied in each particle combination in order to satisfy the two constraints of total energy and $\gamma\gamma$ mass:

$$E_{ch} + E_{\gamma 1} + E_{\gamma 2} = E_{beam}$$
$$2E_{\gamma 1}E_{\gamma 2} \cdot (1 - \cos\theta_{12}) = \begin{cases} M_{\pi^0}^2 \\ M_\eta^2 \end{cases} .$$

An iterative numerical procedure selects the solution to these equations which minimizes $\chi^2$. A cut of $\chi^2 < 6$ then removes combinatorial background. Because the fit constrains the total energy to the beam energy, the beam-constrained mass remains to be plotted and used for the determination of the number of signal events.

The statistical error in the number of events in each mass plot is determined by a maximum likelihood fit, using Poisson statistics on the binned data. The fit function is assumed to be a Gaussian signal term plus a polynomial background, and is integrated over each bin to determine the expected number of events in the bin. The detection efficiency is determined by performing the same analysis on Monte Carlo events. The error on the number of events found in the real data is combined in quadrature with the much smaller error of the Monte Carlo efficiency determination to derive the total statistical error assigned to the number of produced events. Systematic errors from the following sources are considered in these measurements:

- The assumed 5% error on integrated luminosity.
- The efficiency determination when TOF identification of fast kaons is required.
- The efficiency of vertex cuts used to select $K_s^0$ candidates.
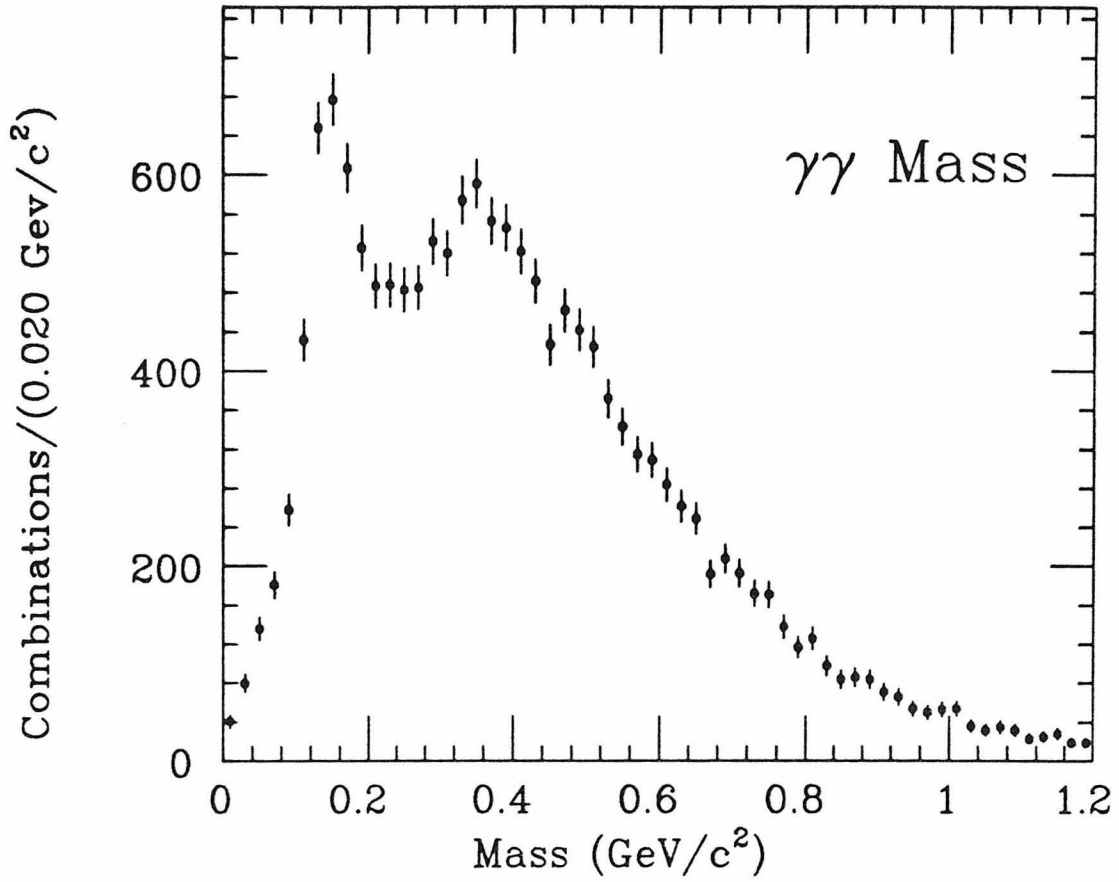
Figure 3.2.   Inclusive $\gamma\gamma$ mass spectrum at the $\psi''$ after $E_\gamma > 0.150\,\text{GeV}$ requirement.

- The tracking efficiency for particles of very low momentum.

- Detection efficiency for low energy ($< 0.1\,\mathrm{GeV}$) photons.

- Modeling of the detector at large $|\cos\theta|$ near the limits of acceptance.

- Tails in $\Delta P_D$, $\Delta E_D$, or $\chi^2$ from the fit used in modes containing $\pi^0$ or $\eta$ which may not be reproduced well by the Monte Carlo.

- Assumption of a polynomial background.

- Use of a fixed signal width as determined by the Monte Carlo in channels where statistics do not allow a reliable determination from the data itself.

- Double-counting in modes with slow $\pi^0$'s, where exchange of one low-energy photon with another may not significantly change the mass. Such a correlation can lead to an apparent signal at the D mass which is larger than the true one.

- Dependence of the efficiency on resonant content in multi-body modes.

To decrease the systematic error due to the Monte Carlo photon simulation, photons are generally required to have fitted energies greater than $0.050\,\mathrm{GeV}$. The higher cut of $0.150\,\mathrm{GeV}$ is used in two-body decay modes containing a fast $\pi^0$. This cut also reduces background from random photon combinations. In addition, in modes where large signals are visible on small backgrounds, fiducial cuts near the limits of detector acceptance may be applied: $|\cos\theta| < 0.75$ for kaons identified by TOF, $|\cos\theta| < 0.85$ for other charged particles, and $|\cos\theta| < 0.95$ for photons, where $\theta$ is the angle between the particle momentum vector and the beam axis. The following sections describe the measurements of specific decays.

## 3.3 Two-Body Decays

The $K^-\pi^+$ decay mode is treated separately because TOF identification is handled in a unique manner. In this decay, both particles are produced in the momentum range $p \in [0.720, 1.020]\,\mathrm{GeV/c}$ where TOF separation of kaons and pions begins to suffer. Use of TOF in this momentum range not only reduces

efficiency, but makes the measurement more dependent on the quality of the TOF simulation in the Monte Carlo.

The approach taken is to examine all pairs of oppositely-charged particles within a fiducial region of $|\cos\theta| < 0.80$. When neither particle has a solid TOF kaon or pion hypothesis, or if both do, but the hypothesis is the same, then one particle is arbitrarily assigned to be a pion, and the other to be a kaon. If just one particle has a kaon or pion hypothesis, or if one has a kaon and the other a pion hypothesis, that information is used to decide the particle assignment. We require the measured $K^-\pi^+$ energy to be within $\pm 0.100\,\text{GeV}$ of the known beam energy, while the difference in energy between the correct and the wrong choice of kaon and pion has a flat distribution within limits $\pm 0.040\,\text{GeV}$ because of the similar kaon and pion momenta. Thus, TOF information is only used to slightly narrow the total energy distribution of real $D^0 \to K^-\pi^+$ decays. The resulting beam-constrained mass plot show in Figure 3.3 contains $(1298 \pm 44)$ signal events, determined by a fit to a Gaussian plus a quadratic background. From a detection efficiency of $(58.8 \pm 0.9)\%$, we derive the production cross-section:

$$\sigma_{D^0} \cdot B(D^0 \to K^-\pi^+) = 0.237 \pm 0.009 \pm 0.013\,\text{nb}\,.$$

Nearly all of the systematic error in this measurement comes from the measurement of total integrated luminosity (5%), while small contributions arise from tracking efficiency (2%) and tails in the beam-constrained mass plot (2%). This value is also in excellent agreement with the result obtained by demanding positive TOF kaon identification within $|\cos\theta| < 0.75$.

The analysis of the decay $D^+ \to \bar{K}^0\pi^+$ is quite simple. Standard fiducial cuts ($|\cos\theta| < 0.75$ for kaons, $|\cos\theta| < 0.85$ for other charged particles, and $|\cos\theta| < 0.95$ for photons) and $K_s^0$ vertex cuts are applied. After requiring the invariant mass of each $\bar{K}^0\pi^+$ combination to lie within $0.060\,\text{GeV}/c^2$ of the $D^+$ mass, the beam-constrained mass plot shown in Figure 3.3 results. The $(147 \pm 14)$ signal events, combined with a detection efficiency of 0.125 determined by the
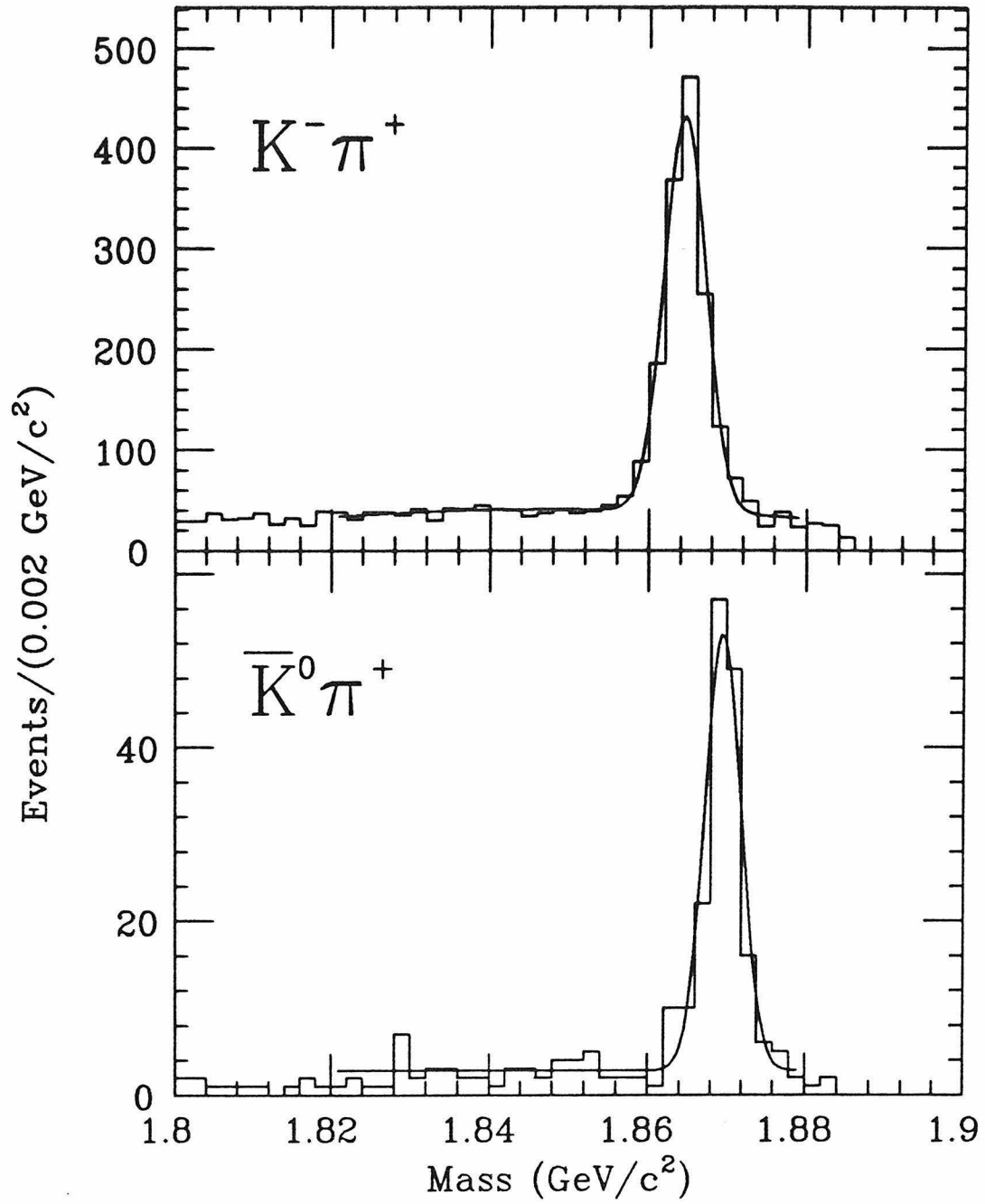
Figure 3.3. Beam-constrained mass plots for $K^-\pi^+$ and $\bar{K}^0\pi^+$.

Monte Carlo, yield the measurement:

$$\sigma_{D^+} \cdot B(D^+ \to \bar{K}^0 \pi^+) = 0.126 \pm 0.012 \pm 0.009 \, \text{nb} \, .$$

The systematic error in this measurement comes from $K_s^0$ vertex cuts (3%), tails in the beam-constrained mass plot (4%), and total integrated luminosity (5%).

The analysis of the $D^0$ decay to $\bar{K}^0 \pi^0$ is very similar to that for the $\bar{K}^0 \eta$ decay. Because the photons are relatively hard, a cut of $E_\gamma > 0.150 \, \text{GeV}$ on the fitted photon energies is imposed to reduce background from random photons and soft $\pi^0$'s, although it also removes $1/3$ of the signals. Standard fiducial and $K_s^0$ vertex cuts are applied. The mass plots which result from the two-constraint fits to the beam energy and the $\pi^0$ or $\eta$ mass are shown in Figure 3.4. The background in each case is assumed to be quadratic. Because of the large number of signal events and small amount of background in the $\bar{K}^0 \pi^0$ mass plot, the mean and width of the signal term are allowed to vary in the fit, yielding $(70 \pm 12)$ signal events. Photons from the decay of the $\pi^0$ in $\bar{K}^0 \pi^0$ usually emerge with a small opening angle. Because of the larger mass of the $\eta$, the photons emerge with a larger opening angle in the $\bar{K}^0 \eta$ decay, allowing more background from random photon combinations. Final states containing an $\eta$ are also more difficult to observe because of the $\eta \to \gamma\gamma$ branching ratio of 39%. Thus, the $\bar{K}^0 \eta$ mass plot is fitted using a fixed signal width ($\sigma = 0.0035 \, \text{GeV}/c^2$) as observed in the Monte Carlo simulation to obtain a signal of $(28 \pm 12)$ events. Detection efficiencies of 0.070 for $\bar{K}^0 \pi^0$ and 0.034 for $\bar{K}^0 \eta$ lead to the measurements:

$$\sigma_{D^0} \cdot B(D^0 \to \bar{K}^0 \pi^0) = 0.108 \pm 0.020 \pm 0.010 \, \text{nb}$$

$$\sigma_{D^0} \cdot B(D^0 \to \bar{K}^0 \eta) = 0.088 \pm 0.039 \pm 0.012 \, \text{nb} \, .$$

The systematic error in the measurement of $\bar{K}^0 \pi^0$ comes from $K_s^0$ vertex cuts (3%), possible tails in the $\chi^2$ distribution (5%), photon detection efficiency (5%), and total integrated luminosity (5%). The systematic error in the $\bar{K}^0 \eta$

measurement contains an additional contribution due to the fixed signal width (10%).

## 3.4 THREE-BODY DECAYS

This section describes the analysis* of Cabibbo-allowed three-body decays of the $D^+$ to $K^-\pi^+\pi^+$ and $\bar{K}^0\pi^+\pi^0$, and of the $D^0$ to $K^-\pi^+\pi^0$ and $\bar{K}^0\pi^+\pi^-$. These final states may include significant contributions from two-body pseudoscalar-vector D decays: $\bar{K}^{*0}\pi^+$ in the $K^-\pi^+\pi^+$ final state; $\bar{K}^{*0}\pi^+$ and $\bar{K}^0\rho^+$ in the $\bar{K}^0\pi^+\pi^0$ final state; $\bar{K}^{*0}\pi^0$, $K^{*-}\pi^+$, and $K^-\rho^+$ in the $K^-\pi^+\pi^0$ final state; $K^{*-}\pi^+$ and $\bar{K}^0\rho^0$ in the $\bar{K}^0\pi^+\pi^-$ final state. Contributions from $\bar{K}^*(1430)\pi$ or even $\kappa(1350)\pi$ must be allowed, in principle, but the large resonance widths and limited phase space for these decays make it doubtful that their fractions could be reliably determined from the Dalitz plots, if they could be recognized at all. Because D mesons are pseudoscalar particles and hence decay isotropically, all information about these decays is contained within their Dalitz plots. Preliminary results are available from an analysis, still in progress at this time, which determines the relative resonant and non-resonant fractions of the Dalitz plots in each of these modes following the procedure outlined in Reference 53. Signals for the three-body $K\pi\pi$ decays are obtained by applying standard fiducial and $K_s^0$ vertex cuts. Events within the signal region are kinematically fitted using the constraint of the D mass, to ensure that they lie within the Dalitz plot boundary. A maximum likelihood fit is then applied to the unbinned distribution of events within the Dalitz plot. The extreme edges of the plot, where at least one particle is very slow and the detection efficiency is dropping off sharply, are cut away. Detection efficiency is then found as a function of position on the Dalitz plot using the Monte Carlo. To minimize the effect of statistical fluctuations, this efficiency is smoothed over the Dalitz

---

* Work done in collaboration with A. Duncan, Univ. of Washington (preliminary).
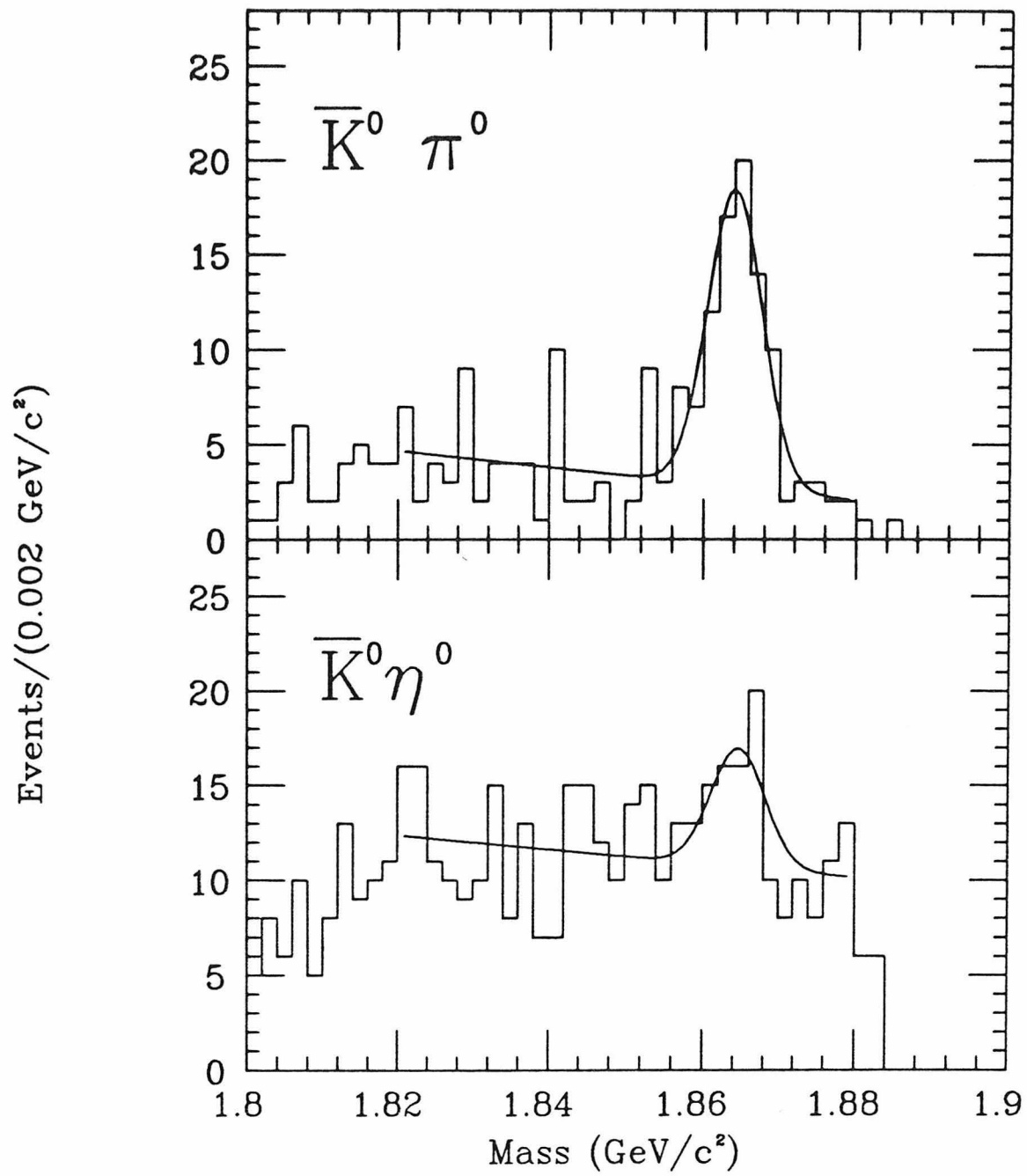
Figure 3.4. Beam-constrained mass plots for $\bar{K}^0\pi^0$ and $\bar{K}^0\eta$.

plot. The fit function is a convolution of detection efficiency with a coherent sum of non-resonant phase space and relativistic Breit-Wigner amplitudes taken to represent $\rho$ and $K^*$ contributions. The resonant contributions to the $K\pi\pi$ final states are $K^*(892)\pi$ or $K\rho$ pseudoscalar-vector decays, in which the vector particle is produced with helicity 0 only. Subsequent two-body decays ($K^* \to K\pi$ or $\rho \to \pi\pi$) occur with a $\cos^2\theta$ distribution in the vector rest frame with respect to the direction of the vector particle in the D rest frame. Instead of smooth bands across the Dalitz plot, then, resonant decays tend to peak near Dalitz plot boundaries. The distribution of background events within the Dalitz plot is found to be fairly uniform (except for moderate $K^*$ contributions), and is represented by 'control' events having beam-constrained mass below the D signal region. The numbers of background events in control and signal regions are determined by a fit to the beam-constrained mass plot, but varied in the determination of systematic error.

The beam-constrained mass plot for the $K^-\pi^+\pi^+$ final state is shown in Figure 3.5, along with a fit yielding $(1166 \pm 41)$ signal events. The Dalitz plot for this decay is shown in Figure 3.6 with one of the $K^-\pi^+$ mass projections. A modest, but statistically significant contribution from $\bar{K}^{*0}\pi^+$ is observed. However, the majority of the Dalitz plot, away from the $\bar{K}^{*0}$ region, shows structure which is clearly inconsistent with a flat non-resonant contribution or variations in detection efficiency. Because of Bose symmetry, the two identical pions in the final state must have even angular momentum $L$. By allowing an $L = 2$ contribution with a $\beta^2$ dependence for the $\pi^+\pi^+$ system, a much better, but still inconsistent result is obtained. Such an $L = 2$ term varies as $\cos^4\theta$ near the boundaries, producing a steep rise near the edges of the Dalitz plot which is not observed. In determining the production rate for $K^-\pi^+\pi^+$, the effect of our changing detection efficiency across the Dalitz plot must be taken into account. This is accomplished by dividing the Dalitz plot into sections of equal $M^2_{K^-\pi^+}$, and determining the detection efficiency within each section, as shown in

Figure 3.7. Sections near the boundary which have small area and, consequently, poorly determined efficiencies, are left out at this stage. The overall efficiency within the included sections is 5% higher than if the decay were assumed to proceed via phase space. The small, ignored sections are then incorporated by using this 5% correction to scale the efficiency over the entire Dalitz plot from the value found from phase space production. The most noticeable efficiency variation is a decrease at low $K^-\pi_1^+$ and $K^-\pi_2^+$ masses, where the kaon is slow and tends to decay. Note that, although the decay matrix element must be symmetric between the identical pions, the drift chamber reconstruction program tends to find trajectories of high momentum pions before those of very low momentum, leading to a slight asymmetry in detection efficiency between the lower right and upper left corners of the Dalitz plot. Using the derived overall efficiency, we find:

$$\sigma_{D^+} \cdot B(D^+ \to K^-\pi^+\pi^+) = 0.399 \pm 0.017 \pm 0.028 \, \text{nb}.$$

Included in the systematic error is a small contribution (2%) for the efficiency determination within the small boundary sections of the Dalitz plot and variations within individual sections, as well as contributions from tracking efficiency (5%), non-Gaussian tails in the beam-constrained mass plot (2%), and total integrated luminosity (5%).

The beam-constrained mass plot for the $\bar{K}^0\pi^+\pi^0$ final state shown in Figure 3.5 contains $(239 \pm 45)$ signal events. The Dalitz plot for this decay is shown in Figure 3.8, along with the three possible mass projections and the overplotted projections of the best fit to the Dalitz plot. Preliminary results describe this Dalitz plot as consisting of $(87 \pm 9 \pm 5)\%$ $\bar{K}^0\rho^+$, $(7 \pm 4 \pm 4)\%$ $\bar{K}^{*0}\pi^+$, and $(6 \pm 6 \pm 4)\%$ flat phase space. The detection efficiencies for these contributions (correcting for the $\bar{K}^{*0} \to \bar{K}^0\pi^0$ branching ratio of 33.3%) are determined by Monte Carlo as 3.6%, 2.9%, and 4.2%, respectively. Using these fractions to
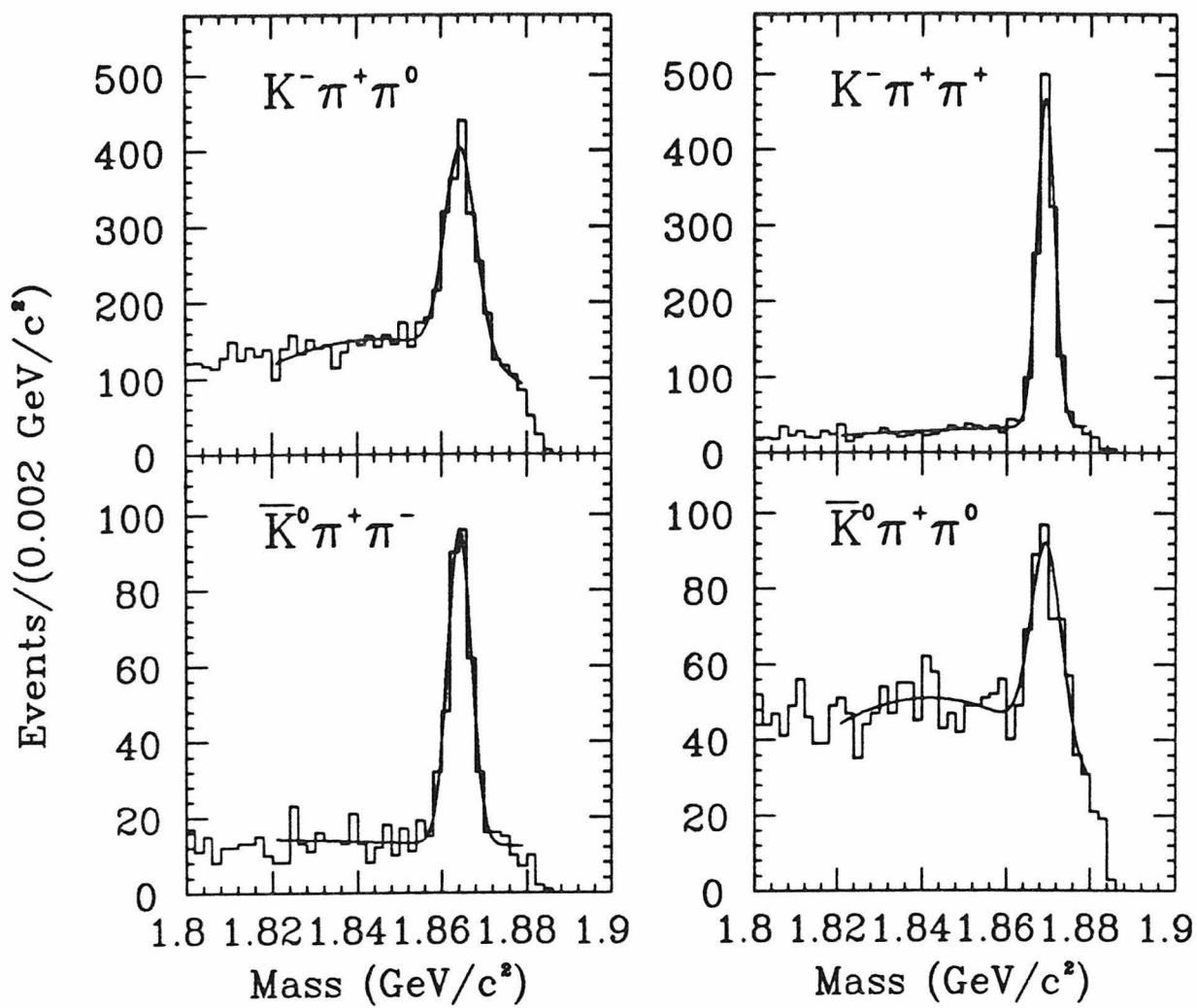
Figure 3.5. Beam-constrained mass plots for $K\pi\pi$ decay modes.

K⁻π⁺π⁺ Dalitz Plot

K⁻π⁺₁ Projection

K⁻π⁺₂ Projection
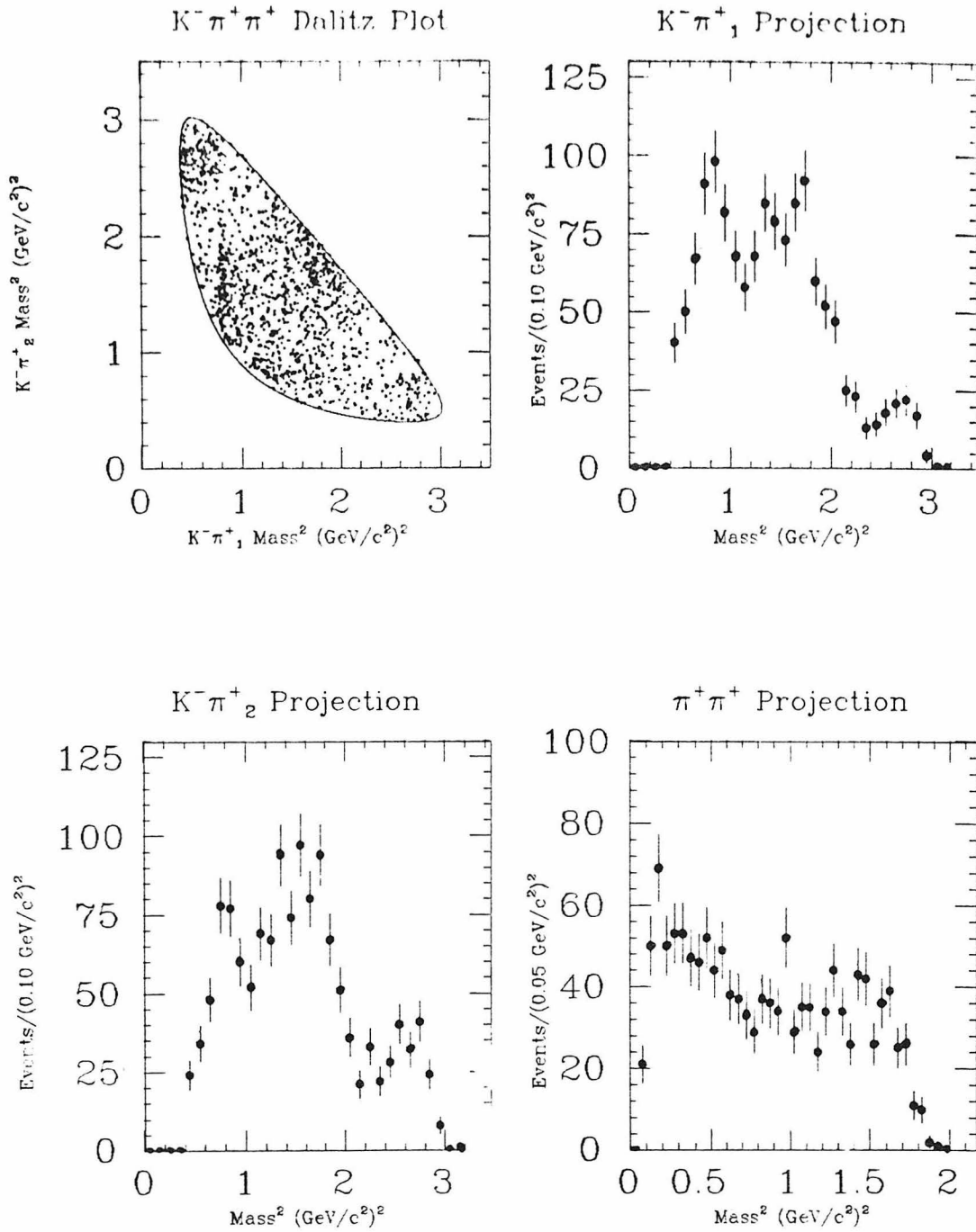
π⁺π⁺ Projection

Figure 3.6. Dalitz plot for $D^+ \rightarrow K^-\pi^+\pi^+$ and the mass projections.
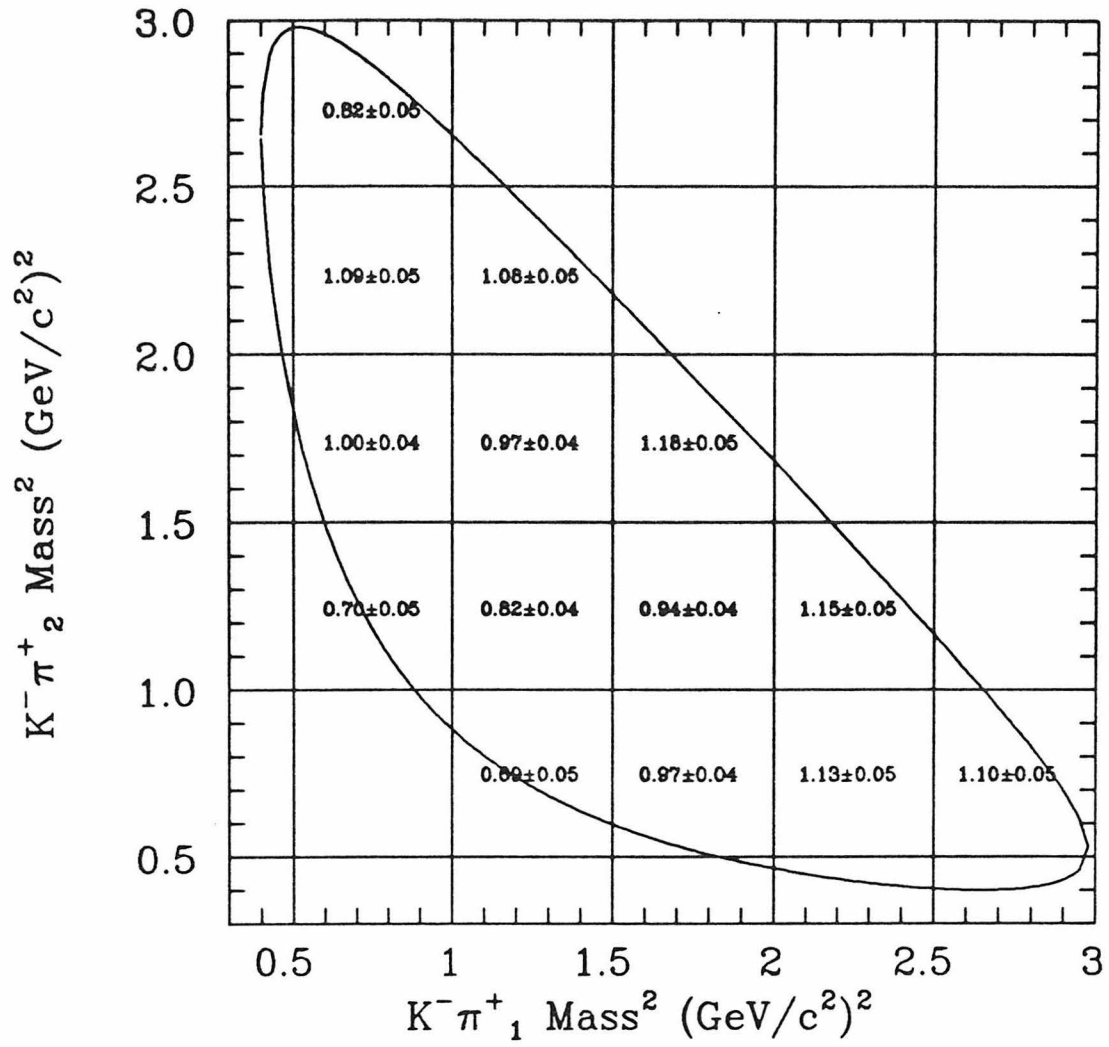
Figure 3.7. Variation of $K^-\pi^+\pi^+$ reconstruction efficiency across the Dalitz plot.

obtain the average efficiency from the Monte Carlo, we derive:

$$\sigma_{D^+} \cdot B(D^+ \to \bar{K}^0 \pi^+ \pi^0) = 0.714 \pm 0.142 \pm 0.100 \, \text{nb}.$$

The portion of the systematic error which is due to the structure of the Dalitz plot (4%) is estimated by varying 10% of the decay from the channel with the highest efficiency (flat phase space) to the channel with the lowest efficiency $(\bar{K}^{*0} \pi^+)$. Other contributions to the systematic error are from the photon detection efficiency (10%), tails in the $\chi^2$ distribution of the two-constraint fit to photon energies and directions (5%), $K^0_s$ vertex cuts (5%), and total integrated luminosity (5%).

The beam-constrained mass plot for the $K^- \pi^+ \pi^0$ final state is shown in Figure 3.5 with a fit which includes $(1250 \pm 68)$ signal events. The Dalitz plot for this decay is shown in Figure 3.9, along with the three possible mass projections and the overplotted projections of the best fit to the Dalitz plot. Preliminary results describe the $K^- \pi^+ \pi^0$ Dalitz plot as consisting of $(74 \pm 5 \pm 5)\%$ $K^- \rho^+$, $(13 \pm 3 \pm 2)\%$ $K^{*-} \pi^+$, $(8 \pm 3 \pm 2)\%$ $\bar{K}^{*0} \pi^0$, and $(5 \pm 4 \pm 3)\%$ flat phase space. The detection efficiencies for these contributions (correcting for the $K^{*-} \to K^- \pi^0$ and $\bar{K}^{*0} \to K^- \pi^+$ branching ratios of 33.3% and 66.7%, respectively) are determined by Monte Carlo as 14%, 10%, 16%, and 16%, respectively. Using these fractions to obtain the average efficiency from the Monte Carlo, we derive:

$$\sigma_{D^0} \cdot B(D^0 \to K^- \pi^+ \pi^0) = 0.978 \pm 0.065 \pm 0.137 \, \text{nb}.$$

In this case, only a 3% systematic error results from variation of 5% of the decay fractions between the channels having lowest and highest detection efficiency, $\bar{K}^{*0} \pi^0$ and $K^{*-} \pi^+$, respectively. Other contributions to the total systematic error come from the photon detection efficiency (10%), tails in the $\chi^2$ distribution from the fit to photon energies and directions (5%), tracking efficiency (5%), and total integrated luminosity (5%).
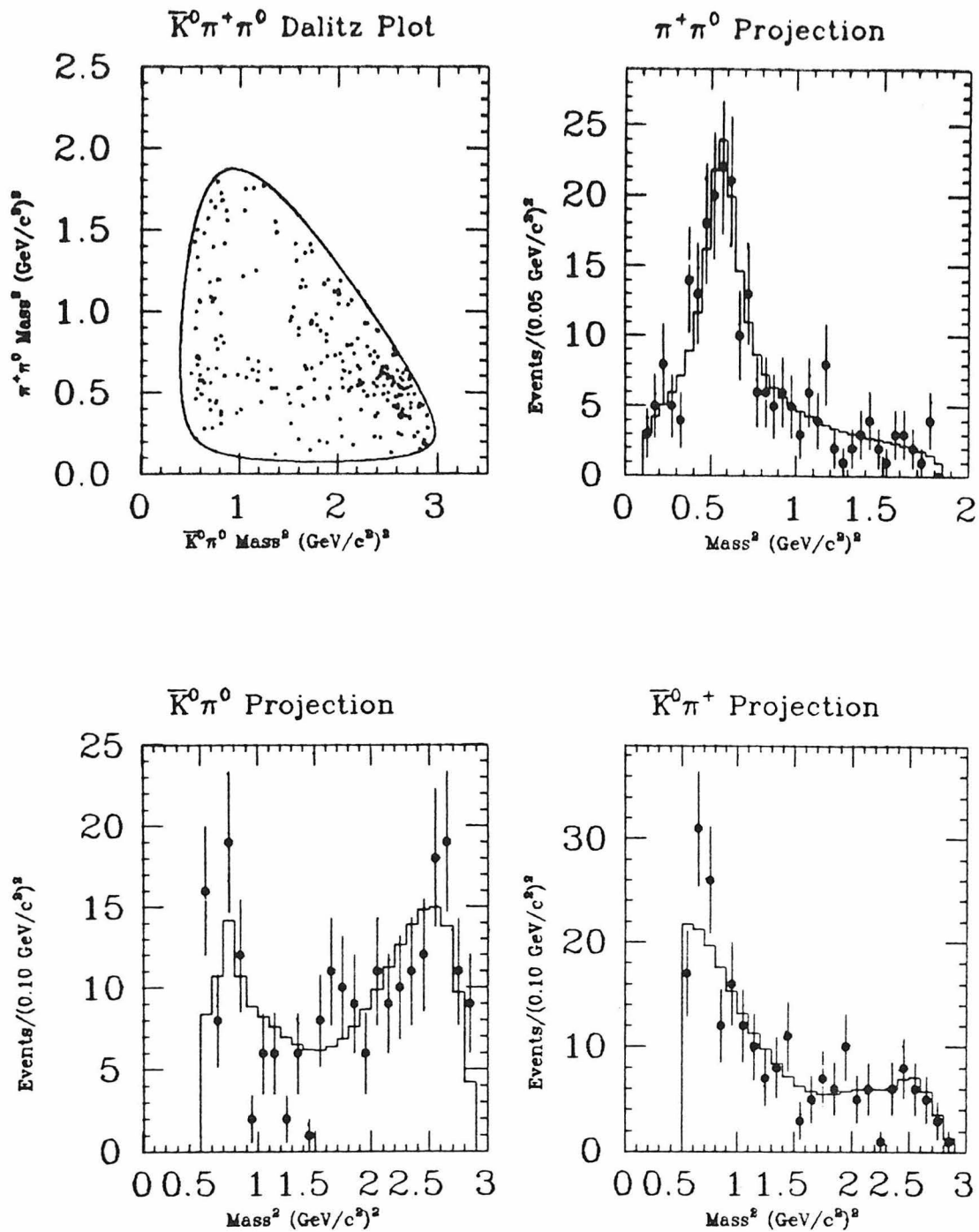
Figure 3.8. Dalitz plot for $D^+ \rightarrow \bar{K}^0 \pi^+ \pi^0$ and the three possible mass projections.
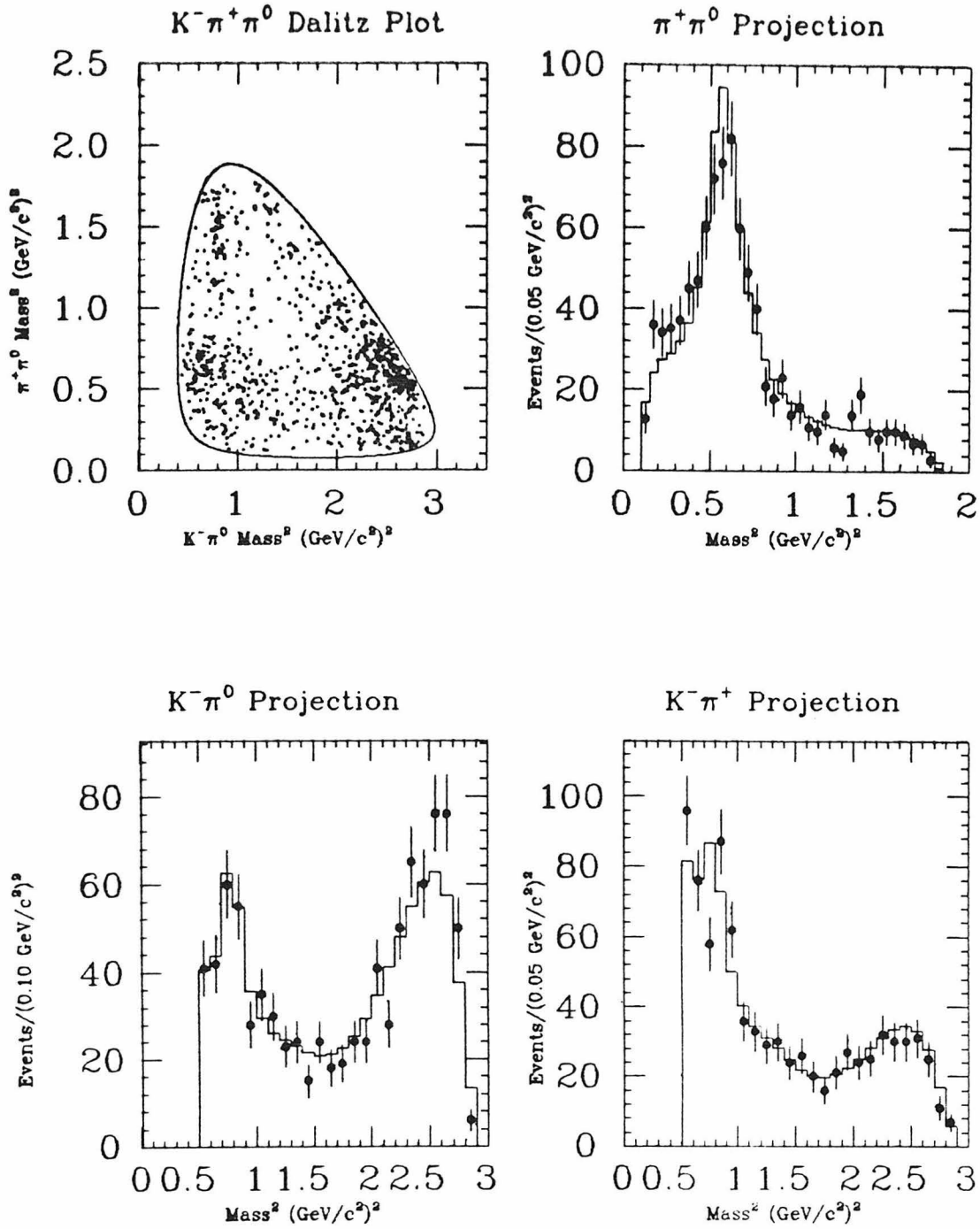
Figure 3.9. Dalitz plot for $D^0 \rightarrow K^-\pi^+\pi^0$ and the three possible mass projections.

The beam-constrained mass plot for the $\bar{K}^0\pi^+\pi^-$ final state is shown in Figure 3.5 with a fit which includes $(291 \pm 22)$ signal events. The Dalitz plot for this decay is shown in Figure 3.10, along with the three possible mass projections and the overplotted projections of the best fit to the Dalitz plot. The contributions to the $\bar{K}^0\pi^+\pi^-$ decay are given by this (preliminary) fit as $(17\pm5\pm3)\%$ $\bar{K}^0\rho^0$, $(64\pm8\pm5)\%$ $K^{*-}\pi^+$, and $(19\pm9\pm4)\%$ flat phase space. The detection efficiencies for these contributions (correcting for the $K^{*-} \rightarrow \bar{K}^0\pi^-$ branching ratio of 66.7%) are determined by Monte Carlo as 8.8%, 8.1%, and 8.7%, respectively. Using these fractions to obtain the average efficiency from the Monte Carlo, we derive:

$$\sigma_{D^0} \cdot B(D^0 \rightarrow \bar{K}^0\pi^+\pi^-) = 0.372 \pm 0.030 \pm 0.031 \text{ nb}.$$

Here, the systematic error from variation of the decay fractions is very small (1%). Other systematic errors in this measurement come from $K^0_s$ vertex cuts (5%), tracking efficiency (4%), and total integrated luminosity (5%).

## 3.5 DECAYS TO FINAL STATES OF FOUR OR MORE PARTICLES

Phase space for D decays to final states of high multiplicity is quite limited, making separation of the various resonant contributions difficult. Efficiencies are therefore calculated from Monte Carlo events produced according to phase space only. No attempt is made to include possible variations in efficiency due to the (unknown) resonant content of these decays in the calculation, either explicitly, or as a contribution to systematic error. Standard fiducial cuts are imposed for the decay modes $K^-\pi^+\pi^-\pi^+$ and $\bar{K}^0\pi^+\pi^-\pi^+$, but not for the smaller $K^-\pi^+\pi^+\pi^0$ and $\bar{K}^0\pi^+\pi^-\pi^0$ decays. To decrease the amount of double-counting in the $K^-\pi^+\pi^+\pi^0$ and $\bar{K}^0\pi^+\pi^-\pi^0$ mass plots due to interchange of low-energy photons, somewhat restrictive cuts are applied: $E_\gamma > 0.75\,\text{GeV}$ for the fitted photon energies, and $\chi^2 < 3$ from the two-constraint fit to photon energies and directions.
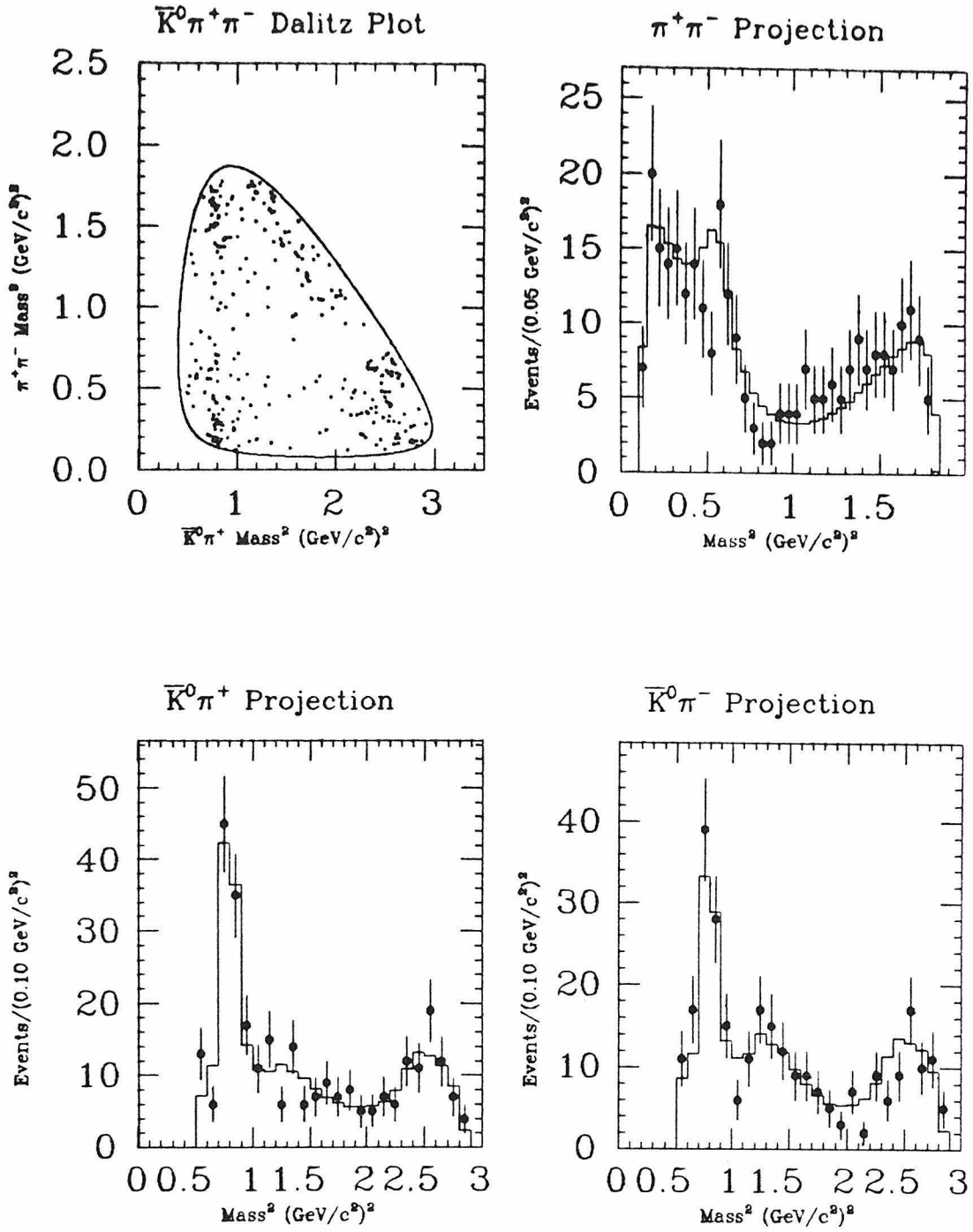
Figure 3.10. Dalitz plot for $D^0 \rightarrow \bar{K}^0\pi^+\pi^-$ and the three possible mass projections.

Signals for the $D^0$ decay modes $K^-\pi^+\pi^-\pi^+$ and $\bar{K}^0\pi^+\pi^-\pi^0$ are shown in Figure 3.11. The numbers of signal events in these mass plots are determined as $(1103 \pm 44)$ and $(169 \pm 26)$ for $K^-\pi^+\pi^-\pi^+$ and $\bar{K}^0\pi^+\pi^-\pi^0$, respectively. The signal width ($\sigma = 0.0034\,\text{GeV}/c^2$) predicted by the Monte Carlo is used in the latter measurement. From detection efficiencies of 0.209 for $K^-\pi^+\pi^-\pi^+$ and 0.027 for $\bar{K}^0\pi^+\pi^-\pi^0$, we determine:

$$\sigma_{D^0} \cdot B(D^0 \to K^-\pi^+\pi^-\pi^+) = 0.566 \pm 0.027 \pm 0.061\,\text{nb}$$

$$\sigma_{D^0} \cdot B(D^0 \to \bar{K}^0\pi^+\pi^-\pi^0) = 0.666 \pm 0.113 \pm 0.153\,\text{nb}.$$

Systematic errors are assigned to the $K^-\pi^+\pi^-\pi^+$ measurement from tracking efficiency (8%), total integrated luminosity (5%), and non-Gaussian tails in the beam-constrained mass plot(5%). The $\bar{K}^0\pi^+\pi^-\pi^0$ systematic error includes contributions from total integrated luminosity (5%), $K^0_s$ vertex cuts (10%), use of a fixed signal width (10%), tracking efficiency (5%), the absence of fiducial cuts (5%), possible tails in the $\chi^2$ distribution (10%), photon detection efficiency (7%), and possible double-counting of signal events (10%).

Within the $\bar{K}^0\pi^+\pi^-\pi^0$ final state is a contribution from the $D^0 \to \bar{K}^0\omega$ decay, where $\omega$ decays to $\pi^+\pi^-\pi^0$. Our experimental resolution in $\pi^+\pi^-\pi^0$ mass on the $\omega$ signal is determined by Monte Carlo as $0.015\,\text{GeV}/c^2$, a value which is significantly larger than the $\omega$ width of $\Gamma = 0.010\,\text{GeV}/c^2$. The signal for this decay shown in Figure 3.12(a) is obtained by requiring the $\pi^+\pi^-\pi^0$ mass to lie between 0.753 and $0.813\,\text{GeV}/c^2$, representing $\pm 2\sigma$ around the $\omega$ mass, and contains $(32.4 \pm 7.1)$ signal events, using a fixed signal width of $\sigma = 0.0034\,\text{GeV}/c^2$. The number of $\bar{K}^0\pi^+\pi^-\pi^0$ events which are not associated with the $\omega$ in this mass plot is estimated by fitting the mass plot which contains events having $\pi^+\pi^-\pi^0$ mass between $2\sigma - 4\sigma$ from the $\omega$ mass shown in Figure 3.12(b). This fit yields $(8.7 \pm 4.9)$ signal events. Subtracting the two results gives $(23.7 \pm 8.6)$ events. Applying the same subtraction to Monte Carlo $\bar{K}^0\omega$ events to account for events between $2\sigma - 4\sigma$ which come from the tail of
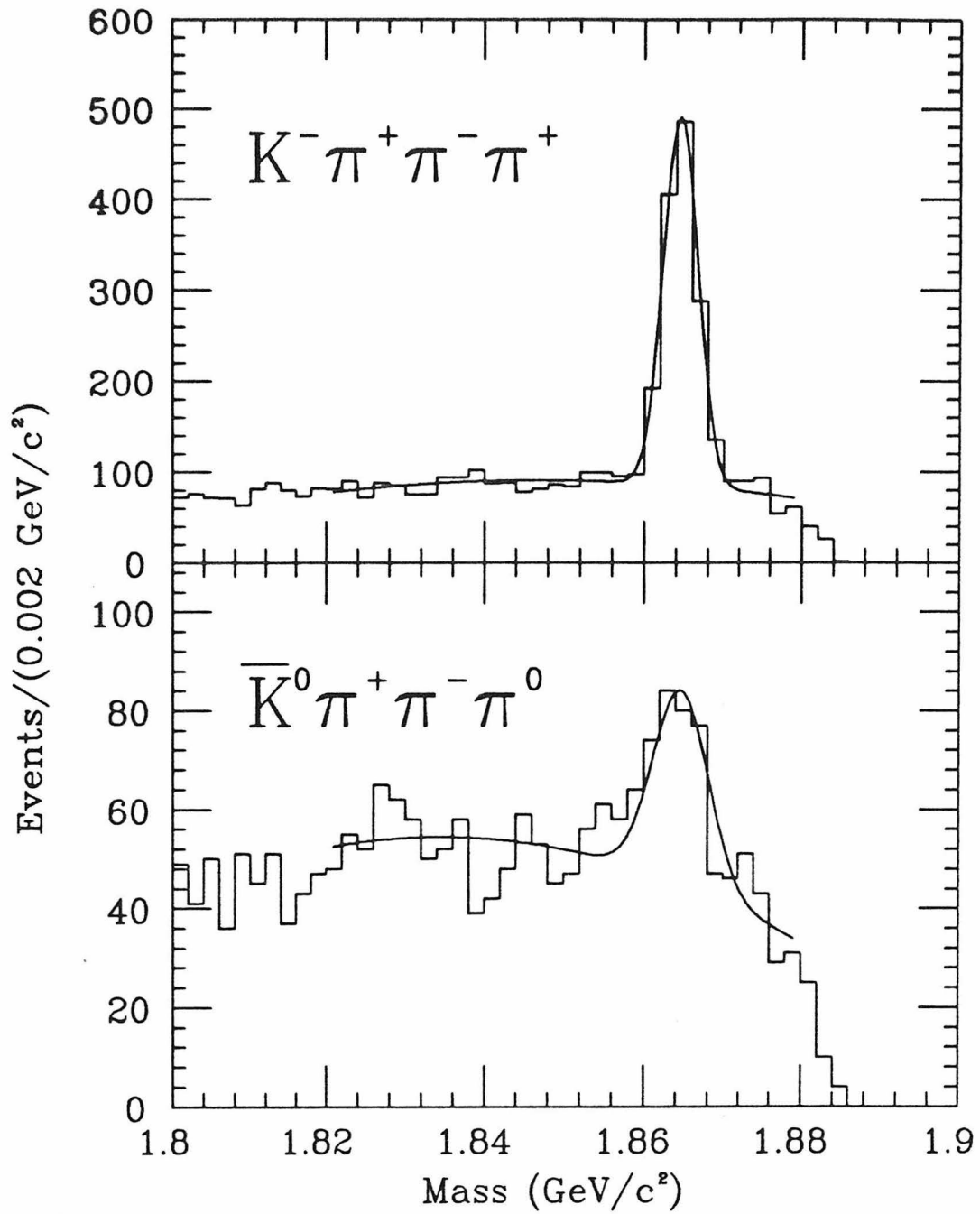
Figure 3.11. Beam-constrained mass plots for $K^-\pi^+\pi^-\pi^+$ and $\bar{K}^0\pi^+\pi^-\pi^0$.

the $\omega$ signal ($\sim 10\%$) results in a detection efficiency of $1.36\%$, from which we derive:

$$\sigma_{D^0} \cdot B(D^0 \to \bar{K}^0 \omega) = 0.187 \pm 0.073 \pm 0.047 \, \text{nb}.$$

This measurement includes a large number of possible systematic errors: total integrated luminosity ($5\%$), $K_s^0$ vertex cuts ($10\%$), use of a fixed signal width ($10\%$), tracking efficiency ($5\%$), the absence of fiducial cuts ($5\%$), tails in $\chi^2$ from the two-constraint fit to photon energies and directions ($5\%$), photon detection efficiency ($7\%$), double counting of events due to interchange of low energy photons ($10\%$), and an additional contribution ($10\%$) due to modeling the $\omega \to \pi^+ \pi^- \pi^0$ decay by flat phase space in the Monte Carlo. The assumption of a phase space decay for the $\omega$ ignores the Dalitz plot structure of the $\omega \to \pi^+ \pi^- \pi^0$ decay, as well as the expected $\sin^2 \theta$ angular distribution of the vector normal to the plane of the $\pi^+ \pi^- \pi^0$ system in the $\omega$ rest frame relative to the $\omega$ direction in the $D^0$ rest frame. This non-uniform angular distribution results because $D^0 \to \bar{K}^0 \omega$ is a pseudoscalar-vector decay of a pseudoscalar particle, so that the $\omega$ can be produced with helicity 0 only, and cannot decay to three pions which are oriented in a plane perpendicular to the $\omega$ direction of motion (as seen in the $D^0$ rest frame).

Signals for the $D^+$ decay modes $\bar{K}^0 \pi^+ \pi^- \pi^+$ and $K^- \pi^+ \pi^+ \pi^0$ are shown in Figure 3.13. The numbers of signal events in these mass plots are determined as $(236 \pm 22)$ and $(197 \pm 28)$ for $\bar{K}^0 \pi^+ \pi^- \pi^+$ and $K^- \pi^+ \pi^+ \pi^0$, respectively, using the signal width ($\sigma = 0.0027 \, \text{GeV}/c^2$) predicted by the Monte Carlo in the latter measurement. From detection efficiencies of 0.083 for $\bar{K}^0 \pi^+ \pi^- \pi^+$ and 0.081 for $K^- \pi^+ \pi^+ \pi^0$, we determine:

$$\sigma_{D^+} \cdot B(D^+ \to \bar{K}^0 \pi^+ \pi^- \pi^+) = 0.305 \pm 0.031 \pm 0.030 \, \text{nb}$$

$$\sigma_{D^+} \cdot B(D^+ \to K^- \pi^+ \pi^+ \pi^0) = 0.260 \pm 0.040 \pm 0.054 \, \text{nb}.$$

Contributions to systematic error in the $\bar{K}^0 \pi^+ \pi^- \pi^+$ decay come from $K_s^0$ vertex cuts ($8\%$), tracking efficiency ($5\%$), and total integrated luminosity ($5\%$).
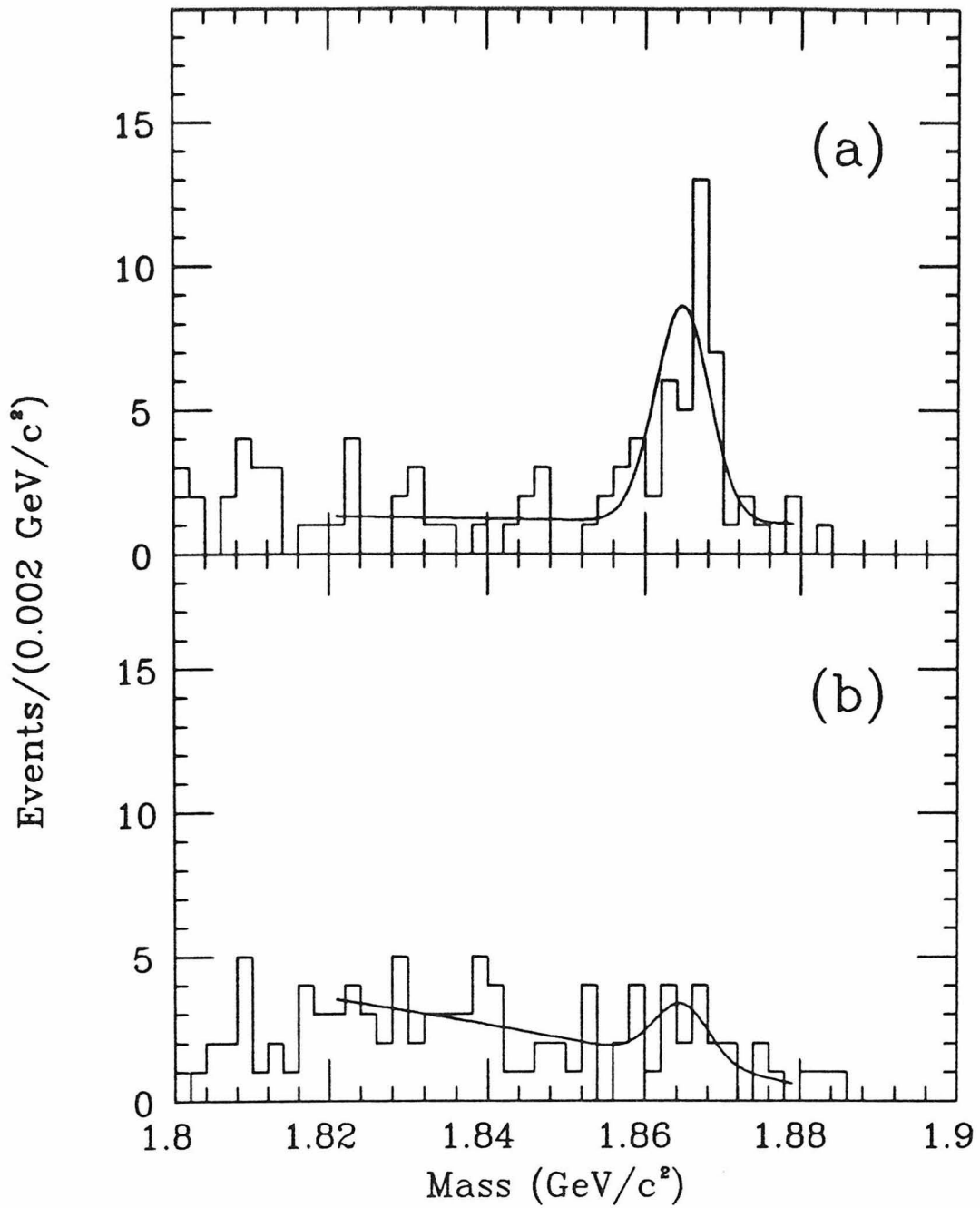
Figure 3.12. Beam-constrained mass plot for $\bar{K}^0\pi^+\pi^-\pi^0$ after cuts (a) to isolate the $\bar{K}^0\omega$ substructure, and (b) to measure feed-down from other $\bar{K}^0\pi^+\pi^-\pi^0$ decays.

Contributions to systematic error in the $K^-\pi^+\pi^+\pi^0$ decay come from possible double-counting (10%), photon detection efficiency (7%), use of a fixed signal width (10%), tracking efficiency (5%), tails in the $\chi^2$ distribution of the two-constraint fit to photon energies and directions (10%), the absence of fiducial cuts (5%), and total integrated luminosity (5%).

## 3.6 THE FINAL STATE $\bar{K}^0 K^+ K^-$

Of the Cabibbo-allowed decays which can arise only through W-exchange diagrams, the decay $D^0 \to \bar{K}^0\phi$, observable in the final state $\bar{K}^0 K^+ K^-$, is the most experimentally accessible. Because all particles in this decay are rather slow, the kaons are likely to decay in flight before they can be identified by TOF measurement. Also, their momenta often lie within the range where dE/dX can effectively separate pions and kaons. Therefore, we use dE/dX measurement in this decay to assign a particle hypothesis to those particles which are not identified by TOF measurement. The requirements for such an assignment are that the measured energy loss deviates from that expected for the best particle hypothesis by no more than $-2\sigma$ or $+3\sigma$ (asymmetric because of Landau fluctuations), and deviates from that expected for the next best particle hypothesis by at least $2\sigma$ more than the best. No fiducial cuts are imposed on charged tracks, but $K^0_s$ vertex cuts are retained. The resulting beam-constrained mass plot shown in Figure 3.14 contains $(22\pm5)$ signal $\bar{K}^0 K^+ K^-$ events. The 24 events in this plot with mass between 1.858 and 1.872 GeV/c$^2$ are used to form the Dalitz plot shown in Figure 3.15(a). There is a significant accumulation of events at low $K^+K^-$ mass. In this respect, it is interesting to note that a $\pi^-p$ fixed-target experiment[54] has reported (in 1981) a signal in the $\bar{K}^0 K^+ K^-$ final state containing 10 events above a background of 1.4 events. This signal was derived by requiring the $K^+K^-$ mass to lie between 1.01 and 1.03 GeV/c$^2$ in an attempt to isolate the $\bar{K}^0\phi$ decay. The Dalitz plot of events in our sample is not, however, consistent with the Dalitz plot, shown in Figure 3.15(b), observed
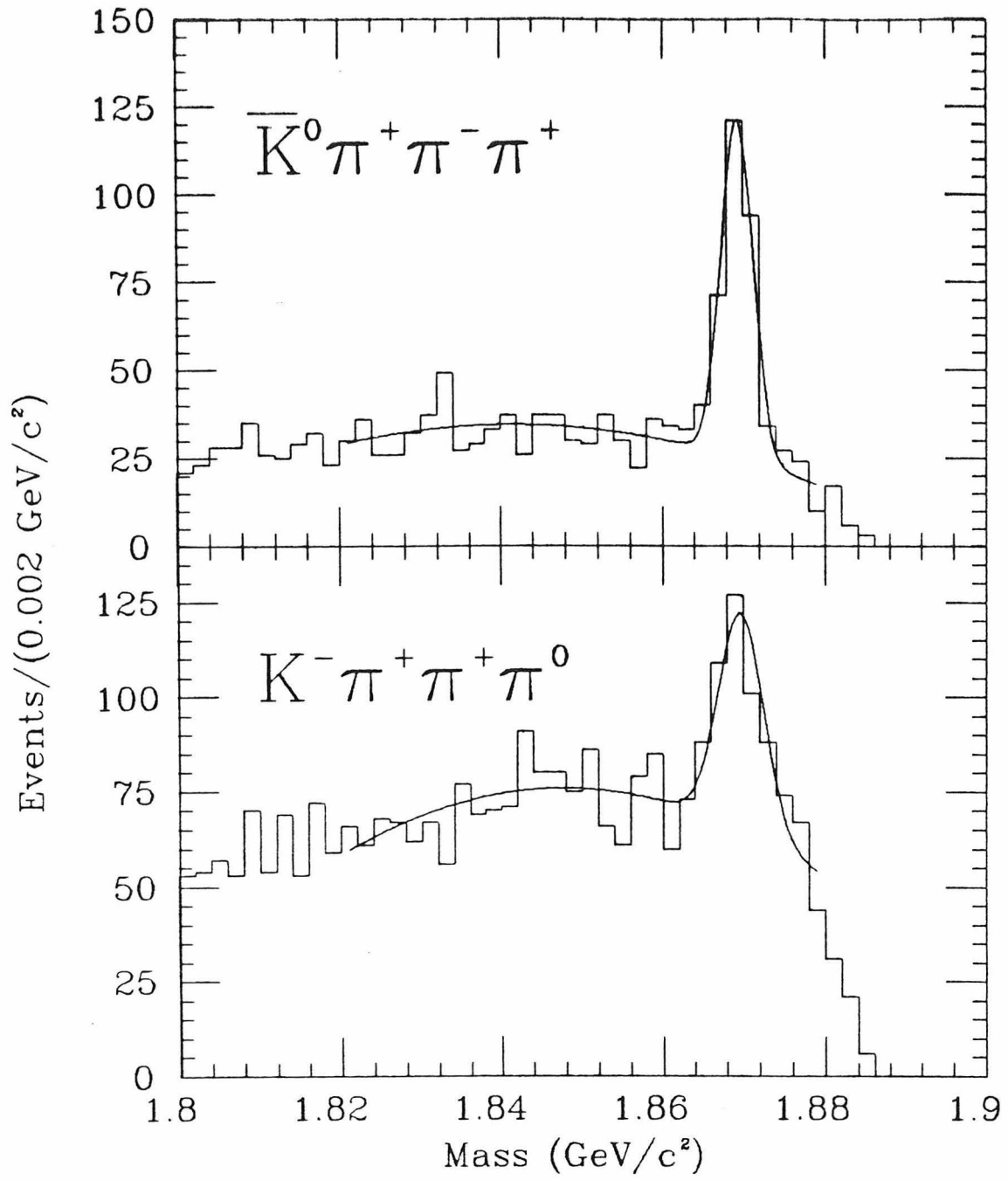
Figure 3.13. Beam-constrained mass plots for $\bar{K}^0\pi^+\pi^-\pi^+$ and $K^-\pi^+\pi^+\pi^0$.

from Monte Carlo events produced according to the $\bar{K}^0\phi$ hypothesis, in which the $\cos^2\theta$ angular distribution of the $\phi \to K^+K^-$ decay relative to the $\phi$ momentum direction in the $D^0$ rest frame results in the strong peaks at high and low $K^+\bar{K}^0$ masses and a zero in the middle. The observed $K^+\bar{K}^0$ mass$^2$ distribution is rather uniform, as might be expected from the decay of a scalar or pseudoscalar particle into $K^+K^-$. Two candidates for the low-mass $K^+K^-$ enhancement are the scalar resonances $S^*(975)$ and $\delta^0(980)$. The $S^*$ hypothesis can be ruled out immediately because it decays into $\pi^+\pi^-$ approximately three times as often as to $K^+K^-$, and thus should be quite visible in the Dalitz plot of the $\bar{K}^0\pi^+\pi^-$ final state (Figure 3.10), where it is not observed. The only known decays of the $I = 1$ resonance $\delta$, on the other hand, are to $K\bar{K}$ and $\eta\pi$. The $\eta\pi$ decay is not as easily observed as $K\bar{K}$ in our detector. More fundamentally, the ratio between the $\delta$ branching fractions to $\eta\pi$ and $K\bar{K}$ is not even known, lying perhaps in a range $0.25 - 1.3$. Although little is known about the $\delta$, its rather peculiar line shapes in the $\eta\pi$ and $K\bar{K}$ channels have been parametrized by Flatté using a coupled-channel formalism[55], in which the opening of the $K\bar{K}$ channel above threshold produces a cusp-like behavior in the $\eta\pi$ lineshape. In this parametrization, the $K\bar{K}$ lineshape takes the form:

$$\frac{d\sigma}{dm} = C \left| \frac{m_\delta\sqrt{\Gamma_\delta\Gamma_{KK}}}{m_\delta^2 - m^2 - im_\delta(\Gamma_{\eta\pi} + \Gamma_{KK})} \right|^2$$

$$\Gamma_{\eta\pi} = g_\eta q_\eta$$

$$\Gamma_{KK} = g_K\sqrt{\frac{1}{4}m^2 - m_K^2}\,,$$

where $q_\eta$ is the momentum of the decay products of the $\eta\pi$ decay at mass $m_{K\bar{K}}$, $g_K$ and $g_\eta$ are the squared coupling constants to $K\bar{K}$ and $\eta\pi$ channels, and $m_\delta$ and $\Gamma_\delta$ are the mass and (poorly determined) width of the $\delta$ resonance. Taking

the values:

$$m_\delta = 0.969 \,\text{GeV}/\text{c}^2$$

$$\Gamma_\delta = 0.082 \,\text{GeV}/\text{c}^2$$

$$g_K/g_\eta = 2.0$$

suggested in Reference 55, the $\delta$ line shape is incorporated into the Monte Carlo, resulting in a Dalitz plot for reconstructed events, shown in Figure 3.15(c), which strongly resembles the distribution observed in the data. Figure 3.16 shows the $K^+K^-$ mass projections from (a) the data, (b) Monte Carlo events produced according to the $\bar{K}^0\phi$ hypothesis, and (c) Monte Carlo events produced according to the $\bar{K}^0\delta^0$ hypothesis. Assuming that the $\bar{K}^0 K^+ K^-$ final state is dominated by $\bar{K}^0\delta^0$ production, this $\delta \to K^+K^-$ lineshape is then used to determine the average detection efficiency of 3.3%, from which we derive:

$$\sigma_{D^0} \cdot B(D^0 \to \bar{K}^0\delta^0) \cdot B(\delta^0 \to K^+K^-) = 0.072 \pm 0.018 \pm 0.012 \,\text{nb}\,.$$

It should be noted that, while this value assumes that the $\bar{K}^0\delta^0$ channel dominates the $\bar{K}^0 K^+ K^-$ final state, the $\bar{K}^0 K^+ K^-$ detection efficiency does not depend strongly on this assumption, so that the more general statement:

$$\sigma_{D^0} \cdot B(D^0 \to \bar{K}^0 K^+ K^-) = 0.072 \pm 0.018 \pm 0.012 \,\text{nb}$$

is also valid. To extract a limit on the $D^0 \to \bar{K}^0\phi$ decay without excessive reliance on the exact shape of the $\bar{K}^0\delta^0$ 'background,' we note that the $K^+K^-$ mass distribution expected from the $\bar{K}^0\delta^0$ decay can be approximated by a linear polynomial between limits of 1.0 and 1.1 GeV/c$^2$. Applying such a fit to the $K^+K^-$ mass distribution, using the $\phi$ signal width ($\sigma = 0.0044 \,\text{GeV}/\text{c}^2$) observed in the Monte Carlo for the $\bar{K}^0\phi$ decay, we derive an upper limit of 7.9 signal events at 90% confidence level. The $\bar{K}^0\phi$ detection efficiency of 1.06% then leads to:

$$\sigma_{D^0} \cdot B(D^0 \to \bar{K}^0\phi) < 0.10 \,\text{nb at 90\% confidence level.}$$

Systematic errors which are included in this limit are $K_s^0$ vertex cuts (8%), tracking efficiency (10%), dE/dX efficiency (10%), the absence of fiducial cuts (5%), use of a fixed width for the $\phi \to K^+ K^-$ mass resolution (5%), and total integrated luminosity (5%).

## 3.7   DETERMINATION OF $D^+$ AND $D^0$ CROSS-SECTIONS

In the past, the cross-sections $\sigma_{D^+}$ and $\sigma_{D^0}$ were determined from the $\psi''$ cross-section, found by fitting the plot of $R$ at center-of-mass energies above the $\psi'$ peak to terms which represent: $\psi$ and $\psi'$ radiative tails, a flat non-charm background, a $\beta^3$ charm threshold term, and the $\psi''$ mass, height, and width. The height of the $\psi''$ term is then assumed to represent the $D\bar{D}$ pair production cross-section, and a ratio of approximately 56/44% between $D^0\bar{D}^0$ and $D^+D^-$ pairs is determined by isospin symmetry and $p$-wave phase space[41], given the $D^0$ and $D^+$ masses and an estimate of the $\psi''$ 'effective interaction radius.' Because of our large data sample, we have been able to employ an alternate technique* which is free of the uncertainties and assumptions implicit in the former method.

This technique compares the number of events in which both D meson decays are reconstructed in charge conjugate modes ('double tags') to the total number of reconstructed decays in those modes ('single tags'). Only channels which have large and background-free signals are used. The numbers of events observed can be written:

$$(\# \text{ double tags})_i = \epsilon_t \cdot \epsilon_r \cdot B_i^2 \cdot N_D$$

$$(\# \text{ single tags})_i = \epsilon_t \cdot B_i \cdot N_D \, ,$$

where $\epsilon_t$ is the efficiency for reconstructing a 'tag,' $\epsilon_r$ is the efficiency for reconstructing the recoil decay, $B_i$ is the branching ratio, and $N_D$ is the number of produced D mesons of the appropriate charge. Dividing these two numbers yields:

$$\left[ \frac{\# \text{ double tags}}{\# \text{ single tags}} \right]_i = \epsilon_r \cdot B_i \, .$$

---

* Work done in collaboration with G. Blaylock, Univ. of Illinois (preliminary).
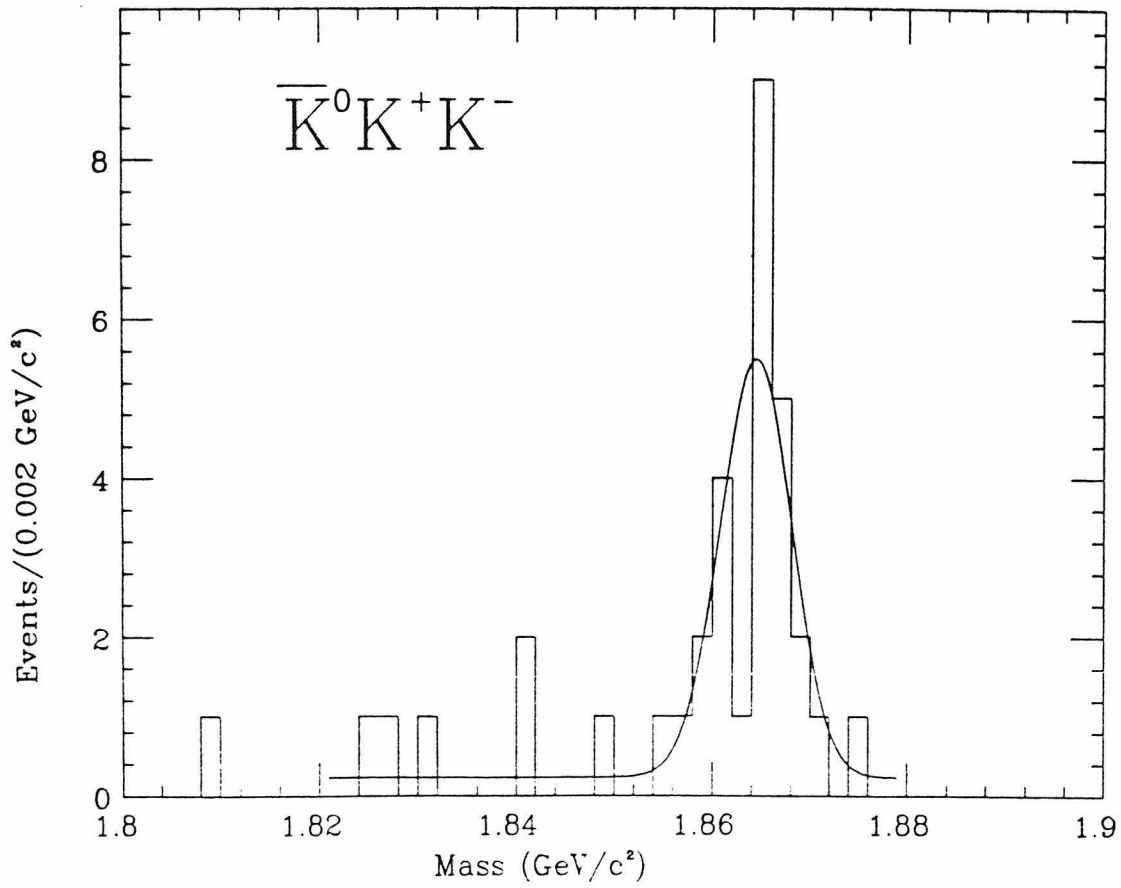
Figure 3.14. Beam-constrained mass plot for $\bar{K}^0 K^+ K^-$.
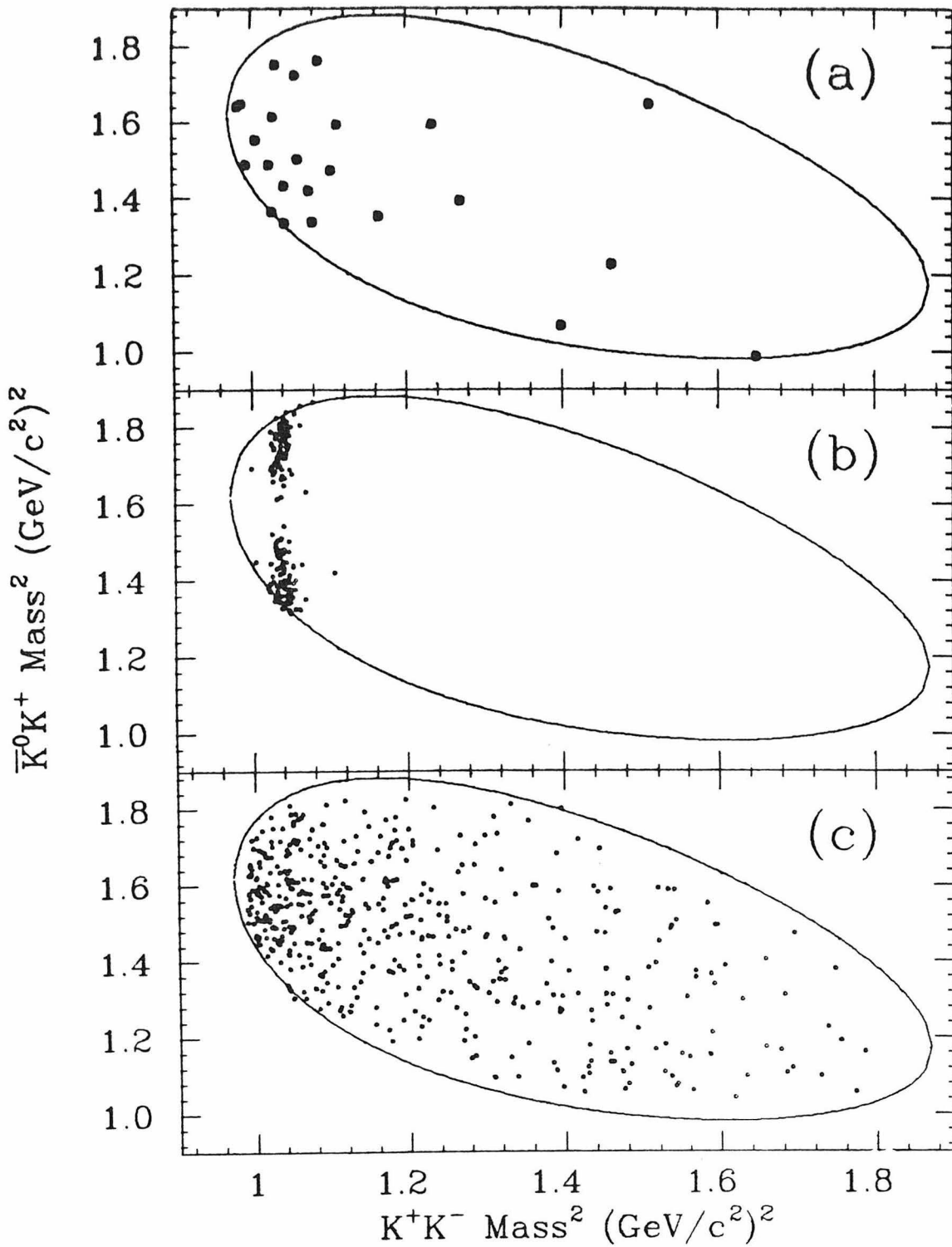
Figure 3.15. Dalitz plots for $D^0 \rightarrow \bar{K}^0 K^+ K^-$ (a) observed in the data, (b) reconstructed from Monte Carlo data produced according to the hypothesis $D^0 \rightarrow \bar{K}^0 \phi$, and (c) reconstructed from Monte Carlo data produced according to the hypothesis $D^0 \rightarrow \bar{K}^0 \delta^0$.
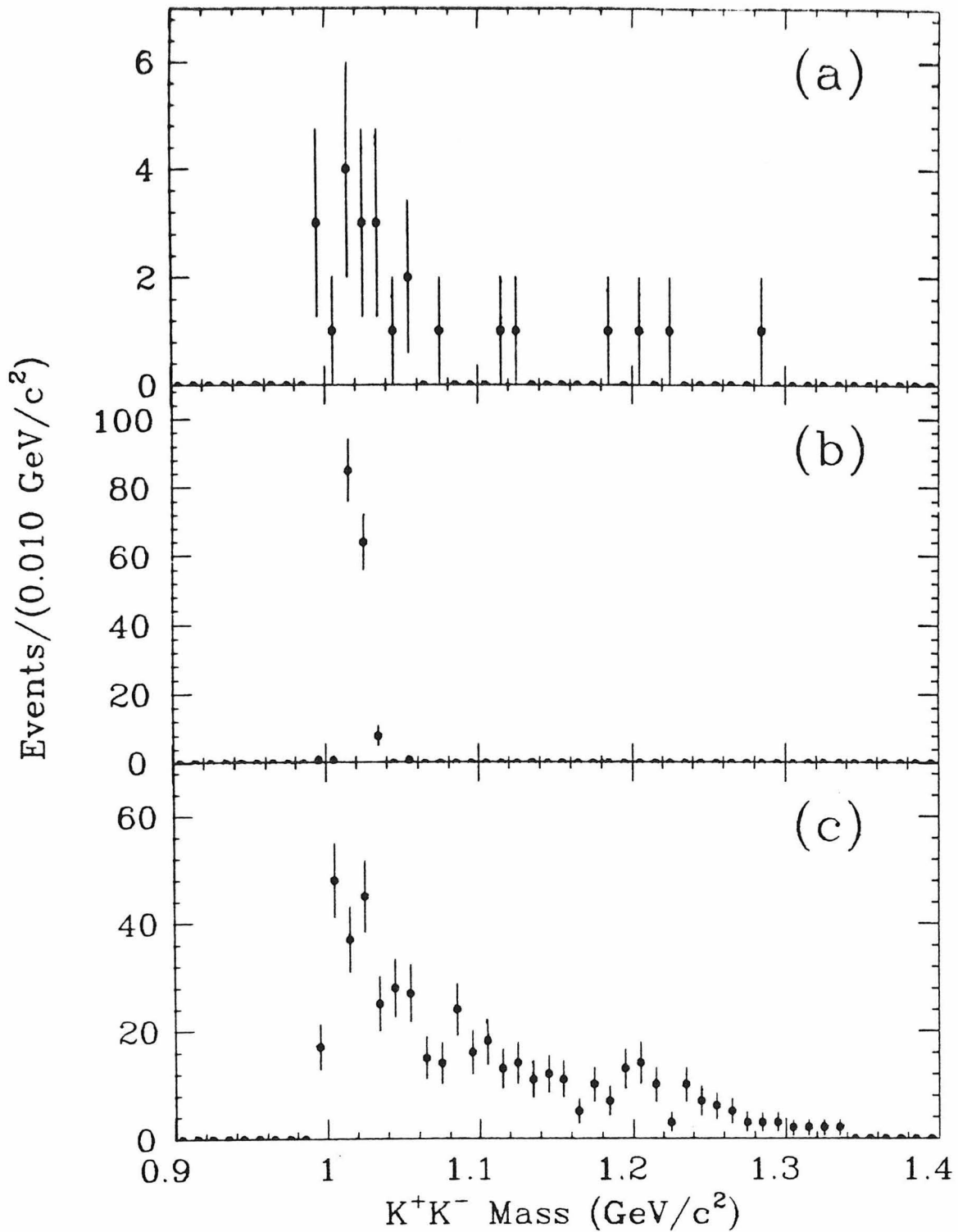
Figure 3.16. $K^+K^-$ mass projections within the $D^0 \rightarrow \bar{K}^0 K^+ K^-$ signal (a) observed in the data, (b) reconstructed from Monte Carlo decays produced according to the hypothesis $D^0 \rightarrow \bar{K}^0 \phi$, and (c) reconstructed from Monte Carlo decays produced according to the hypothesis $D^0 \rightarrow \bar{K}^0 \delta^0$.

Because of the cleanliness of the double tag events, particle identification is not needed to reconstruct the recoil D decay, so that $\epsilon_r$ is easily modeled by the Monte Carlo. From the resulting branching ratios $B_i$ and the accurate measurements of $\sigma \cdot B_i$ already presented, one can determine the cross-sections $\sigma_{D^0}$ and $\sigma_{D^+}$ needed to derive branching ratios in other modes.

This technique is applied to the decays $D^0 \to K^- \pi^+$ and $D^+ \to K^- \pi^+ \pi^+$. Figure 3.17 shows the double tag signals, with the beam-constrained mass of the recoil system plotted against that of the tag. Signals of $(29 \pm 6)$ and $(46 \pm 7)$ events are observed above estimated backgrounds of 1.7 and 2.2 events in the $K^- \pi^+$ and $K^- \pi^+ \pi^+$ plots, respectively. From the number of single tag events, $(978 \pm 33)$ and $(1109 \pm 37)$ in $K^- \pi^+$ and $K^- \pi^+ \pi^+$, respectively, and from the efficiencies for detection of the recoil $K^+ \pi^-$ and $K^+ \pi^- \pi^-$ (0.61 and 0.45, respectively), we derive:

$$B(D^0 \to K^- \pi^+) = (4.9 \pm 0.9 \pm 0.5)\%$$
$$B(D^+ \to K^- \pi^+ \pi^+) = (9.1 \pm 1.5 \pm 0.9)\%,$$

Using these branching ratios together with the $\sigma \cdot B$ values, $(0.237 \pm 0.009 \pm 0.013)$ nb and $(0.399 \pm 0.017 \pm 0.028)$ nb obtained for $K^- \pi^+$ and $K^- \pi^+ \pi^+$, respectively, we derive the average cross-sections:

$$\sigma_{D^+} = (4.4 \pm 0.8 \pm 0.5) \, \text{nb}$$
$$\sigma_{D^0} = (4.8 \pm 0.9 \pm 0.6) \, \text{nb}$$

in our $\psi''$ data sample.

The $\sigma \cdot B$ and $B$ measurements of these two modes made by LGW and Mark II using the former technique are compared to the Mark III numbers derived by the present technique in Figure 3.18. It is clear that the branching ratios determined in this absolute way are significantly higher than those which rely on normalization from the $\psi''$ cross-section, although the production rates for these decays $(\sigma \cdot B)$ are comparable. While these preliminary measurements have large statistical errors, a large increase in the number of double tag events
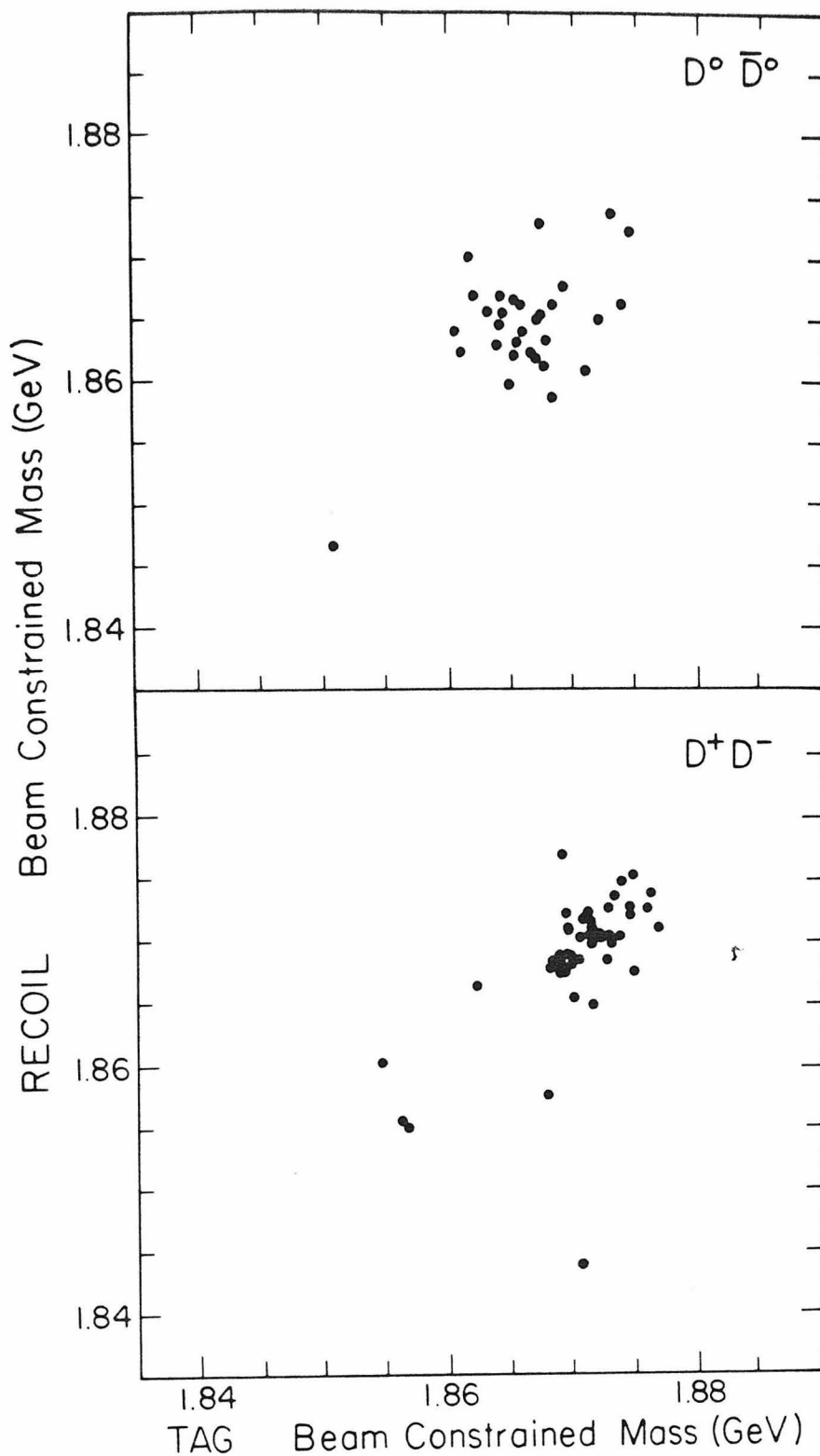
Figure 3.17. Double tag scatter plots of (a) tagged $D^0 \rightarrow K^-\pi^+$ versus $\bar{D}^0 \rightarrow K^+\pi^-$, and (b) tagged $D^+ \rightarrow K^-\pi^+\pi^+$ versus $D^- \rightarrow K^+\pi^-\pi^-$.

should result from the application of kinematic fitting and by use of other decay modes.

## 3.8 SUMMARY

The numbers contained in Table 3.1 summarize the measurements of Cabibbo-allowed D decays to exclusive final states which have been presented in this chapter, both in terms of $\sigma \cdot B$ and as branching ratios, using the cross-sections presented in the previous section for normalization. Ratios between decay rates to final states from either $D^+$ or $D^0$ decay are most accurately derived from the $\sigma \cdot B$ measurements. In the same way, Table 3.2 summarizes the measurements of resonant content in the three-body $K\pi\pi$ decays. In $K^*\pi$ modes, appropriate Clebsch-Gordan coefficients (66.7% for $\bar{K}^{*0} \to K^-\pi^+$ and $K^{*-} \to \bar{K}^0\pi^-$; 33.3% for $\bar{K}^{*0} \to \bar{K}^0\pi^0$ and $K^{*-} \to K^-\pi^0$) are used in addition to the measurements of Dalitz plot fractions to unfold the true $\sigma \cdot B$ and branching ratio measurements.
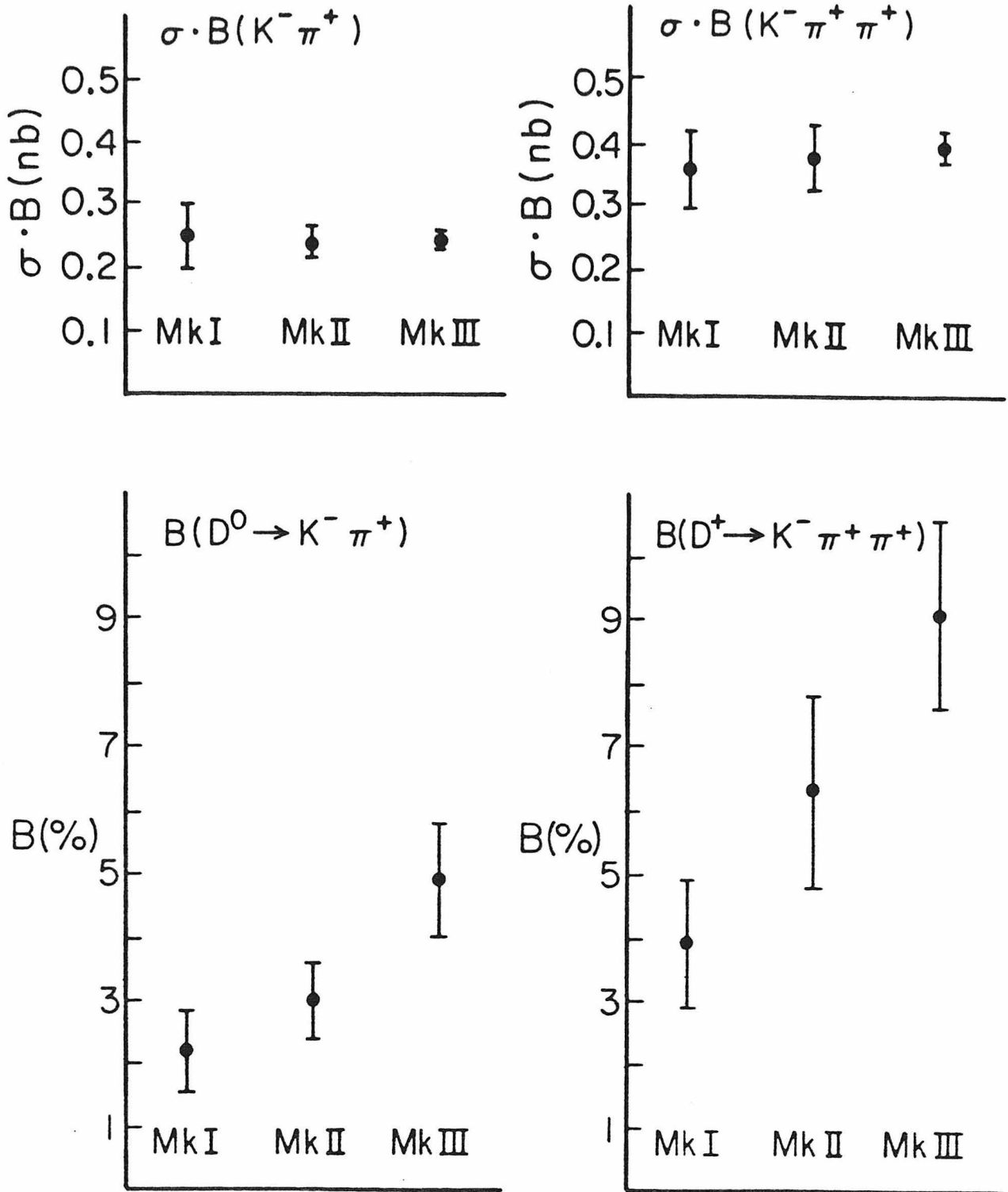
Figure 3.18. Comparison of production rates and branching ratios for $D^0 \to K^-\pi^+$ and $D^+ \to K^-\pi^+\pi^+$ as measured by Mark I (LGW), Mark II, and Mark III. Only the statistical error of the Mark III measurement is shown.

Table 3.1. Summary of branching ratios to Cabibbo-favored channels, using $\sigma_{D^+} = 4.4 \pm 0.8 \pm 0.5\,\mathrm{nb}$ and $\sigma_{D^0} = 4.8 \pm 0.9 \pm 0.6\,\mathrm{nb}$.

| Mode | Events | $\epsilon$ | $\sigma \cdot B$ (nb) | $B(\%)$ |
|---|---|---|---|---|
| $D^0 \rightarrow$ | | | | |
| $K^-\pi^+$ | $1298 \pm 44$ | 0.588 | $0.237 \pm 0.009 \pm 0.013$ | $4.9 \pm 0.9 \pm 0.5$ |
| $\bar{K}^0\pi^0$ | $70 \pm 12$ | 0.069 | $0.108 \pm 0.020 \pm 0.010$ | $2.2 \pm 0.6 \pm 0.4$ |
| $\bar{K}^0\eta$ | $28 \pm 12$ | 0.034 | $0.088 \pm 0.039 \pm 0.012$ | $1.8 \pm 0.9 \pm 0.3$ |
| $\bar{K}^0\omega$ | $24 \pm 9$ | 0.014 | $0.187 \pm 0.073 \pm 0.047$ | $3.9 \pm 1.7 \pm 1.1$ |
| $\bar{K}^0\phi$ | $< 7.9$ | 0.011 | $< 0.10$ | $< 2.4@90\%$ C.L. |
| $K^-\pi^+\pi^0$ | $1250 \pm 68$ | 0.137 | $0.978 \pm 0.065 \pm 0.137$ | $20.4 \pm 4.1 \pm 3.8$ |
| $\bar{K}^0\pi^+\pi^-$ | $291 \pm 22$ | 0.084 | $0.372 \pm 0.030 \pm 0.031$ | $7.7 \pm 1.6 \pm 1.2$ |
| $\bar{K}^0 K^+ K^-$ | $22 \pm 5$ | 0.033 | $0.072 \pm 0.018 \pm 0.012$ | $1.5 \pm 0.5 \pm 0.3$ |
| $K^-\pi^+\pi^-\pi^+$ | $1103 \pm 44$ | 0.209 | $0.566 \pm 0.027 \pm 0.061$ | $11.8 \pm 2.3 \pm 2.0$ |
| $\bar{K}^0\pi^+\pi^-\pi^0$ | $169 \pm 26$ | 0.027 | $0.666 \pm 0.113 \pm 0.153$ | $13.9 \pm 3.5 \pm 3.6$ |
| $D^+ \rightarrow$ | | | | |
| $\bar{K}^0\pi^+$ | $147 \pm 14$ | 0.125 | $0.126 \pm 0.012 \pm 0.009$ | $2.9 \pm 0.6 \pm 0.4$ |
| $K^-\pi^+\pi^+$ | $1166 \pm 41$ | 0.313 | $0.399 \pm 0.017 \pm 0.028$ | $9.1 \pm 1.5 \pm 0.9$ |
| $\bar{K}^0\pi^+\pi^0$ | $239 \pm 45$ | 0.036 | $0.714 \pm 0.142 \pm 0.100$ | $16.2 \pm 4.4 \pm 2.9$ |
| $\bar{K}^0\pi^+\pi^-\pi^+$ | $236 \pm 22$ | 0.083 | $0.305 \pm 0.031 \pm 0.030$ | $6.9 \pm 1.4 \pm 1.0$ |
| $K^-\pi^+\pi^+\pi^0$ | $197 \pm 28$ | 0.081 | $0.260 \pm 0.040 \pm 0.054$ | $5.9 \pm 1.4 \pm 1.4$ |

Table 3.2. Resonance content of three-body $K\pi\pi$ channels.

| Mode | Fraction | $\sigma \cdot B$ (nb) | $B(\%)$ |
|---|---|---|---|
| $D^0 \to$ | | | |
| $K^-\pi^+\pi^0$ | | | |
| $K^-\rho^+$ | $0.74 \pm 0.05 \pm 0.05$ | $0.724 \pm 0.069 \pm 0.113$ | $15.1 \pm 3.2 \pm 3.0$ |
| $K^{*-}\pi^+$ | $0.13 \pm 0.03 \pm 0.02$ | $0.381 \pm 0.093 \pm 0.078$ | $7.9 \pm 2.4 \pm 1.9$ |
| $\bar{K}^{*0}\pi^0$ | $0.08 \pm 0.03 \pm 0.02$ | $0.117 \pm 0.045 \pm 0.033$ | $2.5 \pm 1.0 \pm 0.8$ |
| Non $-$ resonant | $0.05 \pm 0.04 \pm 0.03$ | $0.049 \pm 0.039 \pm 0.030$ | $1.0 \pm 0.8 \pm 0.6$ |
| | | | |
| $\bar{K}^0\pi^+\pi^-$ | | | |
| $\bar{K}^0\rho^0$ | $0.17 \pm 0.05 \pm 0.03$ | $0.063 \pm 0.019 \pm 0.012$ | $1.3 \pm 0.5 \pm 0.3$ |
| $K^{*-}\pi^+$ | $0.64 \pm 0.08 \pm 0.05$ | $0.357 \pm 0.052 \pm 0.040$ | $7.4 \pm 1.8 \pm 1.3$ |
| Non $-$ resonant | $0.19 \pm 0.09 \pm 0.04$ | $0.071 \pm 0.034 \pm 0.016$ | $1.5 \pm 0.8 \pm 0.4$ |
| $D^+ \to$ | | | |
| $\bar{K}^0\pi^+\pi^0$ | | | |
| $\bar{K}^0\rho^+$ | $0.87 \pm 0.09 \pm 0.05$ | $0.621 \pm 0.139 \pm 0.094$ | $14.1 \pm 4.1 \pm 2.7$ |
| $\bar{K}^{*0}\pi^+$ | $0.07 \pm 0.04 \pm 0.04$ | $0.150 \pm 0.090 \pm 0.087$ | $3.4 \pm 2.2 \pm 2.0$ |
| Non $-$ resonant | $0.06 \pm 0.06 \pm 0.04$ | $0.043 \pm 0.044 \pm 0.029$ | $1.0 \pm 1.0 \pm 0.7$ |

## 4. Reconstruction of Cabibbo-Suppressed Hadronic Decay Modes

### 4.1 INTRODUCTION

Cabibbo-suppressed decays of D mesons can occur in channels with either zero or two kaons. The first type of Cabibbo-suppressed decay results from the weak transition shown in Figure 1.1(b) involving the matrix element $V_{cd}$, except for final states with hidden $s\bar{s}$ content such as $\phi$. The second type may proceed via the diagram of Figure 1.1(c), suppressed by the matrix element $V_{us}$ of kaon and hyperon decay, or via the diagram of Figure 1.1(b), suppressed by $V_{cd}$, with creation of an $s\bar{s}$ quark pair from the vacuum. The measurements of long B lifetimes[9] and the unitarity of the weak quark mixing matrix lead one to believe that $V_{cd} \approx -V_{us}$ and $V_{cs} \approx V_{ud}$, so that both kinds of Cabibbo-suppressed decay should naively occur at a rate of about $\tan^2 \theta_c = 0.05$ relative to Cabibbo-allowed D decays. The relative enhancement of Cabibbo-suppressed $D^+$ decays predicted by the color cluster interference model[33] should appear in the ratios between similar exclusive $D^+$ decays to Cabibbo-suppressed and allowed channels, as well as inclusively.

In this chapter*, results are quoted as ratios of decay rates to Cabibbo-suppressed channels relative to similar Cabibbo-allowed channels whenever possible. This often allows cancellation of systematic errors, and makes comparison of theory and experiment easier[56].

### 4.2 TWO-BODY ALL-CHARGED DECAYS

In the $K^-K^+$, $K^-\pi^+$ and $\pi^-\pi^+$ decays, at least one particle will have momentum large enough so that $K/\pi$ misidentification by TOF becomes significant. Therefore, tracks are required to lie within the fiducial region defined by $|\cos\theta| < 0.75$, where the TOF counters are efficient and well modeled by

---

* Work done in collaboration with R.H. Schindler, California Institute of Technology.

the Monte Carlo. TOF misidentification is a particular problem here because contamination from the large Cabibbo-allowed $K^-\pi^+$ decay mode via TOF misidentification can be significant relative to the smaller $K^-K^+$ and $\pi^-\pi^+$ signals. Since the momentum of the decay products is equal to the $D^0$ momentum *independent* of their identities, the signal from this contamination peaks at the same mass as the true signals in the $K^-K^+$ and $\pi^-\pi^+$ beam-constrained mass plots. The invariant mass does, however, depend on particle identities: events from $D^0 \rightarrow K^-\pi^+$ where the $\pi$ is misidentified as a K, or vice versa, show up in the $K^-K^+$ and $\pi^-\pi^+$ invariant mass plots near $1.985\,\mathrm{GeV}/c^2$ and $1.745\,\mathrm{GeV}/c^2$, respectively. The technique chosen, therefore, is to cut around the expected $D^0$ momentum within $|\delta P| < 0.050\,\mathrm{GeV}/c$ and then plot the invariant mass of the particle combinations. The resulting $K^-K^+$ and $\pi^-\pi^+$ plots are fitted to a sum of signal and misidentification peaks and a background term, using the mass and width obtained from the dominant $K^-\pi^+$ channel for the signal terms in the suppressed $K^-K^+$ and $\pi^-\pi^+$ channels. Each reflection peak is fitted with a fixed mean and sigma as derived from the Monte Carlo simulation. The shape of the background is determined by the sidebands in momentum, chosen as $|\delta P| \in [0.060, 0.110]\,\mathrm{GeV}/c$, but its height is allowed to vary in the maximum likelihood fit.

Despite the significant misidentification probability, the TOF information remains useful, and is employed in the following manner. All particle hypotheses for each pair of particle are tried. A hypothesis is rejected only if it results in a normalized TOF weight, $W_K/(W_K + W_\pi)$ or $W_\pi/(W_K + W_\pi)$, for one or both particles which is less than 0.30. The resulting mass distributions are shown in Figure 4.1. In the regions where both signals and reflections are absent, the shape of the background obtained from the momentum sidebands is seen to provide an adequate representation of the data. We find $(118 \pm 15)$ $K^-K^+$, $(39 \pm 12)$ $\pi^-\pi^+$, and $(1091 \pm 36)$ $K^-\pi^+$ signal events. Small differences in

detection efficiency, due mainly to kaon decays, lead to the values:

$$\frac{\Gamma(D^0 \to K^- K^+)}{\Gamma(D^0 \to K^- \pi^+)} = 0.122 \pm 0.018 \pm 0.012$$

$$\frac{\Gamma(D^0 \to \pi^- \pi^+)}{\Gamma(D^0 \to K^- \pi^+)} = 0.033 \pm 0.010 \pm 0.006 \,.$$

Systematic errors in these measurements arise from the fitting procedure through the assumption of fixed signal widths (2% and 5% for $K^- K^+$ and $\pi^- \pi^+$, respectively); and through use of the smoothed sidebands to represent the background shape, estimated by varying the amount of smoothing as 2% and 10% for $K^- K^+$ and $\pi^- \pi^+$, respectively. These errors are combined in quadrature, and then added linearly to the other possible errors: $K \leftrightarrow \pi$ misidentification by TOF (4% for $K^- K^+$, $K^- \pi^+$, and $\pi^- \pi^+$), non-Gaussian tails in the mass distributions (1%), and variation in tracking efficiency between pions and kaons (1% for $K^- K^+$ and $\pi^- \pi^+$). In forming the ratios between Cabibbo-suppressed and allowed channels, the errors are again combined in quadrature.

The same technique is employed in the analyses of the decays $D^+ \to \bar{K}^0 K^+$ and $D^+ \to \bar{K}^0 \pi^+$. Here, charged particle identities are assigned simply according to the greatest normalized TOF weight, and standard fiducial and $K^0$ vertex cuts are applied. The mass plots, shown in Figure 4.2, are fitted to sums of signal and reflection peaks and a smoothed background. Signals of $(31 \pm 8)$ and $(141 \pm 13)$ events are obtained in the $\bar{K}^0 K^+$ and $\bar{K}^0 \pi^+$ channels, respectively. Correcting for a slight difference in detection efficiency yields:

$$\frac{\Gamma(D^+ \to \bar{K}^0 K^+)}{\Gamma(D^+ \to \bar{K}^0 \pi^+)} = 0.317 \pm 0.086 \pm 0.048 \,.$$

## 4.3   THREE-BODY ALL-CHARGED DECAYS

The analyses of the $D^+$ decay rates to $\pi^- \pi^+ \pi^+$ and $K^- K^+ \pi^+$ relative to $K^- \pi^+ \pi^+$ are similar to that of the two-body decay analyses described in the
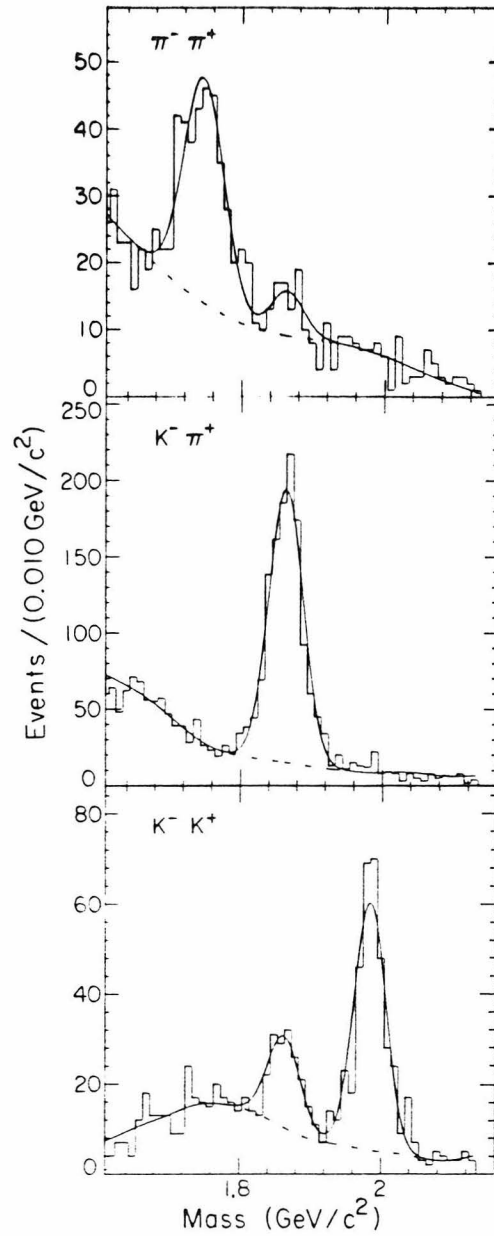
Figure 4.1. Invariant mass plots for $K^-K^+$, $K^-\pi^+$, and $\pi^-\pi^+$.
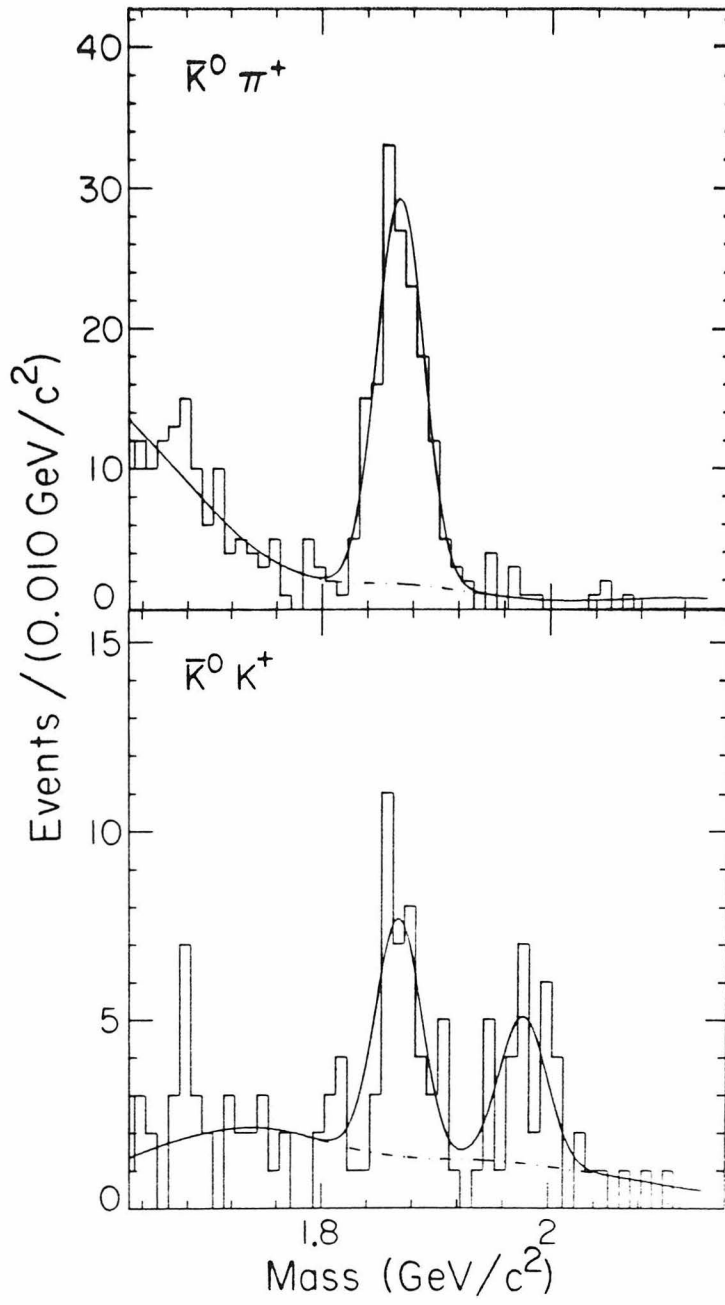
Figure 4.2. Invariant mass plots for $\bar{K}^0 K^+$ and $\bar{K}^0 \pi^+$.

previous section. Once again, the sidebands in momentum are used to determine the background shape used in fitting the signal plot. The mean and width of the TOF misidentification peak in the $K^-K^+\pi^+$ channel are fixed at the values determined by the Monte Carlo, while the reflection peak from $K^-\pi^+\pi^+$ in the $\pi^-\pi^+\pi^+$ mass plot, found to be very non-Gaussian, is represented by the actual (smoothed) shape observed in the Monte Carlo. In the $\pi^-\pi^+\pi^+$ analysis, the invariant masses of both $\pi^+\pi^-$ combinations are required to lie outside of the very wide range $[0.445, 0.545]\,\mathrm{GeV/c^2}$ to guarantee that no events from the Cabibbo-allowed $D^+ \to \bar{K}^0\pi^+$ decay enter the $\pi^-\pi^+\pi^+$ event sample.

The three-body mass plots are shown in Figure 4.3. The fits yield $(78 \pm 13)$ signal events in $K^-K^+\pi^+$, $(57 \pm 21)$ signal events in $\pi^-\pi^+\pi^+$, and $(1037 \pm 36)$ signal events in $K^-\pi^+\pi^+$. Substructure is observed in the $K^-K^+\pi^+$ final state[57] from $D^+ \to \phi\pi^+$ and $\bar{K}^{*0}K^+$. Observation of substructure in the $\pi^-\pi^+\pi^+$ final state, e.g., from $D^+ \to \rho^0\pi^+$, is made impossible by the large background and small number of signal events observed in this mode. The cut:

$$M_{K^-K^+} \in [1.002, 1.036]\,\mathrm{GeV/c^2}$$

in the $K^-K^+\pi^+$ final state selects the $\phi\pi^+$ contribution, leaving $(22 \pm 5)$ signal events in the $K^-K^+\pi^+$ invariant mass plot shown in Figure 4.4(b). Evidence for the decay $D^+ \to \phi\pi^+$ has been presented previously by the ACCMOR collaboration[58]. In looking for the $\bar{K}^{*0}K^+$ decay, one can exploit the $\cos^2\theta$ distribution of the angle between the direction of the $\bar{K}^{*0}$ decay products and the $\bar{K}^{*0}$ momentum in the $D^+$ rest frame to enhance the signal-to-background ratio. After the requirements:

$$|\cos\theta| > 0.3$$

$$M_{K^-\pi^+} \in [0.842, 0.942]\,\mathrm{GeV/c^2},$$

we obtain the mass plot shown in Figure 4.4(a), containing $(19 \pm 5)$ signal events. With the aid of the Monte Carlo, the fractional overlaps between non-

resonant $K^- K^+ \pi^+$ and resonant $\phi \pi^+$ and $\bar{K}^{*0} K^+$ contributions are estimated. Non-resonant $K^- K^+ \pi^+$ decays contaminate the $\phi \pi^+$ and $\bar{K}^{*0} K^+$ signals with $(1.0 \pm 0.4)$ and $(5.0 \pm 2.0)$ events, respectively. After correcting for this overlap and the detection efficiencies, we find:

$$\Gamma(D^+ \to \pi^- \pi^+ \pi^+)/\Gamma(D^+ \to K^- \pi^+ \pi^+) = 0.042 \pm 0.016 \pm 0.010$$

$$\Gamma(D^+ \to K^- K^+ \pi^+_{non-res})/\Gamma(D^+ \to K^- \pi^+ \pi^+) = 0.059 \pm 0.026 \pm 0.009$$

$$\Gamma(D^+ \to \phi \pi^+)/\Gamma(D^+ \to K^- \pi^+ \pi^+) = 0.084 \pm 0.021 \pm 0.011$$

$$\Gamma(D^+ \to \bar{K}^{*0} K^+)/\Gamma(D^+ \to K^- \pi^+ \pi^+) = 0.048 \pm 0.021 \pm 0.011.$$

## 4.4 FINAL STATES $K^0 \bar{K}^0$ AND $K^{*0} \bar{K}^0$ $(\bar{K}^{*0} K^0)$

Of the Cabibbo-suppressed $D^0$ decays which could arise from W-exchange diagrams, the modes $K^0 \bar{K}^0$, $K^{*0} \bar{K}^0$, and $\bar{K}^{*0} K^0$ are the most easily observed. It should be noted that $K^0 \bar{K}^0$ is forbidden in the exact flavor SU(3) limit (with the conventional mixing matrix), so that this decay may be further suppressed.

For reconstruction of $K^0 \bar{K}^0$, a tight set of cuts on the separation of the $K^0_s$ decay vertex from the primary vertex is necessary to avoid contamination of signal region events from $D^0 \to \bar{K}^0 \pi^+ \pi^-$ decays, in which the $\pi^+ \pi^-$ mass may lie close to that of the $K^0_s$, and one or both of the tracks are mis-measured so as to give an apparent separation from the primary vertex. The main difference from the normal $K^0_s$ vertex cuts is the requirement of a 5 mm, rather than 2 mm, minimum track impact parameter. The $\pi^+ \pi^-$ mass distribution after these tight vertex cuts is shown in Figure 4.5. After a $\pm 0.007 \, \mathrm{GeV}/c^2$ ($2\sigma$) cut on beam-constrained mass, the resulting invariant mass distribution shown in Figure 4.6 contains one event consistent with the $D^0$ mass, as well as a significant level of background. The upper limit for this decay is estimated by fitting this plot between 1.7 and 2.0 $\mathrm{GeV}/c^2$ to a flat background plus a Gaussian centered at 1.865 $\mathrm{GeV}/c^2$ having a width of 0.015 $\mathrm{GeV}/c^2$ as derived from the Monte Carlo
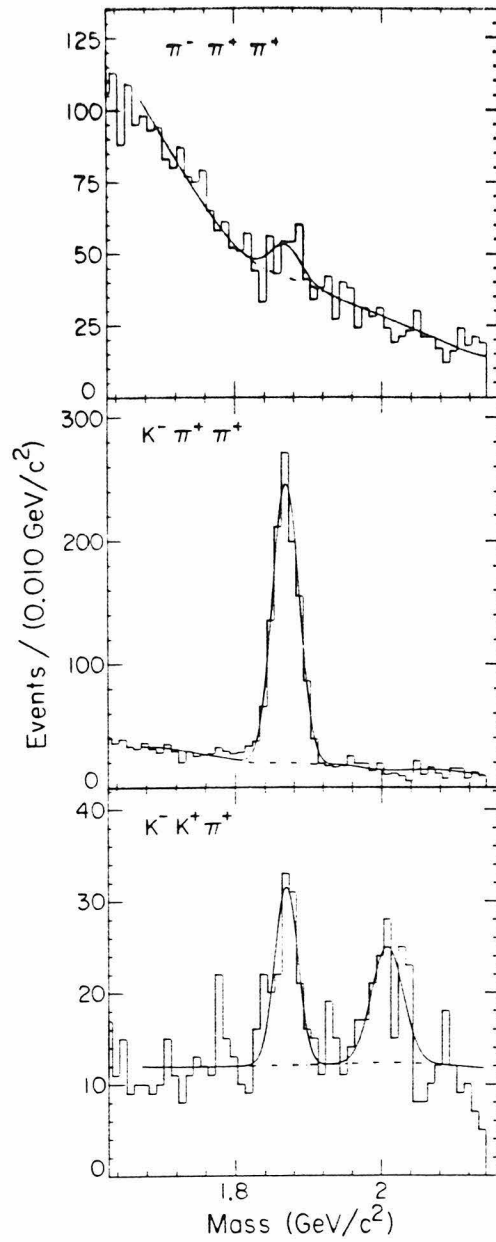
Figure 4.3. Invariant mass plots for $\pi^-\pi^+\pi^+$, $K^-\pi^+\pi^+$, and $K^-K^+\pi^+$.
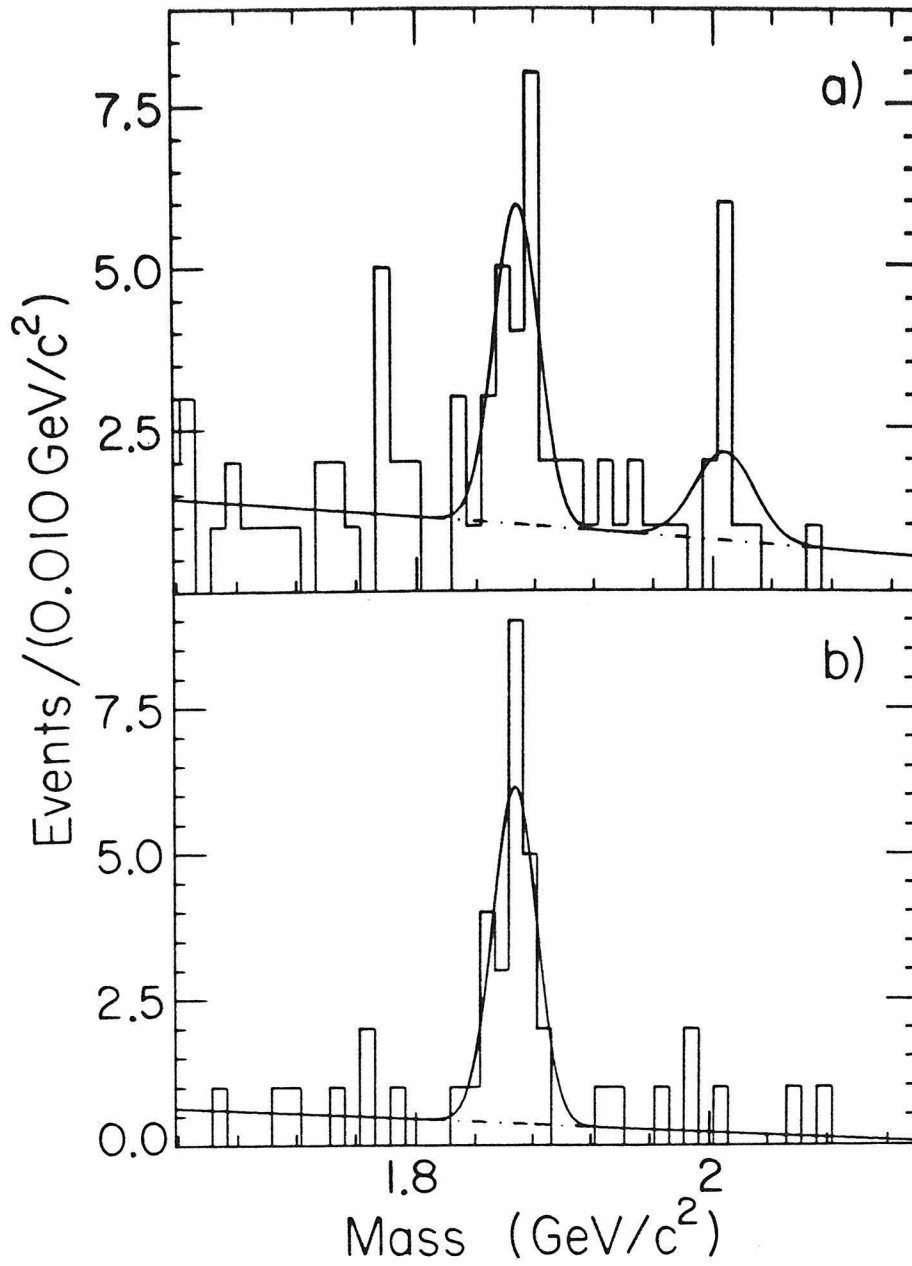
Figure 4.4. Invariant mass plots for $K^-K^+\pi^+$ after cuts to isolate (a) $\bar{K}^{*0}K^+$, and (b) $\phi\pi^+$ components.

simulation. Integration of the resulting likelihood function yields an upper limit of 3.8 events at 90% confidence level. Systematic errors raise this to 4.4 events. From this limit and a detection efficiency of 2.1%, we derive:

$$\frac{\Gamma(D^0 \to K^0 \bar{K}^0)}{\Gamma(D^0 \to K^- \pi^+)} < 0.11 \text{ at } 90\% \text{ confidence level.}$$

Systematic errors which are considered in this measurement include the effect of the tight vertex cuts (10%) and the use of a fixed width determined by Monte Carlo (10%).

The decays $D^0 \to K^{*0}\bar{K}^0$ and $D^0 \to \bar{K}^{*0}K^0$ appear in the final states $K^0 K^- \pi^+$ and $\bar{K}^0 K^+ \pi^-$. It is impossible to separate these two contributions without prior knowledge of the charm of the decaying $D^0$ or $\bar{D}^0$, so that results can only be quoted for the sum of the two charge-conjugate channels. To minimize feed-down from the large Cabibbo-allowed $D^0 \to K^- \pi^+ \pi^- \pi^+$ decay where two pions may appear to be separated from the vertex and have $\pi^+\pi^-$ mass near the $K_s^0$ mass, the tight vertex cuts used in the $K^0 \bar{K}^0$ analysis are again employed. To separate $(K^{*0}\bar{K}^0 + \bar{K}^{*0}K^0)$ from $(K^{*-}K^+ + K^{*+}K^-)$ and the possible non-resonant $K^0 K^- \pi^+ + \bar{K}^0 K^+ \pi^-$ contribution, the mass and angular cuts used to enhance the $\bar{K}^{*0}K^+$ signal within the $K^- K^+ \pi^+$ final state:

$$|\cos\theta| > 0.3$$
$$M_{K\pi} \in [0.842, 0.942] \text{ GeV}/c^2,$$

are employed (using the appropriate $K\pi$ combination in each case) to enhance the $(K^{*0}\bar{K}^0 + \bar{K}^{*0}K^0)$ and $(K^{*-}K^+ + K^{*+}K^-)$ fractions. The non-resonant contribution is isolated by the requirement that $M_{K\pi}$ lie outside of the range $[0.842, 0.942] \text{ GeV}/c^2$. The resulting invariant mass distributions shown in Figure 4.7 are fitted to linear polynomials plus Gaussians of fixed width $\sigma = 0.016 \text{ GeV}/c^2$ as derived from the Monte Carlo. The fits are extended only to $1.960 \text{ GeV}/c^2$ because events from $K^{*-}\pi^+$, where the fast $\pi^+$ is
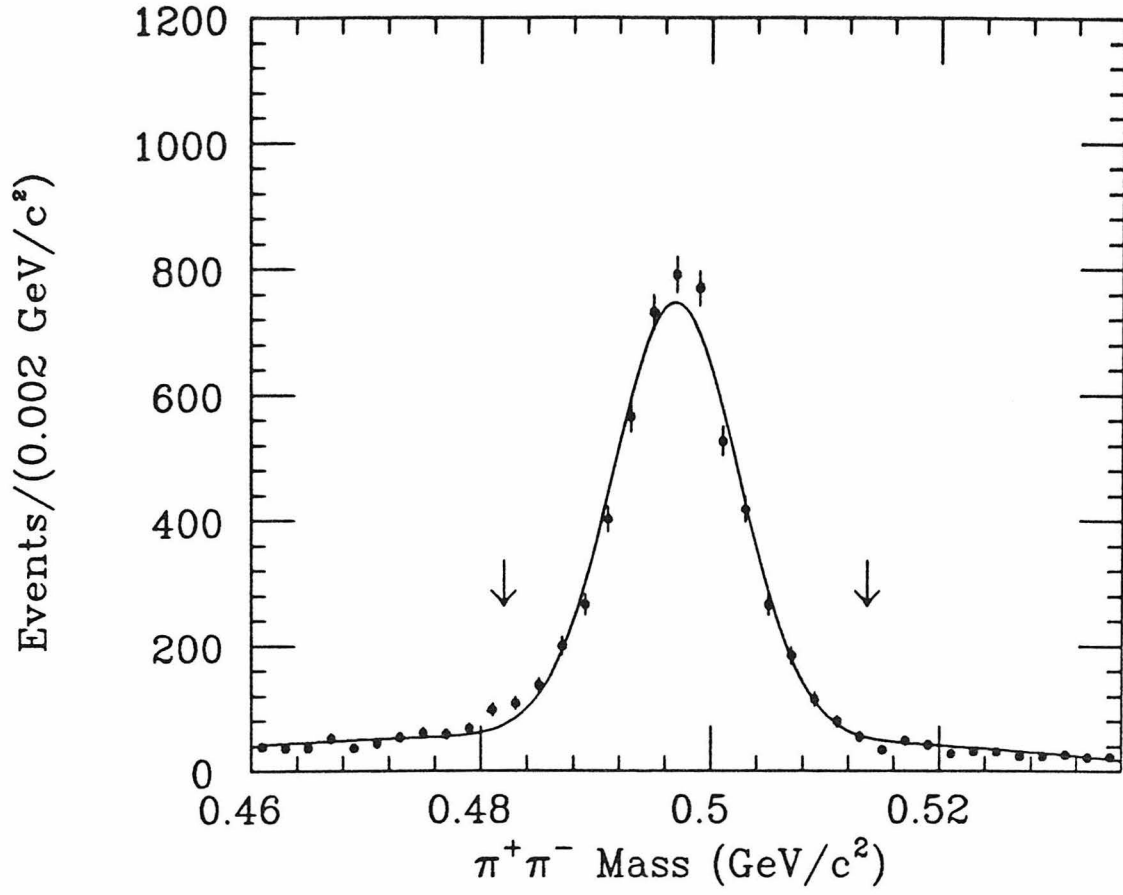
Figure 4.5. Invariant mass of $\pi^+\pi^-$ combinations after tight vertex displacement cuts. Arrows indicate the mass cuts used to select $K_s^0$ candidates.
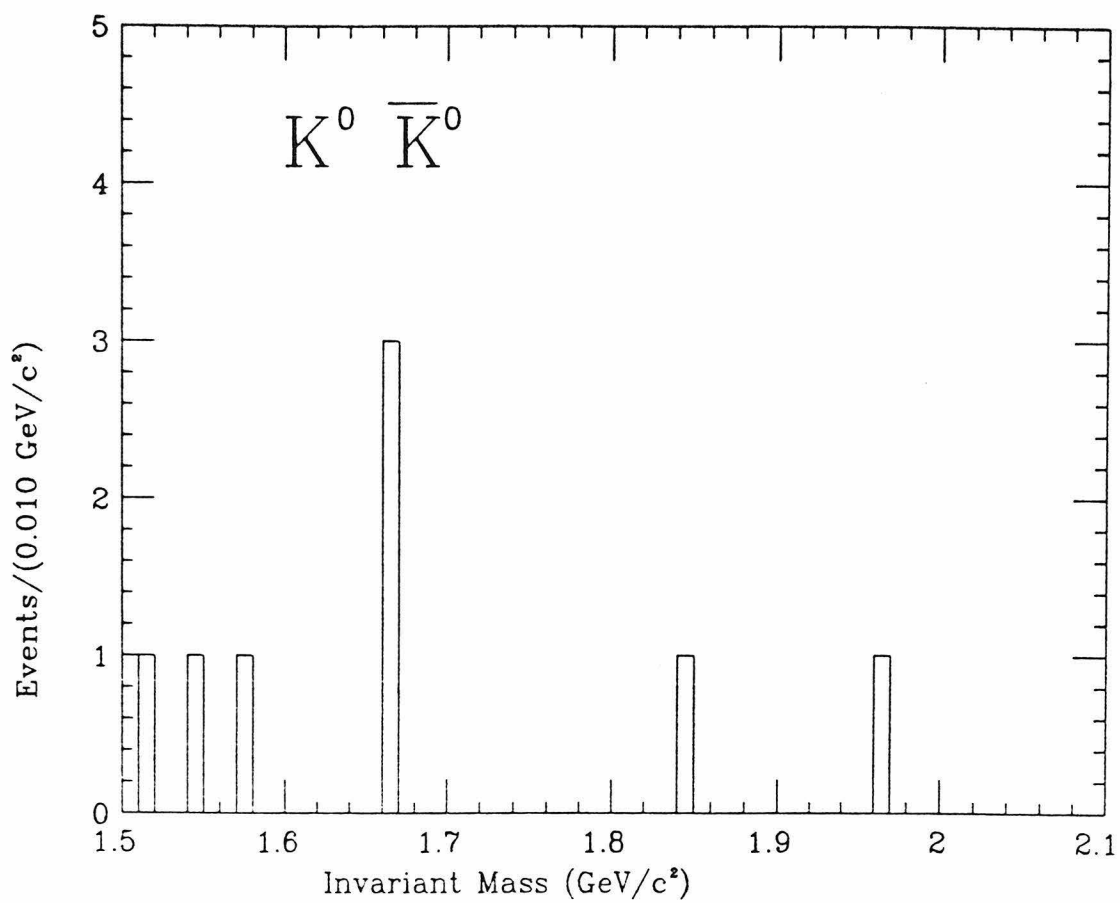
Figure 4.6. Invariant mass plot for $K^0\bar{K}^0$.

misidentified as a kaon by TOF, peak between $1.960 - 2.090 \, \text{GeV}/c^2$. The misidentification peak from $K^{*-}\pi^+$ is particularly apparent on the right side of the $(K^{*-}K^+ + K^{*+}K^-)$ mass plot. Signals of $(13.3^{+6.1}_{-5.5})$ non-resonant $K^0K^-\pi^+ + \bar{K}^0K^+\pi^-$ events, $(2.2^{+2.6}_{-2.0})$ $(K^{*0}\bar{K}^0 + \bar{K}^{*0}K^0)$ events, and $(12.4 \pm 4.2)$ $(K^{*-}K^+ + K^{*+}K^-)$ events are derived. Feed-down from $K^-\pi^+\pi^-\pi^+$ events is accounted for by using sidebands in $\pi^+\pi^-$ mass from the $K^0_s$ mass peak:

$$M(\pi^+\pi^-) \in \begin{cases} [0.460, 0.476] \, \text{GeV}/c^2 & \text{or} \\ [0.520, 0.536] \, \text{GeV}/c^2 \, , \end{cases}$$

and applying the same analysis. Feed-down from $K^-\pi^+\pi^-\pi^+$ is estimated as $(5.2^{+3.4}_{-2.8})$ events in non-resonant $K^0K^-\pi^+ + \bar{K}^0K^+\pi^-$, $(0.0^{+0.5}_{-0.0})$ events in $(K^{*0}\bar{K}^0 + \bar{K}^{*0}K^0)$, and $(1.3^{+1.3}_{-0.8})$ events in $(K^{*-}K^+ + K^{*+}K^-)$. The Monte Carlo is then used to evaluate detection efficiencies and overlap between resonant and non-resonant contributions, to form an efficiency matrix between the number of events produced in the three different channels and the number of events actually observed after the sets of cuts used to help isolate the contributions. By using the inverse of this matrix, and subtracting the estimates of $K^-\pi^+\pi^-\pi^+$ feed-down, we derive:

$$\sigma_{D^0} \cdot B(D^0 \to K^0K^-\pi^+ + \bar{K}^0K^+\pi^-)_{non-res} < 0.079 \, \text{nb at 90\% C.L.}$$

$$\sigma_{D^0} \cdot B(D^0 \to K^{*0}\bar{K}^0 + \bar{K}^{*0}K^0) < 0.036 \, \text{nb at 90\% C.L.}$$

$$\sigma_{D^0} \cdot B(D^0 \to K^{*-}K^+ + K^{*+}K^-) = 0.050 \pm 0.023 \pm 0.010 \, \text{nb.}$$

The systematic errors in these measurements include contributions from the efficiency of $K^0_s$ vertex cuts (10%), tracking efficiency (10%), the absence of fiducial cuts (5%), requiring TOF identification of the kaon (5%), use of a fixed width determined by Monte Carlo in the mass plot fits (10%), and total integrated luminosity (5%). Using results from the previous chapter, we quote:

$$\frac{\Gamma(D^0 \to K^{*-}K^+ + K^{*+}K^-)}{\Gamma(D^0 \to K^{*-}\pi^+ + K^-\rho^+)} = 0.05 \pm 0.03 \, ,$$

including systematic errors, as well as:

$$\frac{\Gamma(D^0 \to K^{*0}\bar{K}^0 + \bar{K}^{*0}K^0)}{\Gamma(D^0 \to K^{*-}\pi^+ + K^-\rho^+)} < 0.034 \text{ at } 90\% \text{ C.L.}$$

## 4.5 MULTI-PION CHANNELS

This section describes the analyses of the decays $D^+ \to \pi^0\pi^+$, $D^0 \to \pi^-\pi^+\pi^0$, and $D^0 \to \pi^-\pi^+\pi^-\pi^+$. The difficulty of measuring small signals on large backgrounds in all-pion modes is first illustrated by an analysis of the $\pi^0\pi^+$ mode which is similar to previous analyses of Cabibbo-allowed decay modes containing a $\pi^0$. A different approach is then taken in an attempt to decrease the level of background, by looking for the $\pi^0\pi^+$ decay in the recoil from fully reconstructed 'tagged' $D^+$ mesons. This method is also used to isolate signals for $D^0$ decays to $\pi^-\pi^+\pi^0$ and $\pi^-\pi^+\pi^-\pi^+$.

The decay $D^+ \to \pi^0\pi^+$ is insensitive to charged particle misidentification, as it can be confused only with the *twice* Cabibbo-suppressed decay $D^+ \to K^+\pi^0$. We may therefore use the two-constraint kinematic fit to the beam energy and the $\pi^0$ mass described in the previous chapter to better determine the photons' energies and positions. The fitted photon energies are required to be greater than $0.150$ GeV. Previous inclusive measurements[22] have shown the fraction of $D^+$ decays with charged multiplicity greater than three to be about 4%. Therefore, a cut which is effective only for this one-track decay, is to require that the number of charged particles in the event observed to be recoiling from the $\pi^0\pi^+$ candidate be three or less. Figure 4.8 shows the resulting mass distributions in the 'signal' region where $\chi^2 < 6$, and in the 'control' region defined by $10 < \chi^2 < 100$. These plots are then fitted to a quadratic background term plus a Gaussian at the $D^+$ mass having a width fixed at $0.0034$ GeV/c$^2$, the value obtained from the Monte Carlo. The signal plot shows an enhancement of modest significance containing $(28\pm16)$ signal events. The control plot shows no such enhancement, and contains
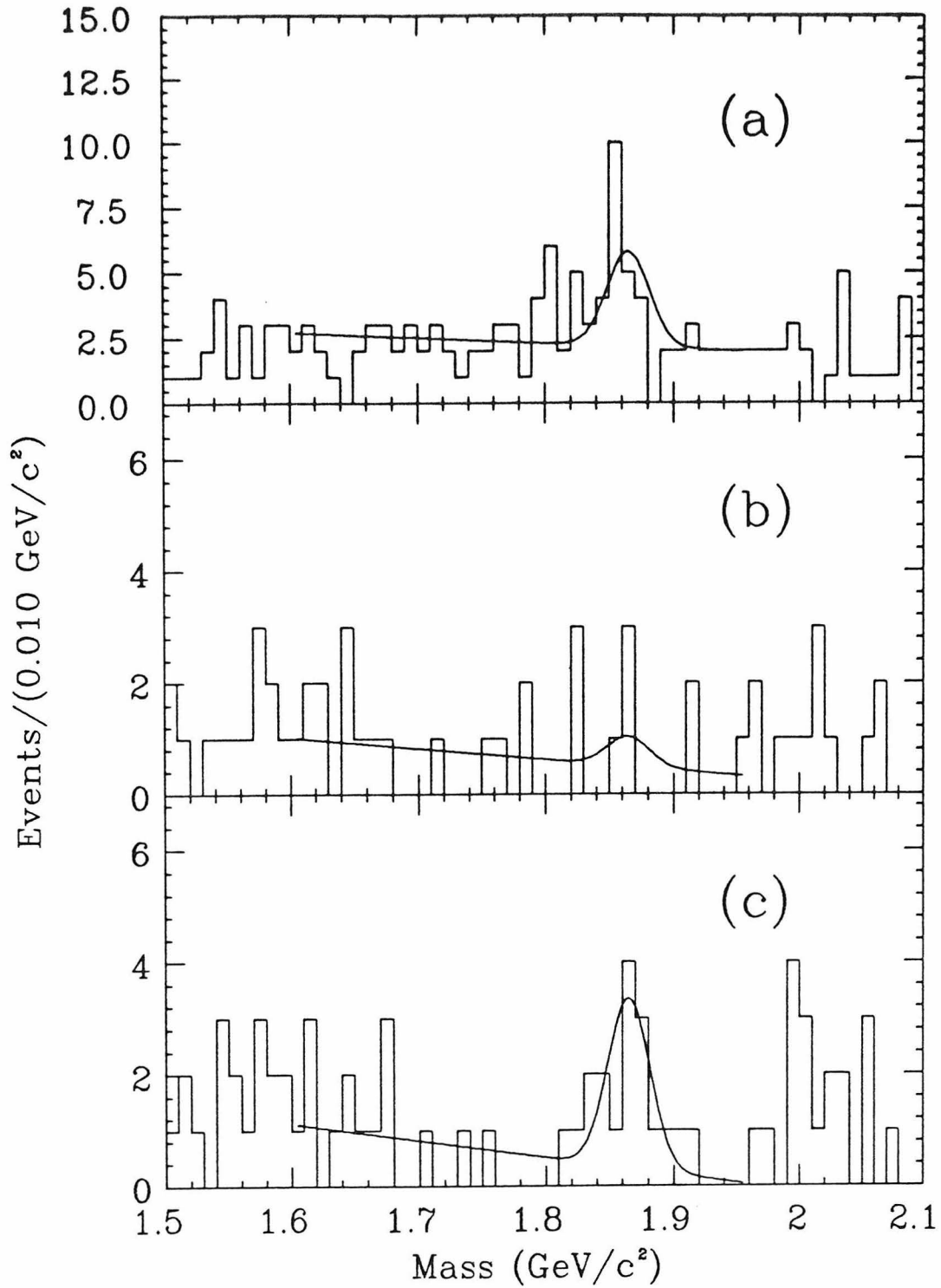
Figure 4.7. Invariant mass plots for $D^0 \rightarrow (K^0 K^- \pi^+ + \bar{K}^0 K^+ \pi^-)$ (a) after cuts to isolate the non-resonant contribution, (b) after cuts which isolate $K^{*0}\bar{K}^0$ and $\bar{K}^{*0}K^0$ components, and (c) after cuts which isolate $K^{*-}K^+$ and $K^{*+}K^-$ components.

$(0 \pm 10)$ signal events. The quadratic background is seen to adequately represent the data in both signal and control plots. After correcting for efficiency and using the value of $\sigma_{D^+} \cdot B(D^+ \to \bar{K}^0 \pi^+)$ from the previous chapter, we derive:

$$\frac{\Gamma(D^+ \to \pi^0 \pi^+)}{\Gamma(D^+ \to \bar{K}^0 \pi^+)} = 0.095 \pm 0.052 \pm 0.015 \,,$$

leading to an upper limit of 0.23 at 90% confidence level as well for this ratio. Systematic errors result from the requirement of 3 or fewer recoil charged tracks (2%), the $\chi^2$ cut on the two-constraint fit to photon energies and directions (5%), the assumption of a quadratic background (10%), and use of a fixed width in fitting the mass plot (5%).

Another approach to the analysis of the $\pi^0 \pi^+$ decay looks for a signal in the recoil from $D^+$ decays which are reconstructed in $K^- \pi^+ \pi^+$, $\bar{K}^0 \pi^+$, or $\bar{K}^0 \pi^+ \pi^- \pi^+$ channels. The reconstruction of these large hadronic $D^+$ decay channels follows the same procedure as described in chapter 3, except that fiducial cuts imposed on charged tracks and photons are removed so as to maximize the number of reconstructed decays. The recoil spectrum from these decays is then required to contain a single charged track and two or more apparent photons. No TOF identification is required for the single charged recoil track, since there are very few $D^+$ decays which produce a fast charged kaon and no other charged tracks which could, in principle, furnish a background to this decay. The charged track is combined with all permutations of two photons, and fitted to the beam energy and $\pi^0$ mass constraints. Combinations having a photon with fitted energy below 0.050 GeV are rejected, and a cut of $\chi^2 < 6$ selects $\pi^0 \pi^+$ candidates. A dramatic decrease in background is then achieved by requiring the momentum of the reconstructed $D^+$ plus that of the $\pi^0 \pi^+$ candidate to be less than 0.080 GeV/c, i.e., the total event momentum must be consistent with zero. The resulting plot of $\pi^0 \pi^+$ beam-constrained mass, shown in Figure 4.9(a), contains one event lying precisely at the $D^+$ mass. The mass
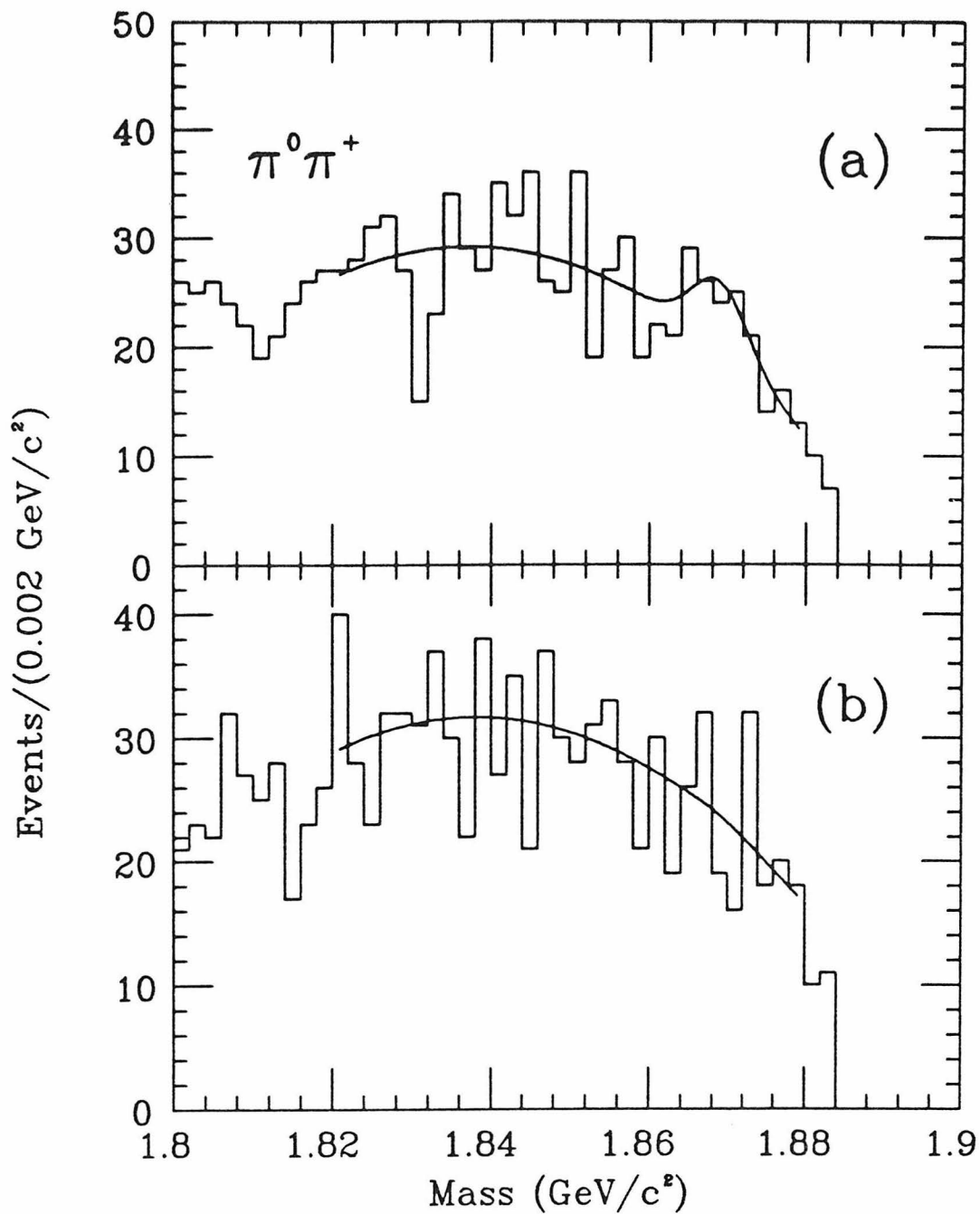
Figure 4.8. Beam-constrained mass plots for $\pi^0\pi^+$ (a) in the signal region where $\chi^2 < 6$, and (b) in the background region defined by $10 < \chi^2 < 100$.

resolution after the above cuts is $0.003\,\mathrm{GeV}/c^2$. One event treated as a signal gives an upper limit of 3.9 events at 90% confidence level by Poisson statistics. Systematic errors, coming from the $\chi^2$ cut on the two-constraint fit to photon energies and directions (5%), photon detection efficiency (5%), and the absence of fiducial cuts (2%), raise the upper limit to 4.2 events in $(1729 \pm 20)$ tag events. Combined with the detection efficiency of 46%, we derive:

$$B(D^+ \to \pi^0 \pi^+) < 0.53\% \text{ at } 90\% \text{ confidence level.}$$

Using the branching ratio of 2.9% obtained for $D^+ \to \bar{K}^0 \pi^+$, we derive:

$$\frac{\Gamma(D^+ \to \pi^0 \pi^+)}{\Gamma(D^+ \to \bar{K}^0 \pi^+)} < 0.18 \text{ at } 90\% \text{ confidence level.}$$

Because this analysis is simpler than the previous $\pi^0 \pi^+$ analysis and free from background, this is the preferred measurement.

The reconstruction of $D^0 \to \pi^- \pi^+ \pi^0$ is handled in a similar way using a sample of $(3762 \pm 42)$ $D^0$ hadronic decays reconstructed in the $K^- \pi^+$, $K^- \pi^+ \pi^0$, $\bar{K}^0 \pi^+ \pi^-$, and $K^- \pi^+ \pi^- \pi^+$ channels; but with a few important distinctions. Here, the possibility of significant background from Cabibbo-allowed modes such as $K^- \pi^+ \pi^0$ forces us to demand that the pions are identified by TOF. Contamination from $\bar{K}^0 \pi^0$ into this final state is eliminated by rejecting events in which the $\pi^+ \pi^-$ invariant mass lies within $0.030\,\mathrm{GeV}/c^2$ of the $K^0_s$ mass. The resulting beam-constrained mass plot is shown in Figure 4.9(b). A fit to this plot using the $\sigma = 0.003\,\mathrm{GeV}/c^2$ signal width predicted by the Monte Carlo and a flat background term yields $(10^{+4}_{-3})$ signal events. Using the detection efficiency of 24% determined from Monte Carlo events produced according to phase space, we derive:

$$B(D^0 \to \pi^- \pi^+ \pi^0) = (1.11^{+0.43}_{-0.35} \pm 0.18)\%.$$
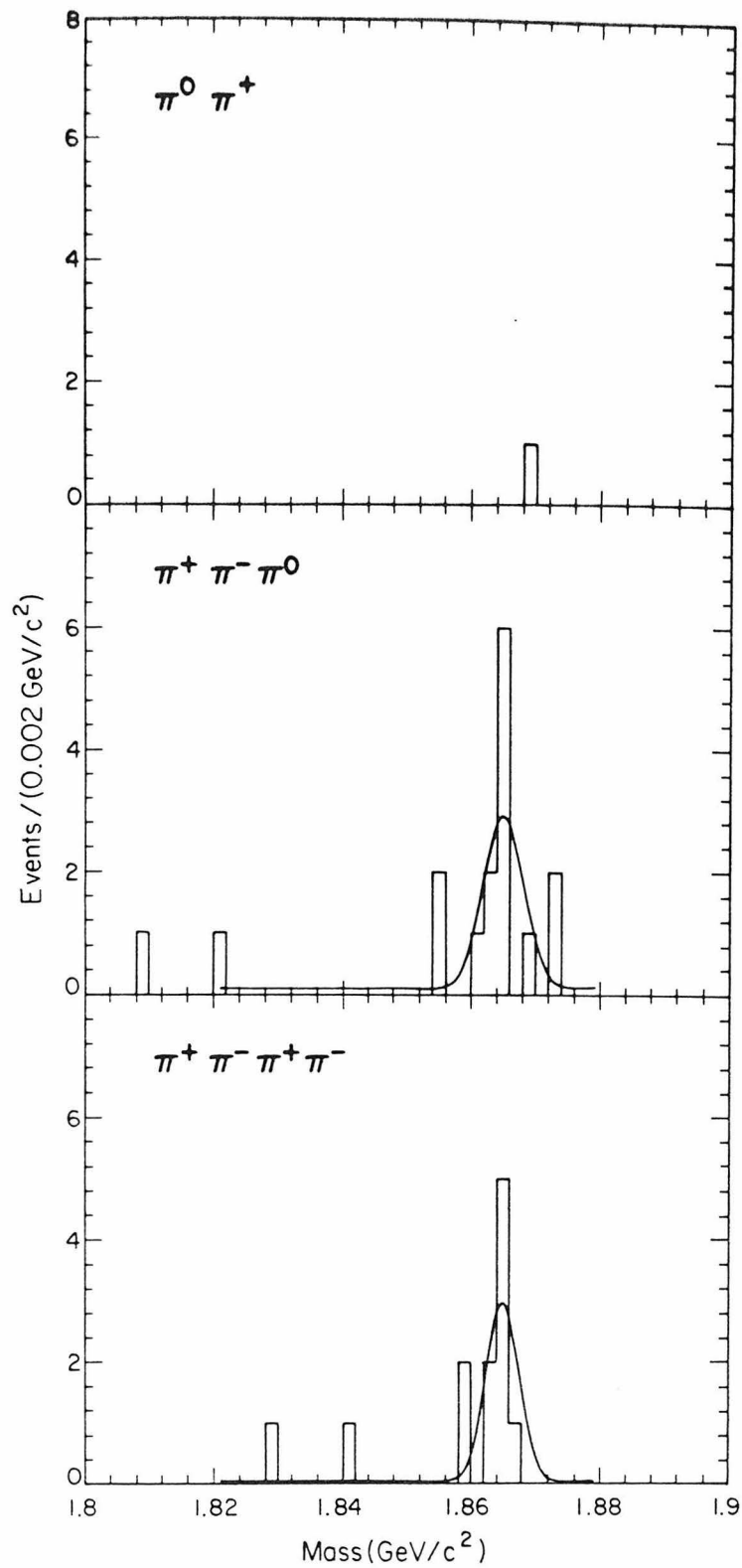
Figure 4.9. Beam-constrained mass for Cabibbo-suppressed all-pion modes in the recoil from D tags.

Here, the quoted systematic error results from the assumption of a fixed signal width (10%), photon detection efficiency (10%), the $\chi^2$ cut on the two-constraint fit to photon energies and directions (5%), and the requirement that the charged pions be identified by TOF (5%).

The charm of the D tag can be used to distinguish between possible contributions to this final state via $D^0 \to \rho^+ \pi^-$ and $D^0 \to \rho^- \pi^+$. The events from $\bar{K}^0 \pi^+ \pi^-$ tags, which have unknown charm, must thus be excluded, leaving $(3435 \pm 39)$ reconstructed $D^0$ decays. The nine remaining $\pi^- \pi^+ \pi^0$ events with mass between $1.858\,\mathrm{GeV}/c^2$ and $1.870\,\mathrm{GeV}/c^2$ form the Dalitz plot shown in Figure 4.10(a). If the $\pi^- \pi^+ \pi^0$ decay occurs through $\rho^0 \pi^0$, the events should cluster at $\pi^+ \pi^-$ masses near that of the $\rho^0$, and $\pi^+ \pi^0$ masses near the top and bottom of the plot, as is indeed observed. Another possibility is that the events are coming from approximately equal decay amplitudes to $\rho^+ \pi^-$ and $\rho^- \pi^+$ which interfere destructively to produce the observed distribution. The corresponding Dalitz plot from $D^0 \to \pi^- \pi^+ \pi^0$ events produced according to phase space in the Monte Carlo, Figure 4.10(b), shows fairly flat acceptance over the whole Dalitz plot.

In the $\pi^- \pi^+ \pi^- \pi^+$ final state, we again require TOF identification of pions, in this case to reject $D^0 \to K^- \pi^+ \pi^- \pi^+$ contamination. Events in which the invariant mass of any of the four $\pi^+ \pi^-$ combinations lies within $0.030\,\mathrm{GeV}/c^2$ of the $K_s^0$ mass are rejected, thereby eliminating contamination by the Cabibbo-allowed $\bar{K}^0 \pi^+ \pi^-$ decay. Requiring the energy of the $4\pi$ system to lie within $0.040\,\mathrm{GeV}$ of the beam energy then results in the beam-constrained mass plot shown in Figure 4.9. Fitting this plot with the signal width ($\sigma = 0.0023\,\mathrm{GeV}/c^2$) predicted by the Monte Carlo and a flat background term, yields $(9^{+4}_{-3})$ signal events. Using the 16% detection efficiency predicted by the Monte Carlo on the basis of flat phase space production, we derive:

$$B(D^0 \to \pi^- \pi^+ \pi^- \pi^+) = (1.47^{+0.61}_{-0.49} \pm 0.19)\%.$$
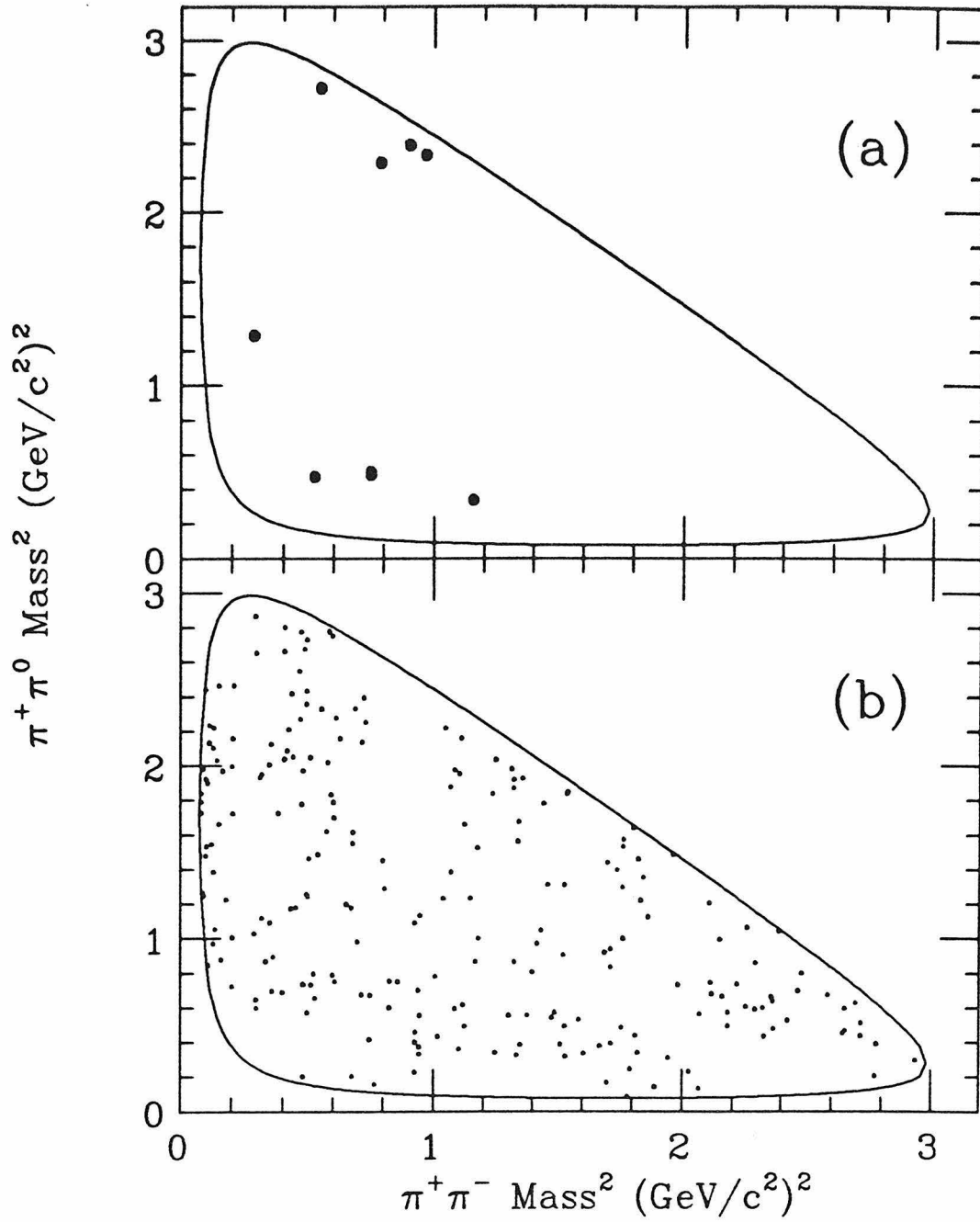
Figure 4.10. Dalitz plot for $D^0 \rightarrow \pi^- \pi^+ \pi^0$ (a) as observed in the data, and (b) from Monte Carlo events generated according to phase space.

Systematic errors in this measurement arise from using a fixed signal width in the mass plot fit (3%), requiring TOF identification of the charged pions (10%), a single event which comes close to the defined $K_s^0$ mass cuts ($\pm 0.5$ event, or 5%), and the $4\pi$ total energy cut (5%).

This technique, using only particles in the recoil spectrum from reconstructed D decays to identify decays in modes with large backgrounds, has been employed in a search for several other decay channels. One event is seen in the $\pi^- \pi^+ \pi^+$ final state at the $D^+$ mass with no background. The measurement which could be derived from this observation is consistent with, but much inferior in precision to the measurement presented in section 4.3 . In the $\pi^- \pi^+ \pi^+ \pi^0$ and $\pi^+ \pi^- \pi^+ \pi^- \pi^+$ final states, no events are seen after $\pi^+ \pi^-$ mass cuts exclude contamination from Cabibbo-favored decays in modes with $K^0$'s. No attempt has been made to derive upper limits based on these observations.

## 4.6 SUMMARY

In this chapter, results have been variously quoted as ratios of decay widths, $\sigma \cdot B$ measurements, and branching fractions. The justification for preferring the $\sigma \cdot B$ measurements to branching ratios in the previous chapter is that the uncertainty in $D^+$ and $D^0$ cross-sections introduces large errors into otherwise well-measured decays. Because of the larger statistical errors in the Cabibbo-suppressed measurements (due to the smaller numbers of reconstructed events), that reasoning is less valid here. Therefore, Table 4.1 lists these measurements both in their original form, and as branching ratios.

Table 4.1. Summary of Cabibbo-suppressed measurements.

| Primary Measurement | $B(\%)$ |
|---|---|
| $D^0$ Decays | |
| $\quad \Gamma(D^0 \to K^- K^+)/\Gamma(D^0 \to K^- \pi^+) = 0.122 \pm 0.018 \pm 0.012$ | $0.60 \pm 0.14 \pm 0.09$ |
| $\quad \Gamma(D^0 \to \pi^+ \pi^-)/\Gamma(D^0 \to K^- \pi^+) = 0.033 \pm 0.010 \pm 0.006$ | $0.16 \pm 0.06 \pm 0.03$ |
| $\quad \Gamma(D^0 \to K^0 \bar{K}^0)/\Gamma(D^0 \to K^- \pi^+) < 0.11$ @90% C.L. | $< 0.65$ @90% C.L. |
| | |
| $\quad \sigma_{D^0} \cdot B(D^0 \to K^0 K^- \pi^+ + \bar{K}^0 K^+ \pi^-)_{non-res} < 0.079 \, \text{nb}$ @90% C.L. | $< 2.03$ @90% C.L. |
| $\quad \sigma_{D^0} \cdot B(D^0 \to K^{*0} \bar{K}^0 + \bar{K}^{*0} K^0) < 0.036 \, \text{nb}$ C.L. | $< 0.92$ @90% C.L. |
| $\quad \sigma_{D^0} \cdot B(D^0 \to K^{*-} K^+ + K^{*+} K^-) = 0.050 \pm 0.023 \pm 0.010 \, \text{nb}$ | $1.04 \pm 0.52 \pm 0.25$ |
| | |
| $\quad B(D^0 \to \pi^- \pi^+ \pi^0) = (1.11^{+0.43}_{-0.35} \pm 0.18)\%$ | $1.11^{+0.43}_{-0.35} \pm 0.18$ |
| $\quad B(D^0 \to \pi^- \pi^+ \pi^- \pi^+) = (1.47^{+0.61}_{-0.49} \pm 0.19)\%$ | $1.47^{+0.61}_{-0.49} \pm 0.19$ |
| $D^+$ Decays | |
| $\quad \Gamma(D^+ \to \bar{K}^0 K^+)/\Gamma(D^+ \to \bar{K}^0 \pi^+) = 0.317 \pm 0.086 \pm 0.048$ | $0.92 \pm 0.31 \pm 0.19$ |
| $\quad \Gamma(D^+ \to \pi^- \pi^+ \pi^+)/\Gamma(D^+ \to K^- \pi^+ \pi^+) = 0.042 \pm 0.016 \pm 0.010$ | $0.38 \pm 0.16 \pm 0.10$ |
| $\quad \Gamma(D^+ \to K^- K^+ \pi^+_{non-res})/\Gamma(D^+ \to K^- \pi^+ \pi^+) = 0.059 \pm 0.026 \pm 0.009$ | $0.54 \pm 0.25 \pm 0.10$ |
| $\quad \Gamma(D^+ \to \phi \pi^+)/\Gamma(D^+ \to K^- \pi^+ \pi^+) = 0.084 \pm 0.021 \pm 0.011$ | $0.76 \pm 0.23 \pm 0.13$ |
| $\quad \Gamma(D^+ \to \bar{K}^{*0} K^+)/\Gamma(D^+ \to K^- \pi^+ \pi^+) = 0.048 \pm 0.021 \pm 0.011$ | $0.44 \pm 0.21 \pm 0.11$ |
| | |
| $\quad B(D^+ \to \pi^0 \pi^+) < 0.53\%$ @90% C.L. | $< 0.53\%$ @90% C.L. |

## 5.  Measurements of $D^+$ and $D^0$ Semileptonic Branching Ratios

### 5.1  INTRODUCTION

The inequality of $D^+$ and $D^0$ semileptonic branching ratios observed by Mark II[22] and DELCO[23] may arise from two sources. The semileptonic decay rates themselves can only differ at a Cabibbo-suppressed level[24], because the Cabibbo-allowed semileptonic decay rates are related by isospin. A possible source of different semileptonic rates would be a large enhancement of the Cabibbo-suppressed $D^+$ annihilation diagram ($c\bar{d} \to W^+ \to e^+\nu_e + \text{hadrons}$), but estimates of this effect place it at the 10% level or below[21]. Larger differences than this between $D^+$ and $D^0$ semileptonic branching ratios must thus be ascribed to different total hadronic decay rates. This, in turn, requires modification of the light quark spectator picture of charm decay.

The DELCO measurements:

$$B(D^+ \to e^+ + X) = (22.0^{+4.4}_{-2.2})\%$$
$$B(D^0 \to e^+ + X) < 4.0\% \text{ at } 90\% \text{ confidence level,}$$

however, yield a lower limit on the ratio of $D^+$ to $D^0$ lifetimes, $\tau^+/\tau^0 > 4.3$ at 95% confidence level, which is in serious conflict with the world average of direct lifetime measurements[26]: $\tau^+/\tau^0 = 2.1 \pm 0.3 \pm 0.3$. On the other hand, the Mark II measurements:

$$B(D^+ \to e^+ + X) = (16.8 \pm 6.4)\%$$
$$B(D^0 \to e^+ + X) = (5.5 \pm 3.7)\%$$

yield a lifetime ratio, $\tau^+/\tau^0 = 3.1^{+4.6}_{-1.4}$, which is of fairly low statistical significance. More precise measurements, particularly of the $D^0$ semileptonic branching ratio, are obviously necessary[59].

### 5.2  ELECTRON IDENTIFICATION AND CORRECTIONS

The basis for this study is a sample of D mesons which are reconstructed in hadronic decay modes. The charm of the hadronically decaying D mesons are

determined by their total charge in $D^+$ decay, and by the kaon charge in $D^0$ decay (assuming a negligible amount of $D^0 \bar{D}^0$ mixing and doubly Cabibbo-suppressed hadronic decays). Semileptonic decays are then identified by the observation of direct electrons among the decay products of the recoil D meson.

Three $D^0$ decay channels ($K^- \pi^+$, $K^- \pi^+ \pi^0$, and $K^- \pi^+ \pi^- \pi^+$) and three $D^+$ decay channels ($\bar{K}^0 \pi^+$, $K^- \pi^+ \pi^+$, and $\bar{K}^0 \pi^+ \pi^- \pi^+$) are chosen for this analysis because of their large signals on modest backgrounds. The reconstruction of these decays follows the procedure described in chapter 3, except that no fiducial cuts are imposed on charged tracks or photons, in order to maximize the number of reconstructed decays. In the $K^- \pi^+ \pi^0$ decay mode, a stricter cut of $\chi^2 < 3$ is imposed to reduce background, and multiple combinations in a single event due to photon interchange are not allowed; only the combination of photons with the best $\chi^2$ is retained. This is done because photons of very low energy do not significantly affect the measured decay mass, and may introduce unwanted correlation between the masses of different combinations. Each mass plot contains a signal region centered on the D mass and a control region between 1.820 and 1.856 GeV/c$^2$. The control region is used in the subsequent analysis as a representation of the background events under the signal peaks. The number of background events under each signal is determined by a fit to the mass plot. The $D^0$ signal region contains 4541 events, of which $(1106 \pm 34)$ are background. The $D^+$ signal region contains 2062 events, of which $(333 \pm 20)$ are background. Here, we are only interested in counting the number of signal events, *not* in measuring the expected production rate. The situation is analogous to that of a coin-flipping experiment, in which the number of reconstructed hadronic decays is like the number of coin flips, and the observation of an electron in the recoil is like a 'success.' Thus, the number of reconstructed hadronic decays contains no intrinsic $\sqrt{N}$ error, but is assigned an error only because of fluctuation in the number of background events.

Candidate electron tracks recoiling from these reconstructed D mesons are

required to lie within $|\cos\theta| < 0.77$. Within this fiducial region charged kaons can and must be rejected, as their charge is preferentially opposite to expected electron charge, and they are often misclassified as electrons because of large energy deposition in the shower counter. Tracks which have momentum below $0.150\,\text{GeV}/\text{c}$, for which the detection efficiency is low and not easily modeled, are also rejected. Remaining tracks must originate near the event's primary vertex within $0.01\,\text{m}$ perpendicular and $0.15\,\text{m}$ parallel to the beam axis, and deposit energy in the barrel calorimeter. Most of the electrons from photon conversions and Dalitz (i.e., $\pi^0 \to e^+ e^- \gamma$) decays are then removed by requiring candidate electron tracks to have opening angles greater than $8°$ with any other oppositely charged track in the event at their crossing point in X-Y projection.

Electrons are separated from charged pions by a sequence of cuts which depend on track momentum, and use the TOF, shower energy deposition, and both longitudinal and transverse shower development information. Pure samples of pions and electrons from $\psi(3095)$ data serve as input to the mathematical technique known as recursive partitioning[60] which is used to determine the optimal set of cuts for electron/pion separation in each momentum bin. The eight variables which are used in the separation are:

- Shower energy.
- Energy-weighted shower depth:

$$\sum_{i=1}^{12} E_i \cdot i \, .$$

- RMS shower width.
- A $[\chi^2]_\pi$ variable, which measures the deviation of the shower profile from that of a 'typical' pion shower.
- Shower energy divided by track momentum, $E/P$.
- TOF electron weight.
- Energy deposition in layers $4 - 6$ of the shower counter.

- Energy deposition in layers $7-9$ of the shower counter.

For tracks which have momenta below $0.3\,\text{GeV/c}$, only TOF information is actually used. Tracks having higher momenta are classified primarily using shower counter information, although TOF information is still useful up to about $0.4\,\text{GeV/c}$. The resulting misidentification rates, shown in Figure 5.1, are then determined using pure and independent samples from the $\psi''$ data set: pions from $K_s^0$ decays and electrons from radiative Bhabha events.

The expected charge of a recoil electron is uniquely determined by the charm of the reconstructed hadronic D decay. Corrections for charge-symmetric sources of electron candidates such as misidentification of equal numbers of positively and negatively charged pions, photon conversions, and Dalitz decays not removed by the opening angle cut are thus made by subtracting the number of wrong-sign electron candidates from the number of right-sign candidates. A right-sign candidate electron is one with the expected charge, given the charm of the hadronic decay. The major source of background to the electron signal which is *not* charge-symmetric is misidentification of an excess of right-sign pions over wrong-sign pions. This amounts to 20% of the apparent number of right-sign electrons for $D^+$ and 14% of the apparent right-sign electrons for $D^0$. To correct for this source of background, the measured electron and pion misidentification rates are used to unfold the true number of electrons from the observed populations of electrons and pions of each sign in each momentum bin. Explicitly, the numbers of observed electrons $(N_e^o)_i$ and pions $(N_\pi^o)_i$ in a single momentum bin are given by the following equations:

$$(N_e^o)_i = (N_e)_i P_{e\to e} + (N_\pi)_i P_{\pi\to e}$$
$$(N_\pi^o)_i = (N_e)_i P_{e\to \pi} + (N_\pi)_i P_{\pi\to \pi},$$

where $(N_e)_i$ and $(N_\pi)_i$ are the true populations of electrons and pions in that momentum bin, and $P_{e\to e}$, $P_{\pi\to e}$, $P_{e\to \pi}$, and $P_{\pi\to \pi}$ are the known misidentification rates. After inverting the $2 \times 2$ misidentification matrices (one
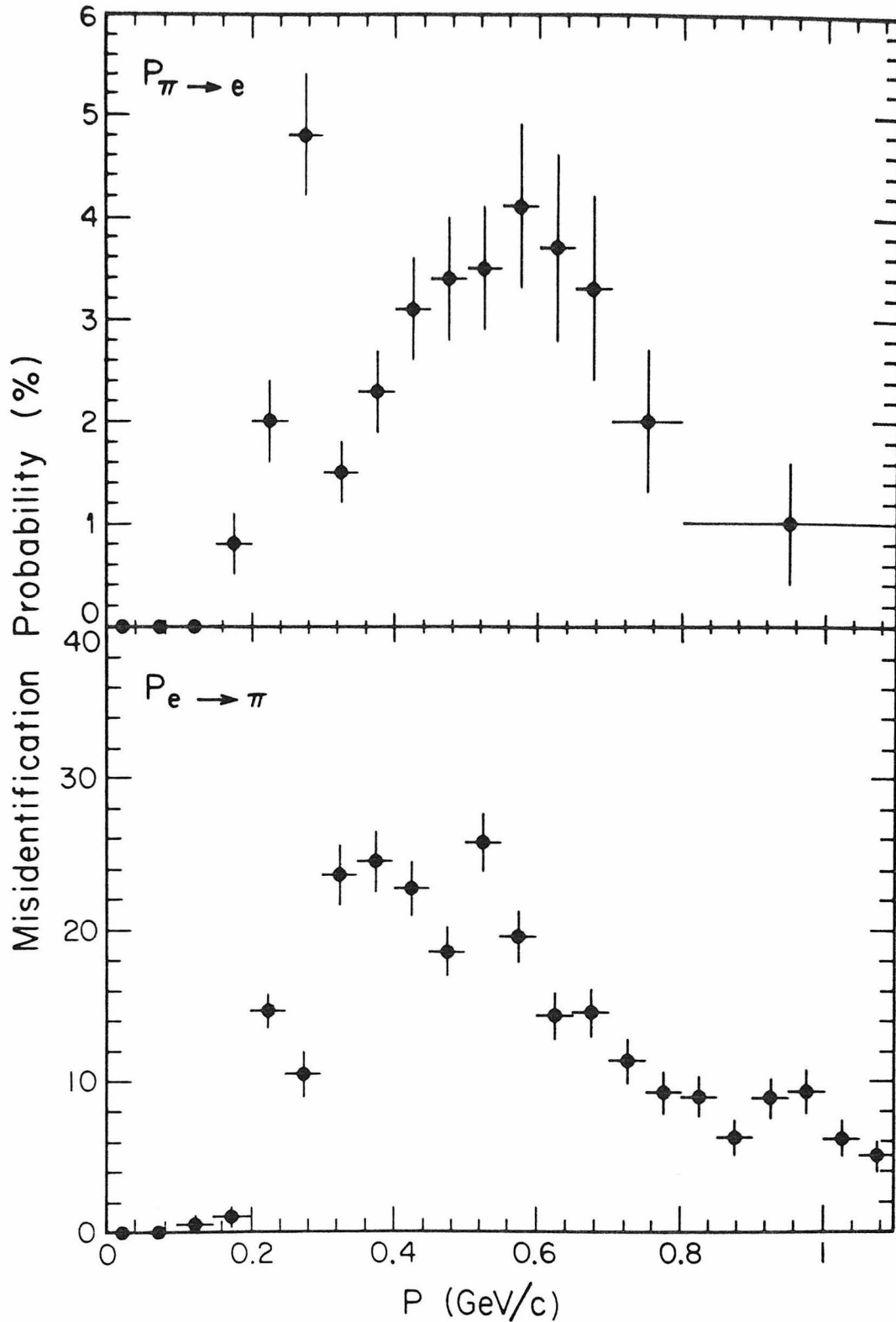
Figure 5.1. Misidentification probabilities for pions and electrons. For $p < 0.3\,\mathrm{GeV/c}$, only TOF is used for particle identification. For $p > 0.3\,\mathrm{GeV/c}$, both TOF and shower counter information are used.

for each momentum bin) and multiplying by the observed numbers of electrons and pions, the total numbers of produced electrons and pions are determined:

$$N_e(tot) = \sum_i (N_e)_i$$

$$N_\pi(tot) = \sum_i (N_\pi)_i \, .$$

The observed populations of right-sign pions include contributions from semileptonic D decays to muons. The number of muons is estimated from the derived semileptonic branching ratios to electrons, and is then subtracted from the number of right-sign pions before misidentification corrections, since muons (as observed in cosmic ray events) are not misidentified as electrons. To correct for background events in the D signal region, the number of unfolded electrons observed in the recoil from particle combinations in the control region is scaled by the relative number of background events in control and signal regions, and is then subtracted from the number of remaining signal region electrons. No dependence on the choice of the control region is observed. A small correction of $(1.8 \pm 0.9)$ electrons is applied to account for TOF misidentification of both kaon and pion in the $D^0 \to K^- \pi^+$ decay mode. Finally, the number of electrons is increased by $(0.3 \pm 0.2)$ and $(0.8 \pm 0.4)$ in the $D^+$ and $D^0$ samples, respectively, to account for $K_{e3}$ decays. Table 5.1 summarizes these corrections.

The probability for an electron to satisfy the track requirements imposed before pion-electron classification depends on momentum and, slightly, on the type of hadronic decay. This efficiency is determined as a function of electron momentum by Monte Carlo simulation of $D\bar{D}$ events, in which one D decays into $Ke\nu$ or $K^*e\nu$ and the recoil $\bar{D}$ decays into a hadronic channel. The form factors in $Ke\nu$ and $K^*e\nu$ decay are assumed to have a $q^2$ dependence given by simple poles[52]. The resulting electron angular distributions are found to be isotropic in the laboratory frame. A typical electron efficiency curve is shown in Figure 5.2 for events in which one $D^0$ decays hadronically into $K^- \pi^+$ and the

Table 5.1. Intermediate results of the electron analysis.

| | $D^+$ | $D^0$ |
|---|---|---|
| Signal events | $1729 \pm 20$ | $3435 \pm 39$ |
| Signal electrons: | | |
|     Right-sign | $177.0 \pm 13.3$ | $193.0 \pm 13.9$ |
|     Wrong-sign | $14.0 \pm 3.7$ | $57.0 \pm 7.5$ |
|     Net | $163.0 \pm 13.8$ | $136.0 \pm 15.8$ |
|     Unfolded | $160.7 \pm 17.4$ | $141.8 \pm 19.9$ |
| Unfolded control electrons | $2.5 \pm 2.9$ | $5.2 \pm 4.5$ |
| Net electrons | $158.2 \pm 17.6$ | $136.6 \pm 20.4$ |
| Corrections: | | |
|     Classification efficiency | $226.1 \pm 25.1$ | $195.7 \pm 29.2$ |
|     $K_{e3}$ decays | $226.4 \pm 25.1$ | $196.5 \pm 29.2$ |
|     $K^-\pi^+$ interchange | $226.4 \pm 25.1$ | $198.3 \pm 29.2$ |
|     Solid angle | $294.0 \pm 32.6$ | $257.5 \pm 37.9$ |
| Branching fraction (%) | $17.0 \pm 1.9$ | $7.5 \pm 1.1$ |

recoil $\bar{D}^0$ decays to $K^+ e^- \bar{\nu}_e$. The efficiency is low for electrons having momenta below $0.150\,\mathrm{GeV/c}$ because the electrons either curl up in the drift chamber or lose energy and stop before reaching the shower counter. A slight decrease in efficiency can also be seen at higher momenta ($> 0.8\,\mathrm{GeV/c}$) due to the reduced ability of the TOF counters to reject charged kaons. The efficiency also depends on total charged multiplicity, dropping approximately $-3.5\%$ per track. For the mix of hadronic decay channels used in this analysis, the mean charged multiplicity is about five for both $D^+$ and $D^0$, leading to an average efficiency of 70% for electrons from either $D^+$ or $D^0$ decay. After these efficiency corrections, the final electron momentum spectra are shown in Figure 5.3 along with the shape of spectra expected for $Ke\nu$ and $K^*e\nu$ decays[52]. Large errors on the unused data points below $0.150\,\mathrm{GeV/c}$ reflect their low and poorly determined efficiencies.

## 5.3 RESULTS

The numbers of electrons seen recoiling against the detected $D^+$ and $D^0$
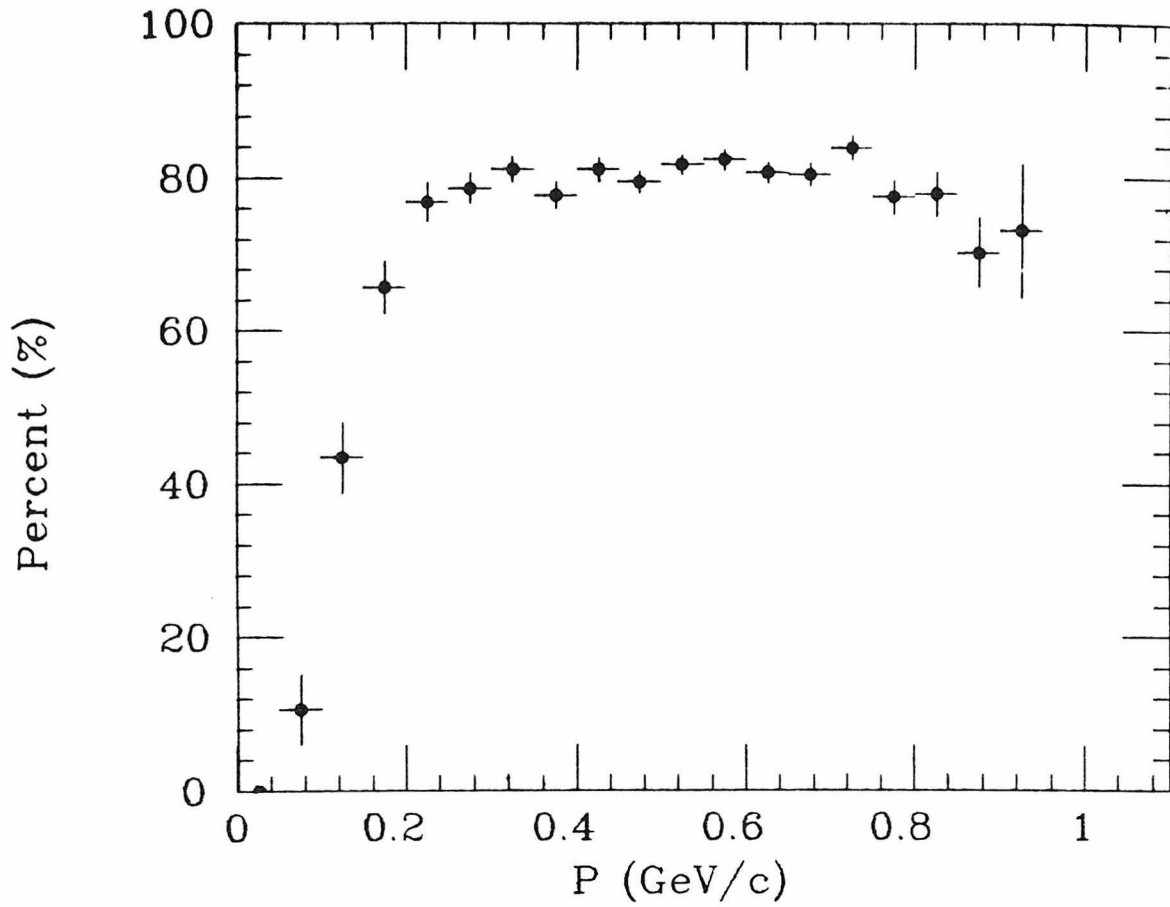
Figure 5.2. Efficiency for electrons to pass track requirements imposed before electron-pion classification, as a function of momentum in $K^+ e^- \bar{\nu}_e$ versus $K^- \pi^+$ Monte Carlo events.
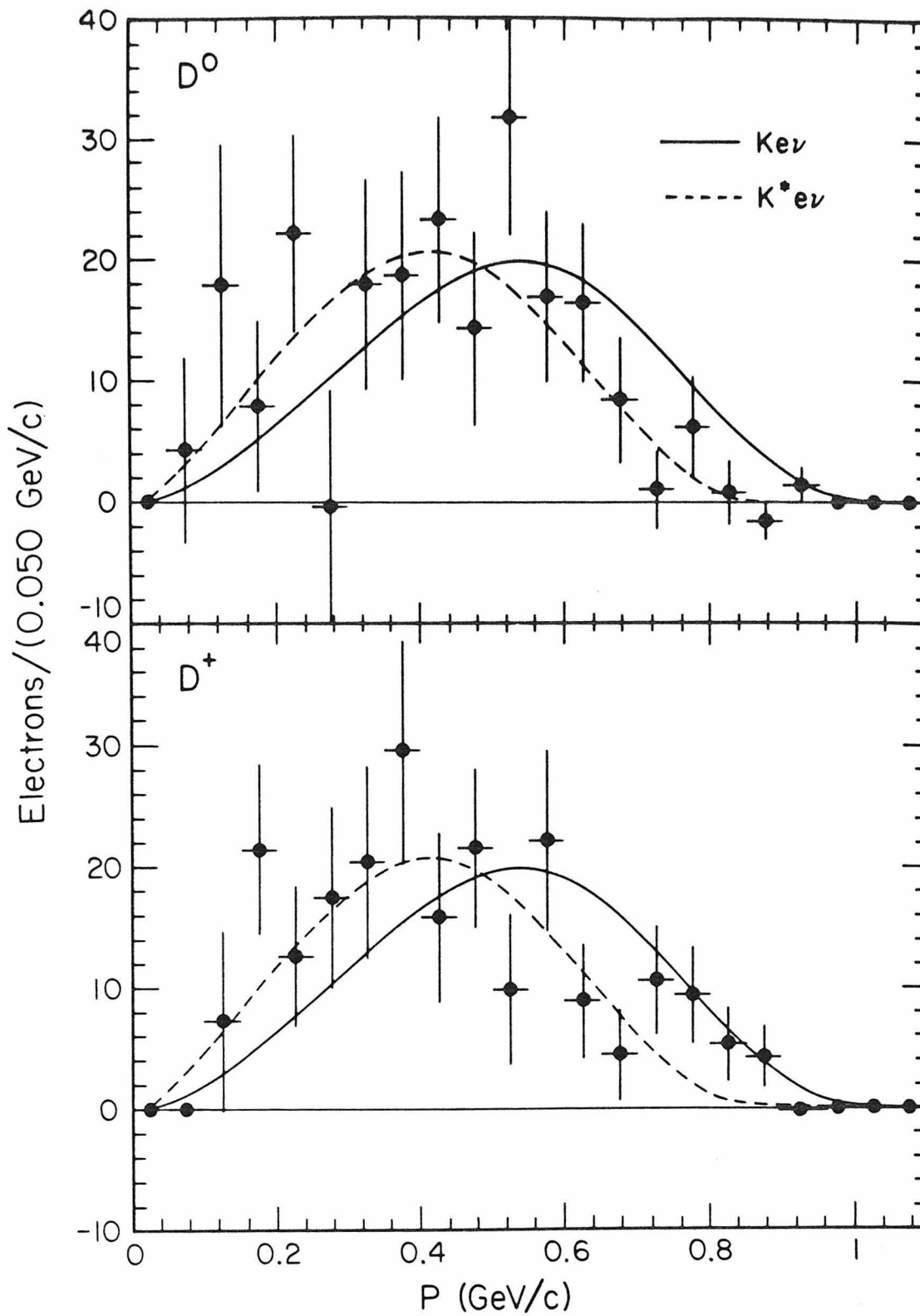
Figure 5.3. $D^0$ and $D^+$ electron spectra. The curves represent the shape of spectra expected from $Ke\nu$ and $K^*e\nu$ decays.

lead to the branching fractions

$$B(D^+ \to e^+ X) = (17.0 \pm 1.9 \pm 0.7)\%,$$

$$B(D^0 \to e^+ X) = (7.5 \pm 1.1 \pm 0.4)\%,$$

and thus to the ratio:

$$\frac{B(D^+ \to e^+ X)}{B(D^0 \to e^+ X)} = 2.3^{+0.5}_{-0.4} \pm 0.1.$$

Contributions to the systematic errors arise from several sources, and are estimated in the following manner.

- Variation of the pion misidentification rate by 25% changes the semileptonic branching ratios by 1.8% for $D^0$, and by 2.3% for $D^+$ (0.5% for their ratio).

- The electron efficiency (before classification) is assigned a systematic error of 3%, estimated from the observed variation of efficiency with charged multiplicity ($-3.5\%$ per additional charged particle) observed in the Monte Carlo. By extrapolating this variation to the case of two charged tracks, a comparison can be made between the expected electron efficiency and the efficiency actually observed in radiative Bhabha events. No significant discrepancy is observed. Because the charged multiplicities in $D^+$ and $D^0$ events are very similar, this source of systematic error cancels in the ratio of semileptonic branching fractions.

- Sensitivity to the $Ke\nu/K^*e\nu$ fractions is largely because of the variation in the fraction of the electron spectrum below the $0.150\,\mathrm{GeV/c}$ momentum cutoff. Varying these fractions according to the result of a DELCO fit to the inclusive electron spectrum[61] at the $\psi''$, which can be quoted as $(63 \pm 16)\%$ $Ke\nu$, changes the $D^0$ and $D^+$ semileptonic branching fractions by 0.8% and 1.0%, respectively, and produces an insignificant change in their ratio.

- The muons in the electron/pion samples from 'semi-muonic' decay, which are all right-sign, have a much lower misidentification rate than pions at momenta where the identification is made using shower counter variables, and represent a 2.7% correction to both $D^+$ and $D^0$ branching fractions. Because cosmic rays must have appreciable energy to penetrate the magnet iron, the number of low-momentum muons from cosmic rays is insufficient at lower momenta ($p < 0.4\,\mathrm{GeV/c}$) to reliably determine their misidentification rate. Therefore, 50% of the 2.7% correction, or 1.3%, is added to the systematic error in both $D^+$ and $D^0$ branching fractions, although not to their ratio.

Combination of these uncertainties in quadrature yields 4.1% and 4.9% systematic errors for the $D^+$ and $D^0$ branching fractions, respectively, and a 3.0% error for their ratio.

The average D semileptonic branching ratio at the $\psi''$ can then be derived as:

$$B(D \to e^+ X) = (11.7 \pm 1.0 \pm 0.5)\%\,,$$

assuming that 56% of the charm production is $D^0 \bar{D}^0$ by division of phase space[41]. This value is consistent with the value of $(10.0 \pm 3.2)\%$ derived using the same technique by Mark II, but significantly higher than previous DELCO[61] and LGW[62] measurements of $(8.0 \pm 1.5)\%$ and $(7.2 \pm 2.8)\%$, respectively. It should be noted, however, that this average represents an absolute measurement, while the DELCO and LGW results rely on normalization of their electron signals using the measured cross-sections for $\psi''$ production. This measurement, like the absolute measurements of $K^-\pi^+$ and $K^-\pi^+\pi^+$ branching ratios presented in section 3.7, indicates that the $D\bar{D}$ cross-section at the $\psi''$ may have been overestimated in the past.

The likelihood function for the ratio of semileptonic branching fractions is shown in Figure 5.4. This measurement is in serious disagreement with the ratio

of semileptonic branching fractions measured by DELCO[23]. Interpreted as the ratio of $D^+$ and $D^0$ lifetimes, however, this ratio agrees with the world average of direct lifetime determinations, and excludes the possibility of equal lifetimes at 4.3 standard deviations.
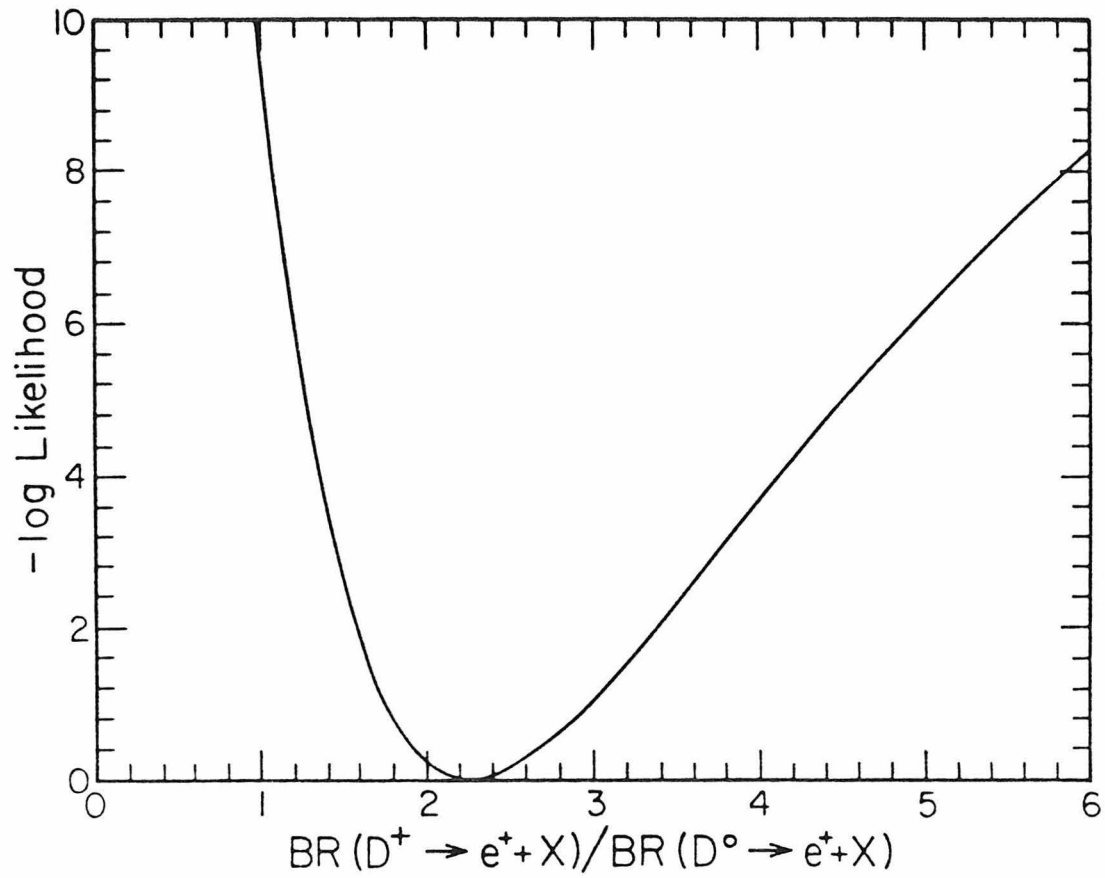
Figure 5.4. Negative log likelihood function for $B(D^+ \to e^+ X)/B(D^0 \to e^+ X)$.

## 6. Conclusions

### 6.1 EXPERIMENTAL

The Mark III data presented in this thesis considerably extends and refines our knowledge of D meson decays. When the branching ratios to exclusive Cabibbo-allowed and suppressed channels are added to the inclusive semileptonic branching ratios (assuming equality of the decay rates to electrons and muons), the total fractions of $D^0$ and $D^+$ decays accounted for are approximately 80% in either case, although these values depend strongly on the production cross-sections $\sigma_{D^0}$ and $\sigma_{D^+}$. In addition, reconstruction of exclusive semileptonic decays in the same Mark III data sample (presented elsewhere[63]) shows that the semileptonic decays are dominated by $Ke\nu$ and $K^*e\nu$ channels, as expected. Thus, a large portion of the total D meson decay widths have been observed in exclusive final states. Decays which have not been accounted for in our data can be presumed to be of high multiplicity, contain more than one $\pi^0$, or contain particles which are relatively difficult to reconstruct, such as $\eta$, $\eta'$, and $\omega$.

The absolute measurements of $K^-\pi^+$ and $K^-\pi^+\pi^+$ branching ratios, as well as the average D semileptonic branching ratio at the $\psi''$, indicate that the $D\bar{D}$ production cross-section at the $\psi''$ peak may have been over-estimated by the Mark I[64] and Mark II[65] experiments, which measured $(10.3 \pm 2.5)\,\mathrm{nb}$ and $(9.3 \pm 1.4)\,\mathrm{nb}$, respectively, although DELCO[66] and Crystal Ball[67] peak cross-sections of $\approx 6\,\mathrm{nb}$ and $(6.7 \pm 0.9)\,\mathrm{nb}$, respectively, are consistent. One possible, although by no means certain, way to explain the discrepancy with Mark I and Mark II cross-sections is to claim that $D\bar{D}$ events more easily pass cuts imposed to select hadrons than continuum events. Efficiency corrections can then make the apparent $\psi''$ cross-section larger than its true cross-section. For instance, $\psi'' \to D^+D^-$ events must contain at least two charged particles, and $(99.1 \pm 0.5)\%$ of $\psi'' \to D^0\bar{D}^0$ events contain at least two charged particles (calculated by assuming that the $D^0$ and $\bar{D}^0$ decay independently[68], and using the Mark II measurement[69] of $(9.6 \pm 2.5)\%$ for the inclusive all-neutral fraction of

Table 6.1. Comparison of $\sigma \cdot B$ measurements between LGW (Mark I),
Mark II, and Mark III.

| Decay Mode | LGW $\sigma \cdot B$ (nb) $\sqrt{s} = 3.774\,\text{GeV}$ | Mark II $\sigma \cdot B$ (nb) $\sqrt{s} = 3.771\,\text{GeV}$ | Mark III $\sigma \cdot B$ (nb) $\sqrt{s} = 3.766\,\text{GeV}$ (avg.) |
|---|---|---|---|
| $D^0 \rightarrow$ | | | |
| $K^-\pi^+$ | $0.25 \pm 0.05$ | $0.24 \pm 0.02$ | $0.237 \pm 0.009 \pm 0.013$ |
| $\bar{K}^0\pi^0$ | | $0.18 \pm 0.08$ | $0.108 \pm 0.020 \pm 0.010$ |
| $K^-\pi^+\pi^0$ | $1.40 \pm 0.60$ | $0.68 \pm 0.23$ | $0.978 \pm 0.065 \pm 0.137$ |
| $\bar{K}^0\pi^+\pi^-$ | $0.46 \pm 0.12$ | $0.30 \pm 0.08$ | $0.372 \pm 0.030 \pm 0.031$ |
| $K^-\pi^+\pi^-\pi^+$ | $0.36 \pm 0.10$ | $0.68 \pm 0.11$ | $0.566 \pm 0.027 \pm 0.061$ |
| $D^+ \rightarrow$ | | | |
| $\bar{K}^0\pi^+$ | $0.14 \pm 0.05$ | $0.14 \pm 0.03$ | $0.126 \pm 0.012 \pm 0.009$ |
| $K^-\pi^+\pi^+$ | $0.36 \pm 0.06$ | $0.38 \pm 0.05$ | $0.399 \pm 0.017 \pm 0.028$ |
| $\bar{K}^0\pi^+\pi^0$ | | $0.78 \pm 0.48$ | $0.714 \pm 0.142 \pm 0.100$ |
| $\bar{K}^0\pi^+\pi^-\pi^+$ | | $0.51 \pm 0.18$ | $0.305 \pm 0.031 \pm 0.030$ |

$D^0$ decays). Moreover, the hadron detection efficiencies in the earlier experiments were quite low, e.g., 47% in the Mark I[70] at a center-of-mass energy of 3.77 GeV. A more exotic explanation, that a significant fraction of $\psi''$ decays are to states other than $D\bar{D}$ pairs, is contradicted, in part, by an unsuccessful search for radiative transitions from the $\psi''$ by Crystal Ball[71].

A comparison between the Mark III measurements of $\sigma \cdot B$ and those of the earlier LGW[42]and Mark II[22]experiments for previously observed D meson decay channels is shown in Table 6.1 . Although the three experiments took their data at different beam energies, and thus may have different D meson production cross-sections, the energies are all close enough to the peak of the $\psi''$ resonance that the differences should be small ($< 10\%$). This comparison reflects both on the quality of the Monte Carlo simulation in determining detection efficiencies, and on the measurement of total integrated luminosity. The Mark III results are seen to agree well with previous results.

## 6.2 CHARM DECAY MIXING MATRIX ELEMENTS

The clustering of the ratios presented in chapter 4 between decay rates to Cabibbo-suppressed and Cabibbo-allowed final states at a level of about 5% tends to support the GIM mechanism as a reasonable approximation in D meson decays. This is merely a qualitative statement, however. For a more quantitative comparison, SU(3) symmetry can be used to relate Cabibbo-allowed and Cabibbo-suppressed rates, particularly in two-body channels. Within the GIM picture, SU(3) leads to the following relations[37]:

$$\frac{\Gamma(D^0 \to K^- K^+)}{\Gamma(D^0 \to K^- \pi^+)} = \frac{\Gamma(D^0 \to \pi^- \pi^+)}{\Gamma(D^0 \to K^- \pi^+)} = \left| \frac{V_{cd}}{V_{cs}} \right|^2 \approx 0.05$$

and

$$\frac{B(D^+ \to \pi^0 \pi^+)}{B(D^+ \to \bar{K}^0 \pi^+)} = \frac{1}{2} \times \left| \frac{V_{cd}}{V_{cs}} \right|^2 \approx 0.025 \,.$$

Mark II measured the rates[72] for $D^0$ decay to $K^- K^+$ and $\pi^- \pi^+$ as $0.113 \pm 0.030$ and $0.033 \pm 0.015$ of the rate to $K^- \pi^+$, respectively. Possible explanations for the discrepancy between these measurements and the SU(3) predictions have included KM charm decay mixing angles which are different from their four-quark values[73], penguin diagrams[74,75], helicity suppression[74], final state interactions[74], and possibly to a statistical fluctuation in the Mark II data[13]. The contribution of penguin diagrams to this inequality has been shown to be small in a four-quark model[28], but could be significant if the KM mixing angles differ from their four-quark model values[74]. Recent measurements of 'long' B lifetimes[9] and charm production in neutrino interactions[10] tend to rule out such an explanation, however. The new Mark III measurements:

$$\frac{\Gamma(D^0 \to K^- K^+)}{\Gamma(D^0 \to K^- \pi^+)} = 0.122 \pm 0.018 \pm 0.012$$

$$\frac{\Gamma(D^0 \to \pi^- \pi^+)}{\Gamma(D^0 \to K^- \pi^+)} = 0.033 \pm 0.010 \pm 0.006 \,,$$

confirm the inequality of $K^- K^+$ and $\pi^- \pi^+$ decay rates and rule out the hypothesis of a large statistical fluctuation in the Mark II data. The remaining hypotheses, such as final state interactions and helicity suppression[74], invoke SU(3) breaking as the source of the $K^- K^+ / \pi^- \pi^+$ difference. The above SU(3) prediction of the $D^+$ decay rate to $\pi^0 \pi^+$ relative to $\bar{K}^0 \pi^+$ may be a more reliable way to look at the mixing angles[76], since the final states are exotic $I = 2$ and $I = 3/2$ combinations, respectively, and thus free of the final state interactions which may contribute to SU(3) breaking. The limit:

$$\frac{\Gamma(D^+ \to \pi^0 \pi^+)}{\Gamma(D^+ \to \bar{K}^0 \pi^+)} < 0.18 \text{ at } 90\% \text{ confidence level}$$

is, however, much higher than the prediction of 0.025 for this ratio, although consistent. Another pair of SU(3) relations related to the mixing angles are[37]:

$$\frac{\Gamma(D^0 \to K^{*-} K^+)}{\Gamma(D^0 \to K^{*-} \pi^+)} = \frac{\Gamma(D^0 \to K^{*+} K^-)}{\Gamma(D^0 \to K^- \rho^+)} = \left| \frac{V_{cd}}{V_{cs}} \right|^2 \approx 0.05 \,.$$

We cannot distinguish $K^{*-} K^+$ from $K^{*+} K^-$ decays, but can sum the observed signals in both numerators and denominators of these relations, to obtain:

$$\frac{\Gamma(D^0 \to K^{*-} K^+ + K^{*+} K^-)}{\Gamma(D^0 \to K^{*-} \pi^+ + K^- \rho^+)} = 0.05 \pm 0.03 \,.$$

This measurement is consistent with the GIM expectations, and does not show the same level of two-kaon enhancement observed in the $D^0 \to K^- K^+$ decay. Thus, our measurements, although not strictly related to the mixing matrix elements in the face of SU(3)-violating effects, are consistent with the GIM picture of charm decay matrix elements $V_{cs}$ and $V_{cd}$.

### 6.3 THE $D^+ / D^0$ LIFETIME DIFFERENCE

The ratio of $D^+$ to $D^0$ semileptonic branching fractions:

$$B_e^+ / B_e^0 = 2.3^{+0.5}_{-0.4} \pm 0.1$$

presented here is in good agreement with the present world average[26] of the ratio of $D^+$ to $D^0$ lifetimes:

$$\frac{\tau^+}{\tau^0} = 2.1 \pm 0.3 \pm 0.3$$

as determined by decay length experiments. The interpretation of these ratios as equal (within about 10%) is supported by preliminary measurements of D branching fractions into exclusive semileptonic channels[63], showing that semileptonic decays to electrons are dominated by the Cabibbo-allowed $Ke\nu$ and $K^*e\nu$ channels. The situation is therefore much different than in 1981, when the ratio of lifetimes appeared closer to 10. One implication of the smaller value of this ratio presently observed is that it is more difficult to isolate the possible contributions to the lifetime difference. It is no longer reasonable to speak of W-exchange dominance of $D^0$ decays, for instance, because spectator diagrams are likely to furnish a significant portion of both $D^+$ and $D^0$ decay widths.

The measured semileptonic branching ratios are compared in Figure 6.1 to the expected value:

$$B_e = \frac{1}{2 + 2C_+^2 + C_-^2}$$

from the spectator model (ignoring quark masses) for different values of $(C_-/C_+)$, assuming the relation $C_+^2 C_- = 1$. From this figure, it can be seen that the Mark III measurements are compatible either with a 'normal' $D^+$ hadronic decay rate using the nominal QCD values of $C_-$ and $C_+$ and 'enhanced' $D^0$ decay; or with 'normal' $D^0$ decay using $(C_-/C_+) \approx 5 - 10$ and 'suppressed' $D^+$ decay. The enhancement or suppression mechanism(s) increases the relative hadronic decay rate of the $D^0$ from that of the $D^+$ by about a factor of three. When corrections from the next-to-leading log (NLL) calculation and quark masses are taken into account, QCD predicts semileptonic branching ratios of $(13 - 15)\%$. Thus, from the measured semileptonic branching ratios alone, one suspects that the $D^0$ hadronic decay rate is somewhat enhanced *and* that the $D^+$ rate is slightly suppressed. For more clues as to the source of the lifetime difference, we must

turn to the measurements of specific hadronic decays.

Observation of signals in $\bar{K}^0\phi$, $K^0\bar{K}^0$, or $K^{*0}\bar{K}^0$ ($\bar{K}^{*0}K^0$) would be the most reliable indication[32] of a significant contribution to the $D^0$ decay rate from W-exchange diagrams. The rate for $D^0 \to \bar{K}^0\phi$ should be suppressed by phase space by a factor of about 5 relative to the rates for $D^0 \to \bar{K}^0\rho^0$ or $K^-\rho^+$, so that the limit:

$$B(D^0 \to \bar{K}^0\phi) < 2.4\% \text{ at } 90\% \text{ confidence level}$$

is not particularly stringent, in light of the measurements:

$$B(D^0 \to \bar{K}^0\rho^0) = (1.3 \pm 0.5 \pm 0.3)\%$$
$$B(D^0 \to K^-\rho^+) = (15.1 \pm 3.2 \pm 3.0)\%.$$

The decay $D^0 \to K^0\bar{K}^0$, on the other hand, is not only Cabibbo-suppressed, but is forbidden by exact SU(3) flavor symmetry[37], and so may be additionally suppressed to the extent that SU(3) symmetry is not broken. The upper limit:

$$\frac{\Gamma(D^0 \to K^0\bar{K}^0)}{\Gamma(D^0 \to K^-\pi^+)} < 0.11 \text{ at } 90\% \text{ confidence level}$$

is also not decisive. Perhaps the best limit is supplied for the sum of $D^0$ decay rates to the Cabibbo-suppressed channels $K^{*0}\bar{K}^0$ and $\bar{K}^{*0}K^0$ relative to the sum of the similar, but Cabibbo-allowed decays $D^0 \to K^{*-}\pi^+$ and $K^-\rho^+$:

$$\frac{\Gamma(D^0 \to K^{*0}\bar{K}^0 + \bar{K}^{*0}K^0)}{\Gamma(D^0 \to K^{*-}\pi^+ + K^-\rho^+)} < 0.034 \text{ at } 90\% \text{ confidence level}.$$

If the $\bar{K}^0\phi$, $K^0\bar{K}^0$, or $K^{*0}\bar{K}^0$ ($\bar{K}^{*0}K^0$) decays actually do occur, but at a rate below these limits, a very large data sample may be necessary to see them.

Another way to approach the D lifetime question is to examine the effects which W-exchange diagrams or color clustering may have on isospin or SU(3)
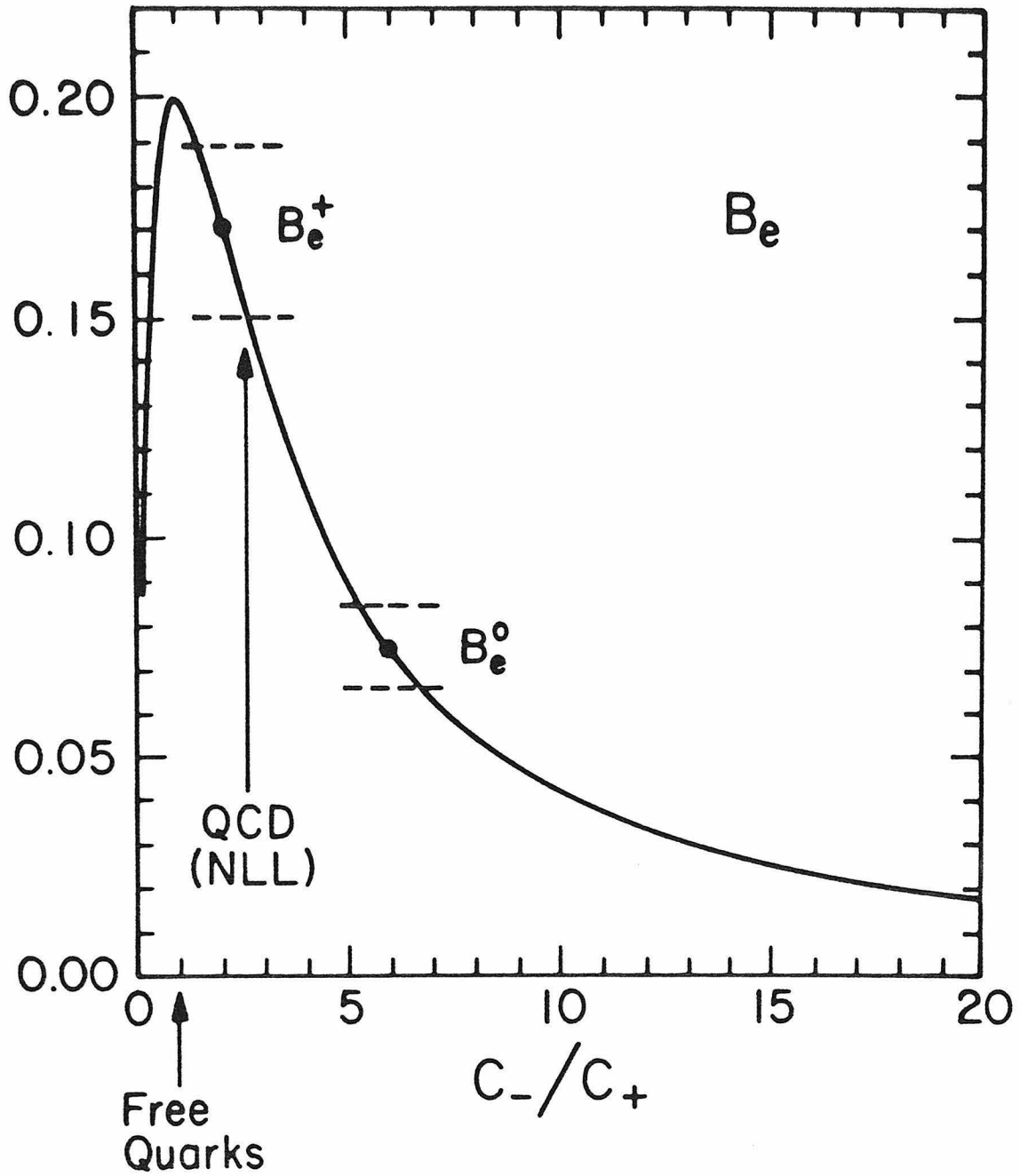
Figure 6.1. Variation of semileptonic branching fractions with $(C_-/C_+)$ in the spectator model, and comparison with the values measured by Mark III.

Table 6.2. SU(3) relations between D and F decay rates to pseudoscalar pairs. $c \equiv \cos\theta_c$, $s \equiv \sin\theta_c$

| $D^0$ | | $D^+$ | | $F^+$ | |
|---|---|---|---|---|---|
| $K^-\pi^+$ | $2\lvert A\rvert^2 c^4$ | $\bar{K}^0\pi^+$ | $2\lvert A+B\rvert^2 c^4$ | $\bar{K}^0 K^+$ | $2\lvert A+B-C\rvert^2 c^4$ |
| $K^- K^+$ | $2\lvert A\rvert^2 c^2 s^2$ | $\bar{K}^0 K^+$ | $2\lvert C\rvert^2 c^2 s^2$ | $\pi^0\pi^+$ | $0$ |
| $\pi^-\pi^+$ | $2\lvert A\rvert^2 c^2 s^2$ | $\pi^0\pi^+$ | $\lvert A+B\rvert^2 c^2 s^2$ | $\eta\pi^+$ | $\frac{4}{3}\lvert C\rvert^2 c^4$ |
| $\bar{K}^0\pi^0$ | $\lvert B\rvert^2 c^4$ | $\eta\pi^+$ | $\frac{1}{3}\lvert 3A+3B-2C\rvert^2 c^2 s^2$ | $\bar{K}^0\pi^+$ | $2\lvert C\rvert^2 c^2 s^2$ |
| $\bar{K}^0\eta$ | $\frac{1}{3}\lvert B\rvert^2 c^4$ | | | $K^+\pi^0$ | $\lvert A+B-C\rvert^2 c^2 s^2$ |
| $K^0\bar{K}^0$ | $0$ | | | $K^+\eta$ | $\frac{1}{3}\lvert 3A+3B-C\rvert^2 c^2 s^2$ |
| $\pi^0\pi^0$ | $\lvert B\rvert^2 c^2 s^2$ | | | | |
| $\eta\eta$ | $\lvert B\rvert^2 c^2 s^2$ | | | | |
| $\pi^0\eta$ | $\frac{2}{3}\lvert B\rvert^2 c^2 s^2$ | | | | |

amplitudes to exclusive final states. The SU(3) relations between various two-body pseudoscalar-pseudoscalar final states (the simplest case) from $D^0$, $D^+$, and $F^+$ decay are presented in Table 6.2 in terms of the three possible reduced matrix elements $A$, $B$, and $C$. The sextet dominance model (large $C_-/C_+$) predicts:

$$A = -B = C,$$

while a large contribution from W-exchange diagrams leads to the relation:

$$A = -B.$$

Because the sextet dominance predictions *contain* those of the W-exchange model, it is impossible to distinguish between the models by this approach. In addition, the more reliable isospin relations only give relations between $A$ and $B$, and so contain no information which can distinguish between these models. However, one can conclude the following:

1. The existence of the $\bar{K}^0\pi^+$ decay at a significant, but not large ($\sim 1/3$) rate compared to $K^-\pi^+$, indicates that the cancellation of $A$ and $B$ amplitudes in this decay predicted by sextet dominance is only partially realized.

2. The Cabibbo-suppressed decay $D^+ \rightarrow \bar{K}^0 K^+$ directly measures the strength of the $C$ amplitude. The ratio of this decay relative to $\bar{K}^0 \pi^+$:

$$\frac{\Gamma(D^+ \rightarrow \bar{K}^0 K^+)}{\Gamma(D^+ \rightarrow \bar{K}^0 \pi^+)} = 0.317 \pm 0.086 \pm 0.048$$

appears anomalously large, but this is because of the partial suppression of the $\bar{K}^0 \pi^+$ decay rate. The $\bar{K}^0 K^+$ decay rate relative to the $D^0 \rightarrow K^- \pi^+$ rate is approximately 8% (using a ratio of lifetimes $\tau^+ / \tau^0 = 2.5$), indicating a value of:

$$\frac{|C|}{|A|} \approx 1.3 \,,$$

which is fairly close to the sextet dominance prediction of equality. In the W-exchange model, $C$ could be anything, and there is no reason to prefer $|C| \approx |A|$.

The above SU(3) relations do not give information about the actual values of $C_+$ and $C_-$ operator coefficients without additional assumptions which can relate the quark currents to final state hadrons. The simplest assumption is to factorize the weak decay matrix elements between color singlet quark-antiquark pairs which are taken to represent the mesonic final states[17]. Factorization is entirely valid in semileptonic decays, where the lepton current is decoupled (ignoring electromagnetic corrections) from the final state mesons. In hadronic decays, factorization can be expected to fail because of interchange of gluons between the final state quarks, and because of the complication of quark hadronization into real particles. As a working assumption, though, factorization leads to a large number of predictions for exclusive decay rates[18]. The previous Mark II measurement[22]:

$$\frac{\Gamma(D^0 \rightarrow \bar{K}^0 \pi^0)}{\Gamma(D^0 \rightarrow K^- \pi^+)} = 0.75 \pm 0.35 \,,$$

is in serious disagreement with the strong suppression of the $\bar{K}^0 \pi^0$ decay rate predicted in the spectator model by this approach. We have confirmed their

result with higher precision, measuring:

$$\frac{\Gamma(D^0 \to \bar{K}^0 \pi^0)}{\Gamma(D^0 \to K^- \pi^+)} = 0.45 \pm 0.08 \pm 0.05 \,.$$

Either large $C_-/C_+$ ratios or contributions from W-exchange diagrams can lead to a ratio of about 1/2, and thus explain this ratio. Another possibility is that the $I = 1/2$ decay amplitude is enhanced by final state interactions[74,77] from, for instance, the scalar resonance $\kappa(1350)$. A large phase shift in the $I = 1/2$ channel could even have made the $\bar{K}^0 \pi^0$ rate larger than the $K^- \pi^+$ rate. (Final state interactions may be less of a problem in B meson decays, or even kaon decays, which are far above and below the resonance region, respectively[12].) The factorization hypothesis is more likely to work in the exotic $I = 3/2$ two-body final states from $D^+$ decay, which are free of final state interactions. An especially good test is the $D^+ \to \bar{K}^0 \pi^+$ decay, factorized as:

$$\langle \bar{K}^0 \pi^+ | H^{eff} | D^+ \rangle = \frac{4C_+}{3} V_{cs} V_{ud}^* \cdot \langle \pi^+ | (\bar{u}d)_L | 0 \rangle \cdot \langle \bar{K}^0 | (\bar{s}c)_L | D^+ \rangle \,.$$

By taking the ratio of this decay to the semileptonic $D^+ \to \bar{K}^0 e^+ \nu_e$ decay, and using vector meson $(F^{*+})$ dominance to represent the $q^2$ dependence of the unknown form factor $f_+(q^2)$ in the $\langle \bar{K}^0 | (\bar{s}c)_L | D^+ \rangle$ matrix element, one can reliably derive[27]:

$$\frac{\Gamma(D^+ \to \bar{K}^0 \pi^+)}{\Gamma(D^+ \to \bar{K}^0 e^+ \nu_e)} \approx 24\pi^2 |V_{ud}|^2 \left[\frac{4C_+}{3}\right]^2 \left[\frac{f_\pi}{M_D}\right]^2 \approx 1.9 \cdot C_+^2 \,.$$

A previous DELCO fit to the inclusive electron spectrum[61] observed at the $\psi''$ quotes the $D \to Ke\nu$ fraction of semileptonic decay as $(55 \pm 14)\%$, which, combined with the $D^+$ semileptonic branching ratio of $(17.0 \pm 1.9 \pm 0.7)\%$, yields:

$$B(D^+ \to \bar{K}^0 e^+ \nu_e) = (9.3 \pm 2.6)\% \,,$$

a value which is compatible with preliminary Mark III measurements[63] of branching ratios to exclusive semileptonic decay modes. Using this value and our measurement:

$$B(D^+ \to \bar{K}^0\pi^+) = (2.9 \pm 0.6 \pm 0.4)\%$$

leads to the ratio:

$$\frac{\Gamma(D^+ \to \bar{K}^0\pi^+)}{\Gamma(D^+ \to \bar{K}^0 e^+\nu_e)} = 0.31 \pm 0.12 \,.$$

If the nominal QCD value $C_+ = 0.7$ is used, however, a value of 0.9 is predicted for this ratio. This factor of three 'discrepancy' was originally cited as evidence that the factorization hypothesis is invalid in charm decays[27]. One can turn the argument around, and by assuming factorization, at least for the exotic $\bar{K}^0\pi^+$ final state, derive:

$$C_+ = 0.4 \pm 0.1 \,.$$

If the relation $C_+^2 C_- = 1$ is assumed to hold true to all orders, as it does in leading log approximation and approximately in the next-to-lead log calculation (although justification for this is not clear[78]), values of $4 - 11$ for $C_-$, and $8 - 37$ for the ratio $C_-/C_+$ are derived. It can be seen from Figure 6.1 that the lower end of the allowed range for $C_-/C_+$ is compatible with our measurement of the $D^0$ semileptonic branching ratio. This may be evidence for enhancement of the effective $C_-/C_+$ ratio in D decays beyond its perturbative QCD value of $2 - 3$.

The use of factorization can be called into question, however, by the observation of the $D^+ \to \phi\pi^+$ decay at a level comparable to other Cabibbo-suppressed $D^+$ decays. This decay, which occurs in the spectator model only by the second diagram of Figure 1.2(c), like the decay $D^0 \to \bar{K}^0\pi^0$, could be 'color suppressed' due to a possible mismatch of colors between the pairs of quarks which must form the final state hadrons. Unlike the $\bar{K}^0\pi^0$ final state, however, the $\phi\pi^+$ decay cannot proceed by the W-exchange process. In addition, it seems unlikely that this decay is significantly affected by final state interactions.

The presence of the $\phi\pi^+$ decay at an appreciable level thus indicates that color suppression is invalid in D decays, and might be explained in several ways. One explanation is that a very large $C_-/C_+$ ratio removes the effective color suppression, as seen in Figure 1.4. Yet another point of view is that soft gluon transfer, which is not taken into consideration in the calculation of $C_+$ and $C_-$ operator coefficients or by the factorization hypothesis, is probable, and so ruins the color suppression.

The last two arguments may really be the same, if the incalculable, or 'non-perturbative' gluon processes tend to enhance the effective $C_-/C_+$ ratio[34]. In the process, color suppression is ruined, and the semileptonic decay rate for charmed particles is decreased to the level observed in $D^0$ decay. The $D^+$ semileptonic branching ratio is higher because the interference observed in the $\bar{K}^0\pi^+$ decay is also present inclusively[33]. The last hypothesis is probably the most open to question - for example, the rate for $D^+ \to \bar{K}^0\rho^+$ may in fact be enhanced in the SU(6) symmetry limit[79]. Moreover, the modification of the inclusive $D^+$ decay rate has been estimated both in a non-relativistic quark model[80] and in a relativistic model[31]as a relatively small $(10 - 30)\%$ effect. The pattern of decays observed, however, and the non-observation of final states indicative of W-exchange diagrams seem to favor the interference effect over non-spectator processes as the source of the D meson lifetime difference.

Many of the theoretical ideas presented in the introduction and in this chapter were stimulated by earlier measurements from the LGW, Mark II, DELCO, and direct lifetime experiments. The number and precision of the Mark III measurements, however, are sufficient to have put the experimental picture of D decays on a solid basis for the first time. With experimentalists presently trying to measure the weak decays of particles containing $b$ and even $t$ quarks, and theorists attacking weak decays through lattice calculations, we may hope that a consistent theory of hadronic weak decays from kaons to particles containing the top quark will emerge within the not-too-distant future.

## Appendix A.  Track Finding and Fitting

### A.1  INTRODUCTION

The program which finds and fits the trajectories of charged particles in a central tracking chamber can be as crucial to the success of a colliding-beam experiment as the chamber itself. Every such experiment thus far has had a tracking program which is specific to the geometry of its tracking chamber. The new tracking program for Mark III[50], however, was written in an attempt to define a method which could be adapted for other, future detectors. Features of this program are speed nearly three times that of an earlier program, reliable track finding in the face of noisy or dead wires, excellent separation of nearby tracks, and efficient dip angle reconstruction in a drift chamber with only two stereo layers (see the chamber description in section 2.4). Because of the lack of dip angle information provided by the drift chamber, the program has three separate stages. Tracks are first found in X-Y (axial) projection using information from wires which are parallel to the beam axis only. In the next stage, dip angle information is associated with the tracks, using mainly the stereo wire layers. Finally, each trajectory is fitted to a series of linked helices (which would be a single helix in the absence of magnetic field variations), to find the best estimate of the momentum and direction of the particle, and the error matrix of the track parameters.

### A.2  TRACK FINDING

The first step in track reconstruction is to assemble the raw data (in this case, the times of wire hits) in a meaningful order. A circularly linked-list structure is chosen, in which each drift time is associated with a hit index (in case of multiple hits on the same wire), a wire index, a drift cell index, and a layer index. Pointers are supplied for each index which lead either to the next, or to the previous hit, wire, cell, or layer index. At each level of indices, starting and ending indices are defined for the level below. In this manner, the data can be conveniently

accessed in many different ways. The creation of this linked-list data structure takes about 4 ms of CPU time on an IBM 3081K computer, including the time necessary to check for and reject invalid data.

The pattern of struck cells in the axial layers is used in the next step to find all potential tracks in axial projection. The drift chamber layers as presented in chapter 2 are temporarily redefined, at this stage only. In order to make a total of eight axial layers, layer 1 and layer 2 are each split into two sub-layers containing two (sub-layers 1a and 1b) and six (sub-layers 2a and 2b) wire planes, respectively. A cell is then considered struck if hits are found on one of two, four of six, or two of the three wire layers in that cell in layers (1a,1b), (2a,2b), or (3,5,7,8), respectively. The pattern of all struck cells is compared to a 'dictionary' of all 12832 cell patterns which are possible for particles of transverse momentum greater than $0.050 \, \mathrm{GeV/c}$. In the creation of the track dictionary, cells were defined to be 10% larger than their physical size in order to accommodate some multiple Coulomb scattering. Note that the track finding could work as well in an arbitrarily non-uniform magnetic field if the track dictionary were changed accordingly.

Obviously, comparison of every permutation of every subset of some fifty struck cells with 12832 possible tracks is impossible. Thus, we make the comparison in a slightly more subtle manner, using a two-dimensional array in which one dimension is eight bits long, one for each layer of the drift chambers, while the other is 12832 bits long, one for each of the possible tracks. For each struck cell, the track dictionary is consulted to find the set of all tracks which pass through the cell. Bits are then set in the two-dimensional array for the tracks which include that cell. When the array has been filled, it is scanned for eight-bit columns which correspond to valid tracks. A perfect track which passes through all drift chamber layers will thus produce a column of eight '1's. This array tends to be quite sparse, so some computational time can be saved by testing an array whose columns are the logical OR of 32 adjacent columns in

the original array for valid tracks, before testing the individual columns.

A slight further complication is introduced by the necessity of allowing imperfect combinations (either because of a track which exited the chamber before the outer layers, or because of inefficiency in the chamber). The various types of layer combinations allowed by the standard Mark III tracking program are shown in Fig. A.1. Such a combination may be identical to several longer tracks defined in the dictionary. When an imperfect combination is accepted, the other (degenerate) tracks which contain the same combination must be disallowed. In order to retain only the best possible candidate tracks, several passes are made through the $8 \times 12832$ array. The first pass searches for perfect tracks. The next pass searches for tracks having a single missing layer, and disallows degenerate tracks. The next pass after that looks for tracks with two missing layers, and so on. This track finding process is very fast because it is entirely digital, taking less than 1 ms of CPU time on an IBM 3081K computer.

What remains is a list of candidate tracks and the cells which lie on them. This list includes *all* real tracks which reach into layer three of the drift chamber, but may include false tracks as well, particularly if confusion arises from several real tracks passing close to each other or crossing in axial projection. The list of tracks is sorted into distinct 'bundles' of tracks which do not share any drift cells with hits between them. A single bundle may consist of one track, or several tracks which share one or more cells in common.

To select only the real tracks from bundles containing more than one track, we must use the drift time information. Points in X-Y are determined from each hit using the sense wire position and the directions of electron drift to the wire from each side. The multiple sense wire geometry then allows track vectors to be constructed within each cell containing at least two struck wires, while the staggered wire arrangement resolves the left-right ambiguity in most cases. If the ambiguity cannot be resolved, however, all possible track vectors are retained. Each track vector, along with the assumption that the track originated at or

```
Pattern Requirement Array For 0 Misses

Layer    1A   1B   2A   2B   3    5    7
         X    X    X    X    X    X    X


Pattern Requirement Array For 1 Miss

Layer    1A   1B   2A   2B   3    5    7
         X    X    X    X    X    X    .
         X    X    X    X    X    .    X
         X    X    X    X    .    X    X
         X    X    X    .    X    X    X
         X    X    .    X    X    X    X
         X    .    X    X    X    X    X
         .    X    X    X    X    X    X


Pattern Requirement Array For 2 Misses

Layer    1A   1B   2A   2B   3    5    7
         X    X    X    X    X    .    .
         X    .    X    X    X    X    .
         .    X    X    X    X    X    .
```

Figure A.1. Layer combinations allowed in track finding.

near the beam axis, defines a circle which can best be parametrized by its inverse radius and $\phi$ angle at the origin. The resolution from each vector is typically between $0.02 - 0.2\,\mathrm{m}^{-1}$ in $1/R$, depending on the radial distance of the layer from the beam axis, and $10\,\mathrm{mr}$ in $\phi$. The various candidate tracks within a bundle and the unresolved left-right assignments allowed for each can then be compared using a pseudo-$\chi^2$ from the agreement between the $1/R$ and $\phi$ measurements from the track vectors constructed within each drift chamber layer.

Selection of good tracks and rejection of spurious ones proceeds in the following manner. The longest candidate tracks are examined first, starting with the track and set of left-right assignments which has the lowest pseudo-$\chi^2$. The X-Y coordinates from hits on the track are fed to a fast non-iterative circle fitting program (described in Reference 81) which yields a far more restrictive $\chi^2$. This fit minimizes the quantity:

$$[\chi^2] = \sum_{i=1}^{N} \left( \sqrt{(x_i - x_0)^2 + (y_i - y_0)^2} - R \right)^2$$

which is almost equivalent to a true $\chi^2$ in the limit of small residuals, but unlike the true $\chi^2$, can be minimized analytically. If the circle fit has an acceptable $[\chi^2]$, the track is considered real. All of the cells which belong to this track are deleted from the other tracks in the bundle, some of which may become so short that they may be removed from consideration. Others may no longer share cells, and so can be put in a separate bundle. If other tracks remain in the bundle, they too are fed to the circle fitting program in the order described above. If, on the other hand, the track initially chosen does not fit with an acceptable $[\chi^2]$, several directions are pursued. Each combination of drift chamber layers having a single layer deleted from the fit is attempted. If none of these combinations succeed, each combination with two layers deleted from the fit is attempted, and the circle fitting program is fast enough ($\sim 1\,\mu\mathrm{s}$ for 28 wire planes) so that all combinations with three layers deleted may be tried if necessary. If no combination succeeds

in giving an acceptable $[\chi^2]$, the track must be removed from consideration. If one or more combinations having an equal number of wire planes succeed, then the one which has the lowest $[\chi^2]$ is chosen to represent the track. The left-right choices for each wire in a deleted layer are then checked for consistency with the circle parameters from the fit, and if consistent, are reassigned. The track, however, is not considered to be real until all other candidate tracks which might have as many or more wire planes are fed to the circle fitting program. By removing the cells struck by the longest and best tracks from consideration by the other tracks, what initially appears to be a hopelessly tangled set of struck cells can be reduced to the constituent real tracks. Because the circle fitting and track sorting use numerical computations, it takes roughly $1 - 15\,\mathrm{ms}$ per track to select the real tracks, determine which wires to use, and solve the left-right ambiguity where necessary.

## A.3  DIP ANGLE RECONSTRUCTION

Knowledge of all tracks and their circle parameters in X-Y helps greatly in the association of dip angle information with the tracks. We try first to associate struck cells from both stereo layers with each track, as this information is the most reliable and accurate. A drift length and side assignment on a single stereo wire gives a measurement of Z when combined with circle parameters in X-Y. Both stereo layers thus supply up to six measurements of Z, leaving four degrees of freedom to a fit in R and Z, enough for a good check of consistency. Such a fit is performed on each possible combination of a track with struck cells in the stereo layers. In cases where more than one track could be associated with a given stereo cell, the best solution is chosen. The stereo cells and side assignments are then permanently assigned to the favored track, and deleted from possible use by other tracks. The search then continues until either no track remains without both stereo layers 'attached,' or until none of the remaining fits are acceptable. Both stereo layers can be attached for 79% of all tracks, somewhat less than the

84% geometrical coverage of the stereo layers.

The tracks which have both stereo layers attached are then passed to the final helix fit described in the next section. From these fits, the position of the event vertex is found. The vertex is assumed to be at the center of the beam intersection region only if no tracks receive full stereo information. Remaining tracks are then fitted to all possible combinations of a single stereo layer and the event vertex position. In cases where a good combination can be found, the track is extrapolated to the radius of the missing stereo layer. If the Z found by extrapolation agrees with one or more Z measurements which can be made either by drift from the right or the left sides of one or more wires, the wires and side determinations are thereby assigned to the track. This solves, for instance, cases in which the left-right determination is wrong because of a single bad time measurement. If hits in a second stereo layer cannot be assigned to the track, then the vertex position and its error are used in conjunction with the single stereo layer hits in the final helix fit. Of all tracks, 13% are fitted in this manner.

If a track cannot successfully be associated with any stereo layer hits, then the Z measurements found from charge division in hit cells on the track in layers 1, 3, 5, or 7 are used, if they are self-consistent. The vertex position may also be used if the charge division information is inconsistent or inadequate. The dip angle is reconstructed in this way for only 2% of all tracks.

If sufficient charge division information cannot be found, as for many tracks which exit the chamber at small angles to the beam axis, we look for a shower in the endcap calorimeters which is near the end of the visible track in axial projection. If such a shower is found, its position is used with the vertex position to determine the dip angle. Of all tracks, 4% are fitted in this manner.

For another 2% of tracks which have been found in axial projection, no dip angle information can be found. These tracks cannot, therefore, receive a helix fit.

A.4   THE HELIX FIT

After the tracks have been found and had dip angle information assigned to them, a final fit must be made to properly account for the inhomogeneous magnetic field, multiple Coulomb scattering in the beam pipe and chamber, and details of the detector geometry and electron drift. The fitting technique is a modification of the iterative piecewise helix fit developed for the Mark II detector[82,69]. This is a simultaneous least-squares fit in all three dimensions which takes advantage of the local field uniformity to propagate an orbit as a set of linked helices.

Linearization of the equations leads to an iterative fit for the five parameters which characterize a helical trajectory. Iteration of the fit is time-consuming, so some care is worthwhile. Three improvements to the program have proved particularly useful. First, use of the non-iterative circle fit and the approximate determination of dip angle provide an accurate set of initial parameters as starting values for the helix fit, thus allowing the fit to converge with fewer iterations. Secondly, the orbit propagation has been organized to take advantage of the clustered wire geometry of the drift chamber. The fit must calculate a residual and its derivative with respect to the helix parameters at each wire. Since wires are clustered into layers that are about 13 cm apart, but have wire spacing of only 1 cm, the natural organization is to propagate the orbit to the center of each layer using the full 3-space calculation, and then to make fast local orbit approximations to derive the residuals and derivatives for the nearby wires in the layer. This can be done with no loss of precision, actually reducing round-off error, and saves 25% of the execution time of the helix fit. Finally, the time spent in calling small functions and subroutines has been decreased by replacing them with in-line code wherever possible. These three improvements have reduced the execution time by about 55% from the original program, to an average of 17 ms on an IBM 3081K computer for a track with 34 measured hits.

## A.5  CONCLUSIONS

A novel means of finding tracks in the Mark III drift chamber by an entirely digital algorithm has been described. When combined with an improved fitting package, a three-fold increase in speed and an improvement in tracking ability and reliability has been attained. While the program is implemented in a serial processor, the techniques which have been described could also be adapted for track finding on a vector processor. For instance, the initial track finding involves scanning through a large array for valid tracks, which could be handled in several pieces. After the tracks are split into bundles, then each bundle can be split into its real tracks completely independently. Finally, each track is fitted to a helix using information from that track only.

The incorporation of a clustered wire geometry into the structure of this tracking program makes it a suitable model for the next generation of tracking detectors, which will contain more wire planes, and will have to cope with larger numbers of tracks.

# REFERENCES

1. S.L. Glashow, J. Iliopoulos, and L. Maiani, Phys. Rev. **D2**, 1285 (1970).

2. J.J. Aubert *et al.*, Phys. Rev. Lett. **33**, 1404 (1974);

   J.E. Augustin *et al.*, Phys. Rev. Lett. **33**, 1406 (1974).

3. D.J. Gross and F. Wilczek, Phys. Rev. Lett. **30**, 1343 (1973);

   H.D. Politzer, Phys. Reports **14C**, 129 (1974).

4. S. Okubo, Phys. Lett. **5**, 165 (1963);

   G. Zweig, CERN Preprints CERN-TH401, 402, 412 (1964);

   J. Iizuka, Prog. Theor. Phys. Suppl. **37-38**, 21 (1966).

5. M.K. Gaillard, B.W. Lee, and J.L. Rosner, Rev. Mod. Phys. **47**, 277 (1975).

6. K. Kleinknecht and B. Renk, Phys. Lett. **130B**, 459 (1983).

7. G. Goldhaber *et al.*, Phys. Rev. Lett. **37**, 255 (1976);

   I. Peruzzi *et al.*, Phys. Rev. Lett. **37**, 569 (1976).

8. M. Kobayashi and T. Maskawa, Prog. Theor. Phys. **49**, 652 (1973).

9. E. Fernandez *et al.*, Phys. Rev. Lett. **51**, 1022 (1983);

   N. Lockyer *et al.*, Phys. Rev. Lett. **51**, 1316 (1983);

   D.E. Klem *et al.*, Phys. Rev. Lett. **53**, 1873 (1984);

   M. Althoff *et al.*, Phys. Lett. **149B**, 524 (1984).

10. H. Abramowicz *et al.*, Z. Physik **C15**, 19 (1982).

11. L.-L. Chau, Phys. Rep. **93**, 1 (1983).

12. R. Rückl, Habilitationsschrift, University of Munich (1983).

13. G. Trilling, Phys. Reports **75**, 73 (1981).

14. For a review, see M.K. Gaillard, in *Proceedings of the SLAC Summer Institute on Particle Physics*, 1978, M.C. Zipf, ed., SLAC Report **215**, Stanford, p. 397.

15. M.A. Shifman, A.I. Vainshtein, and V.I. Zakharov, Nucl. Phys. **B120**, 316 (1977).

16. M.K. Gaillard and B.W. Lee, Phys. Rev. Lett. **33**, 108 (1974);

G. Altarelli and L. Maiani, Phys. Lett. **52B**, 351 (1974).

17. J. Ellis, M.K. Gaillard, D.V. Nanopoulos, Nucl. Phys. **B100**, 313 (1975)

18. N. Cabibbo and L. Maiani, Phys. Lett. **73B**, 418 (1978);

    D. Fakirov and B. Stech, Nucl. Phys. **B133**, 315 (1978).

19. N. Cabibbo and L. Maiani, Phys. Lett. **79B**, 109 (1978);

    M. Suzuki, Nucl. Phys. **B145**, 420 (1978);

    N. Cabibbo, G. Corbo, and L Maiani, Nucl. Phys. **B155**, 93 (1979).

20. G. Altarelli *et al.*, Phys. Lett. **99B**, 141 (1981).

21. U. Baur and H. Fritzsch, Phys. Lett. **109B**, 402 (1982).

22. R.H. Schindler *et al.*, Phys. Rev. **D24**, 78 (1981).

23. W. Bacino *et al.*, Phys. Rev. Lett. **45**, 329 (1980).

24. A. Pais and S.B. Treiman, Phys. Rev. **D15**, 2529 (1977).

25. N. Ushida *et al.*, Phys. Rev. Lett. **45**, 1049 (1980); **45**, 1053 (1980).

26. A recent review can be found in E. Di Capua, *Proceedings of the Twenty-second International Conference on High Energy Physics*, Leipzig (1984).

27. M. Bonvin and C. Schmidt, Nucl. Phys. **B194**, 319 (1982).

28. L.F. Abbott, P. Sikivie, and M.B. Wise, Phys. Rev. **D21**, 768 (1980).

29. M. Bander, D. Silverman, and A. Soni, Phys. Rev. Lett. **44**, 7 (1980).

30. H. Fritzsch and P. Minkowski, Phys. Lett. **90B**, 455 (1980).

31. H. Sawayanagi, K. Fujii, T. Okazaki, and S. Okubo, Phys. Rev. **D27**, 2107 (1983).

32. I.I.Y. Bigi and M. Fukugita, Phys. Lett. **91B**, 121 (1980).

33. B. Guberina, S. Nussinov, R.D. Peccei, and R. Rückl, Phys. Lett. **89B**, 111 (1979).

34. Y. Igarashi, M. Kuroda, and S. Kitakado, Phys. Lett. **93B**, 125 (1980);

    M. Deshpande, M. Gronau, and D. Sutherland, Phys. Lett. **90B**, 431 (1980);

    M. Gronau and D.G. Sutherland, Nucl. Phys. **B183**, 367 (1981).

35. I.I.Y. Bigi, Phys. Lett. **90B**, 177 (1980).

36. G. Altarelli, N. Cabibbo, and L. Maiani, Nucl. Phys. **B88**, 285 (1975).

37. R.L. Kingsley *et al.*, Phys. Rev. **D11**, 1919 (1975).

38. M.B. Einhorn and C. Quigg, Phys. Rev. **D12**, 2015 (1975).

39. P.A. Rapidis *et al.*, Phys. Rev. Lett. **39**, 526 (1977).

40. K. Lane and E. Eichten, Phys. Rev. Lett. **37**, 477 (1976).

41. R.H. Schindler, SLAC Report **219** (1979);

    J.D. Jackson and D.L. Scharre, Nucl. Instr. and Meth. **128**, 13 (1975);

    G. Bonneau and F. Martin, Nucl. Phys. **B27**, 381 (1971).

42. I. Peruzzi *et al*, Phys. Rev. Lett. **39**, 1301 (1977).

43. F.A. Behrends and R. Kleiss, Acta Physica Polonica **B14**, 413 (1983).

44. D. Bernstein *et al.*, Nucl. Instr. and Meth. **226**, 301 (1984).

45. J. Roehrig *et al.*, Nucl. Instr. and Meth. **226**, 319 (1984).

46. J.S. Brown *et al.*, Nucl. Instr. and Meth. **221**, 503 (1984).

47. W. Toki *et al.*, Nucl. Instr. and Meth. **219**, 479 (1984).

48. R. Fabrizio *et al.*, Nucl. Instr. and Meth. **227**, 220 (1984).

49. J.J. Thaler *et al.*, IEEE Trans. **NS-30**, 236 (1983).

50. See, also, J.J. Becker *et al.*, Nucl. Instr. and Meth. **235**, 502 (1985).

51. Sternheimer and Peierls, Phys. Rev. **B3**, 3681 (1971).

52. A. Ali and T.C. Yang, Phys. Lett. **65B**, 295 (1976).

53. B. Jongejans, in *Proceedings of the International School of Elementary Particle Physics*, M. Nikolic, ed., Gordon and Breach, N.Y. (1970), vol. IV part 1, p. 349.

54. C. Bromberg *et al.*, Phys. Rev. **D22**, 1513 (1980).

55. S.M. Flatté, Phys. Lett. **63B**, 224 (1976).

56. Many of the results on Cabibbo-suppressed D decays are contained in R.M. Baltrusaitis *et al.*, SLAC-PUB-3544, submitted to Phys. Rev. Lett. (1985).

57. See, also, S. Plaetzer, Ph.D. thesis, University of Illinois (1985).

58. R. Bailey *et al.*, Phys. Lett. **139B**, 320 (1984).

59. The results of this analysis are contained in R.M. Baltrusaitis *et al.*, Phys. Rev. Lett. **54**, 1976 (1985).

60. J.H. Friedman, IEEE Trans. **C-26**, 404 (1977).

61. W. Bacino *et al.*, Phys. Rev. Lett. **43**, 1073 (1979).

62. J.M. Feller *et al.*, Phys. Rev. Lett. **40**, 274 (1978).

63. D. Coffman, *Proceedings of the First International Conference on Hadron Spectroscopy*, Maryland (1985).

64. P.A. Rapidis *et al.*, Phys. Rev. Lett. **39**, 526 (1977);
    I. Peruzzi *et al.*, Phys. Rev. Lett. **39**, 1301 (1977).

65. R.H. Schindler *et al.*, Phys. Rev. **D21**, 2716 (1980).

66. W. Bacino *et al.*, Phys. Rev. Lett. **40**, 671 (1978).

67. H. Sadrozinski, *Proceedings of the Twentieth International Conference on High Energy Physics*, Madison (1980).

68. This is valid except for final states which are eigenstates of CP such as $\bar{K}^0 \pi^0$, which, however, are not particularly prevalent in $D^0$ decays.

69. R.H. Schindler, Ph.D. thesis, Stanford University, SLAC Report **219** (1979).

70. J.L. Siegrist, Ph.D. thesis, Stanford University, SLAC Report **225** (1979).

71. R.A. Partridge, Ph.D. thesis, California Institute of Technology, CALT-68-1105 (1984).

72. G.S. Abrams *et al.*, Phys. Rev. Lett. **43**, 481 (1979).

73. L.L. Wang and F. Wilczek, Phys. Rev. Lett. **43**, 3341 (1979);
    M. Suzuki, Phys. Rev. Lett. **43**, 818 (1979);
    V. Barger and S. Pakvasa, Phys. Rev. Lett. **43**, 812 (1979).

74. J.F. Donoghue and B.R. Holstein, Phys. Rev. **D21**, 1334 (1980).

75. M. Glück, Phys. Lett. **88B**, 145 (1980).

76. L.-L. Chau and F. Wilczek, Phys. Rev. Lett. **43**, 816 (1983).

77. A.N. Kamal, SLAC-PUB-3443, submitted to Phys. Rev. D (1984).

78. M.B. Wise, private communication.

79. I.I.Y. Bigi, Z. Phys. **C6**, 83 (1980).

80. T. Kobayashi and N. Yamazaki, Prog. Theor. Phys. **65**, 775 (1981).

81. J.F. Crawford, Nucl. Instr. and Meth. **211**, 223 (1983).

82. G.H. Trilling and A.D. Johnson, LBL internal memo **TD-301** (1978).